Master thesis and internship[BR]- Master's Thesis : Station-Keeping Attitude Control of an Under-Actuated CubeSat in orbit around Collinear Libation Points[BR]- Internship (linked to master's thesis)

Auteur : Macchiaiolo, Luca
Promoteur(s) : Collette, Christophe
Faculté : Faculté des Sciences appliquées
Diplôme : Master en ingénieur civil en aérospatiale, à finalité spécialisée en "aerospace engineering"
Année académique : 2019-2020
URI/URL : http://hdl.handle.net/2268.2/10389

Station-Keeping Attitude Control of an Under-Actuated CubeSat in orbit around Collinear Libation Points

Luca Macchiaiolo

Année académique 2019-2020

Travail de fin d'études réalisé en vue de l'obtention du grade de master Ingénieur Civil en Ingénierie Aérospatiale

Promoteur : Christophe Collette

Université de Liège - Faculté des Sciences Appliquées

Abstract

The rising of the CubeSat concept is re-defining the canonical approach to space mission design. The exponential interest in the use of CubeSats for deep space missions opens up a wide range of new possibilities along with new technological challenges. The reduced spacecraft available space combined with stringent mission requirements drives the search for innovative solutions for the optimization of the resources on board. On the other hand, new horizons are opening up for CubeSat applications; Libration point missions for scientific or support purposes seem to be the next step in the development and refinement of nano-satellite technologies. This work proposes an innovative solution where the stand-alone CubeSat main propulsion system and the ADCS actuators merge together in a 4-thruster assembly able to provide both Station-Keeping and Attitude Control for Libration Point missions.

Contents

List of Tables

List of Figures

Chapter 1

Introduction

1.1 Work description

The rising of the CubeSat concept is re-defining the canonical approach to space mission design. If space missions were previously conceived using a single, large, expensive, multi-tasking satellite, now the same mission objectives can be achieved by multiple small satellites in formation flight or constellations or swarms, with incomparable advantages: first of all, mission objectives can be broken down and assigned individually to several satellites, thus avoiding the classic performance trade-off typical of conventional satellites. Moreover, the adoption of *Off-The-Shelf Components (COTS)* ensures faster, cheaper and more efficient development process. Cubesats make possible support missions to main spacecrafts, further expanding the scientific return of the global mission. Since their first appearance in the space sector to date, CubeSats have been used as technological demonstrators or Earth observer devices for science purposes. Recently there has been a shift towards more complex and ambitious missions in deep space. Stand-alone or formation flying CubeSats have been proposed for interplanetary missions as daughter ships of conventional mother satellites or directly concieved as principal satellites. In 2018, the *Insight mission* supported by the two deep-space CubeSats *MarCO-A* and *MarCO-B* set the milestones for deep-space operations of CubeSats.

Many missions involving the use of CubeSats in orbit around the *Libration points* (also called *Lagrangian points)* of the Earth-Moon or Sun-Earth system are currently being

considered. Those equilibrium points in the *Restricted Three Body Problem (R3BP)* offer uncommon features for space operations; because their positions is almost constant with respect to the two attracting bodies, orbits around them can be designed in order to enable the spacecraft to be always visible from Earth always maintaining a privileged view on the second body. This characteristic tuns out to be extremely beneficial both for science missions both for relay and support missions devoted to future space colonisation. The technological challenges for Cubesats operating in deep space are nonetheless arduous. The complexity of required operations in conjunction with reliability and robustness to space environment requisites, become more and more challenging to achieve as the on-board available space decreases. Especially for the propulsion and attitude control system it becomes almost impossible to design two separate system acting independently; the combination of the two tuns out to be the only possible solution in order to provide propulsion for orbital maneuvers (*Station-Keeping*) and propulsive attitude control in an efficient way.

This work aims to address the problematic of the station-keeping/attitude control coupling in the case of an under-actuated spacecraft in orbit around collinear libration points. The term "under-actuated" means a satellite with fewer actuators than the number of degrees of freedom it is intended to control. Both the station-keeping and the attitude control are obtained by using only four engines located along the satellite and equipped with a gimbal system able to direct the thrust produced. Thanks to recent developments in the field of electric propulsion, a type of continuous control at low thrust level has been chosen to provide positioning and attitude control. The three main types of libration point orbits have been taken into consideration in the study, namely: *Halo Orbits*, *Lyapunov Orbits* and *Lissajous Orbits*. Those families of orbits are compared and evaluated in terms of control effort in order to highlights the advantages and disadvantages of the proposed architecture once applied to the most common scenarios concerning missions around Lagrangian points.

The whole work is developed following the red thread schematically represented in Fig.(1.1).

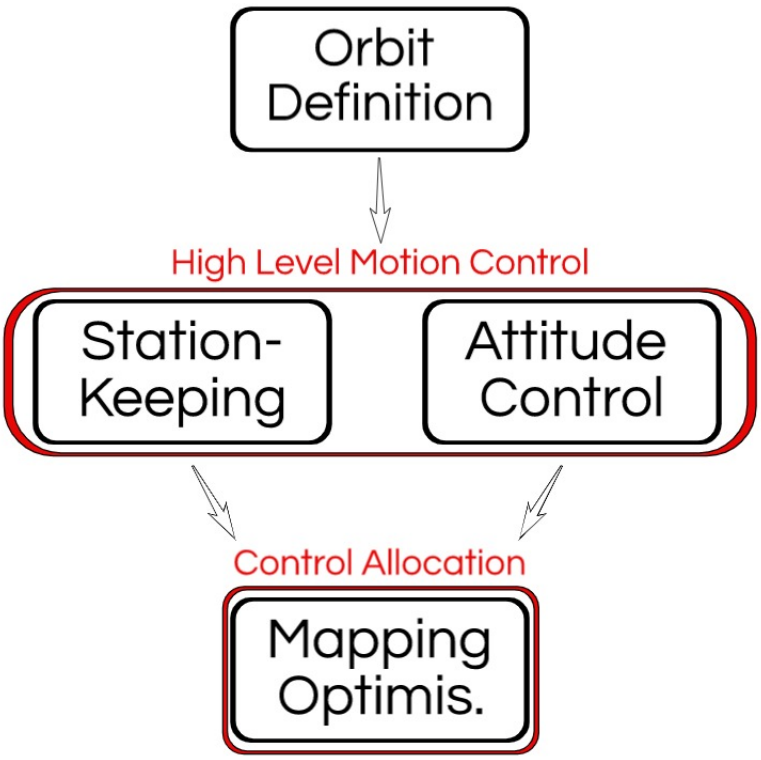

Figure 1.1: Project workflow.

Firstly, the nominal trajectories around collinear libration points are derived. Then the clue topic of station-keeping/attitude control is addressed through a *two-step approach*:

1. *Step 1: High-Level Motion Control.* The ideal input forces, required to achieve satisfactory station-keeping performances, and the ideal input torques, ruling the satellite attitude evolution along the orbit, are computed independently without considering any coupling among them. The coupling in fact derives from the adoption of a limited number of actuators to accomplish both tasks. The actuators properties are not taken into consideration at this stage.

2. *Step 2: Control Allocation.* Once the traces of ideal forces and moments have been defined, an optimisation process is carried out in order to map them onto the engines. By doing so it is derived the optimal combination of engine orientations and thrust levels in order to achieve the ideal control inputs computed at step 1, or in order to minimise the error between the actual control inputs and the ideal ones if the

commanded ideal inputs are out of reach of the engine system.

The report is organized as follows: *Chapter 1* continues with an historical review and the state of the art concerning the fundamental topics covered in the work.
Chapter 2 presents the mathematical formulation of the *Restricted Three Body Problem (R3BP)*, which is the dynamic model used as baseline framework. The mathematical formulation of the orbits is subsequently exposed, together with the methodologies adopted to calculate them numerically. The simulated orbits are shown at the end of the chapter, together with tables grouping their most important parameters.
Chapter 3 focuses on the *Station-Keeping* strategy used to keep the spacecraft close to its nominal orbit. The theory behind the methodology adopted is explained at the beginning of the chapter while the numerical results for each of the orbit chosen, as representative for the respective family, are presented at the end.
Chapter 4 provides the fundamentals of attitude control and the mathematical background which lies behind the techniques chosen to accomplish the task; as in the other cases the numerical results are shown at the end of the chapter with a detailed description of the parameters used in the simulations.
Chapter 5 deals with the control allocation procedure implemented in the project. Firstly the optimisation algorithms adopted are properly defined; then the analysis of the results in terms of engine thrust levels and mapping errors is pursued, for each typology of orbit, for the following cases:

- Unconstrained gimbal angle.
- Constrained gimbal angle.

Afterwards the selection of the thruster type is carried out based on a detailed comparison of the *Micro Electro-Mechanical System (MEMS)* technologies available (or close to be) on the market.
In *Chapter 6* the main conclusions are drawn and further developments are suggested.

1.2 Historical review and State of the Art

In 1772, the French mathematician, J. L. Lagrange, showed that there are five positions of equilibrium in a rotating two-body gravity field model; the model is referred as the *Restricted Three Body Problem (R3BP)*. Those equilibrium points are called *"Lagrangian Points"* or *"Libration Points"*. Three out of five lie on the line joining the massive bodies, called *Primaries*, while the remaining two form equilateral triangles with the primaries. All five libration points belong to the orbit plane of the two attractive bodies.

The libration points aroused great interest within the scientific community since the early dawn of the space era. They offer the unique possibility to design a space mission having the spacecraft with fixed configuration with respect to two primaries. It enlarges the mission design possibilities enabling the achievement of objectives which would not be achievable with classical Keplerian *Two Body Problem (TBP)* orbits. Moreover, since the libration points are characterised by an unstable dynamics, they might be exploited to obtain low-energy interplanetary, lunar, moon-to-moon transfers of practical interest. Historically it was in 1950 that Arthur C. Clark suggested to use the L2 point of the Earth-Moon system to broadcast radio and TV signals to the foreseen colonies on the back side of the Moon. This idea was grasped and developed by Farquhar in 1966 who drew the first libration point orbit in the history [38], a quasi-periodic *Lissajous Orbit*. Later, in 1973, Farquhar and Kamel achieved to analytical define a periodic orbit around libration points called *Halo Orbit* [19]. The first application of the theoretical studies carried out by Farquhar and Kamel is the International Sun-Earth Explorer (ISEE) Program [16]. The ISEE mission envisaged three spacecrafts, ISEE-1 and ISEE-2 located in an highly elliptical orbit around Earth and ISEE-3 in an halo orbit around the Sun-Earth L1 [46]. The incredible success of the ISEE-3 mission (which was extended in 1981 and renamed as ICE Extended Mission), encouraged the space community to develop new space missions exploiting the libration point characteristics. The first who seized the opportunity were the Russians in 1990 with Relict-2 which unfortunately was discarded due to the financial problems arose from the collapse of the Soviet Union [17]. The 2^{nd} libration point mission was the SOlar Heliospheric Observatory (SOHO) launched in 1995 and funded by ESA.

It entered its L1 halo orbit on February 14, 1996, an orbit designed on the heritage left by ISEE-3. The continuous detailed solar observations available to all via the Web have set a new standard for solar observation and the mission it is still operative [15]. In 1997 The Advanced Composition Explorer (ACE) was launched and it is the full-fledged 3^{rd} libration point mission. ACE was placed into a Sun-Earth L1 Lissajous orbit and it is still operative [43]. The WIND spacecraft is considered the 4^{th} libration point satellite even if it was lauched before the ACE, because its orbit is not properly considered as a "pure" libration point one. In the new millennium plenty of libration points mission were launched: the Wilkinson Microwave Anisotropy Probe (WMAP) in 2001, THEMIS-ARTEMIS mission in 2007, Herschel Space Telescope and Planck Space Observatory in 2009, Chang'e 2 in 2010, the Gaia Space Observatory in 2013, Chang'e 5-T1 Service Module in 2014, the Deep Space Climate Observatory (DSCOVR) in 2015, LISA Pathfinder (LPF) in 2015, Queqiao spacecraft in 2018 and Spektr-RG spacecraft in 2019. For the next decade at least 15 missions are planned to be launched towards libration points.

This incredible interest in deep-space exploration and in libration point missions is driving also many developers and manufacturers to design affordable and easy-to-develop CubeSats capable of taking on such missions. Since the early 2000s the role of CubeSats in the space scenario has risen in a predominant way. CubeSats are a subset of SmallSats (spacecrafts with a mass less than 500 Kg), and are built in standard units of 10 cm $\times$ 10 cm $\times$ 10 cm cubes (called a 1U which typically weigh less than 2 kg) and usually are composed of standardised *Commercial Off-The-Shelf (COTS)* components. It is precisely this standardization of size and subsequent CubeSat components such as the spacecraft structure, electronics, power systems and communications modules that allows them to be developed, built and launched in an extremely less expansive way with respect to conventional satellites, causing the recent spike in the CubeSat's popularity [18]. More than 1000 CubeSats were launched from 2001 to date and more than 2500 are planned to lift-off in the next 6 years. The vast majority of CubeSats are intended for *Low Earth Orbit (LEO)* operations but *NASA Jet Propulsion Laboratory (JPL)*, in 2018, set the cornerstone for the employment of CubeSats in deep-space missions; *MarCO-A (Wall-E)* and *MarCO-B*

(Eva) CubeSats are the first two nano-satellites to operate beyond Earth orbit, in the deep-space environment. Mars Cube One (or MarCO) was a Mars flyby mission launched on 5 May 2018 alongside NASA's InSight Mars lander mission. The role of MarCO-A and MarCO-B was to provided a real-time communications link to Earth for InSight during its entry, descent, and landing *(EDL)* when InSight was out of line of sight from the Earth. Both spacecraft were 6U CubeSats, and the mission was a test of new miniaturized communications and navigation technologies. Both nano-satellites accomplished succesfully their mission before the loss of contact happened in January 2019 [41]. For the next years, dozen of CubeSats mission concepts are under analysis from the major space agencies all around the world. JPL has already flight-qualified the two CubeSats for its *INSPIRE (Interplanetary Nano-Spacecraft Pathfinder in Relevant Environment)* mission and it is developing several other projects of the kind, notably *Lunar Flashlight*, *Near Earth Asteroid Scout*, *LunarIceCube*, *MarsDROP* and *NANOSWARM* [1]. The *European Space Agency (ESA)*, for its part, is investigating new mission concepts involving a number of CubeSats operating in interplanetary space in orther to enhance the scientific return of the already proposed ESA missions; the most representative ones are *Miniaturised Asteroid Remote Geophysical Observer (M-ARGO)*, *DustCube*, *CUBATA*, *Payload of Advanced Little Satellites (PALS)*, *Asteroid Geophysical Explorer (AGEX)*, *Lunar Meteoroid Impact Observer (LUMIO)*, *Moon CubeSat for the Analysis of the Radiation Environment (MoonCARE)*, *CubeSat Low frequency Explorer (CLE)* and *Lunar Volatile and Mineralogy Mapping Orbiter (VMMO)* [7]. Many of them are supposed to be placed in orbits around libration points.

One of the crucial challenges regarding CubeSat design is to fit all the required components in the tiny available space on-board in order to allow the nano-satellite to match the mission requirements and constraints. Of particular interest is the *Attitude and Orbit Control System (AOCS)* whose aim is to provide the necessary torque and force inputs to control the attitude and position of the spacecraft along its orbit. Generally a sufficient number of actuators is implemented in order to control separately the spacecraft attitude and the orbit maintenance (*Station-Keeping*). This solution grants robustness to external

perturbations and actuator failures due to the high redundancy of the system, and allows an independent, not coupled, control of spacecraft attitude from the orbit positioning control; the main drawback is the wide number of actuators which must fit in the CubeSat limited space. Moreover the most diffuse AOCS architecture envisages the the adoption of *Reaction Wheels (RW)* in conjunction with a certain number of thrusters displaced all around the spacecraft (or magnetotorques if possible). Reaction wheels are a consolidated space technology and ensure high performances in terms of pointing accuracy for a moderate cost of On-Board mass, volume occupied and energy consumption; on the other hand they cannot be boarded without a collateral thruster system devoted to de-saturatation the RW once they reach their momentum storage limit. Many efforts have been put into the optimisation of thruster usage for RW de-saturation/station-keeping manoeuvres. Both MarCO A and B adopt a RW Assembly unitedly with 8 cold gas thruster devoted to attitude control and *Trajectory Correction Maneuvers (TCMs)* [40]; also in LUMIO project different de-saturation strategies are investigated with an unconventional approach due to the employment of only four thrusters in order to achieve Moon tracking cooperartively with de-saturation procedures [6]. Other projects deal with "pure" thrusters attitude control in order to avoid the implementation of RW, such as [13] [21]. Nevertheless the new horizon for high accuracy attitude control and station-keeping systems is represented by electric propulsion: recent technological advances in the development of electric micro-thrusters pave the way to the successful diffusion of all-electric spacecraft capable of providing high-accuracy pointing, long-term stability of pointing, orbit maintenance, and long-term orbit maneuvers. In 2015 the feasibility of the concept was practically demonstrated by the on-orbit demonstrator of the United States Naval Academy's BRICSat-P CubeSat that housed four micro-cathode thrusters developed by the George Washington University in a 1.5U form factor [26] [27]. Moreover concerning the main propulsion system, electrical engines are asserted as the rightful heir to chemical propulsion systems. Full-electric satellites appeared in the market in 2015 with the ABS-3A satellite for ABS and the EUTELSAT 115 West B satellite for Eutelsat produced by Boeing. From 2015 to date more that 40 satellites boarding electrical engines

were launched. Among them the most famous *LISA Pathfinder* and *BepiColombo* missions embed respectively 8 electrospray thruster for high precision attitude control and T6 QinetiQ arcject engines for station-keeping and de-orbiting operations; one-fourth of the rest is represented by electrical propelled CubeSats for near-Earth operations. The most important research and development initiative in the field is the NASA's *Solar Electric Propulsion (SEP)* program which is developing critical technologies to extend the length and capabilities of ambitious new science and exploration missions. Alternative propulsion technologies such as SEP may deliver the right mix of cost savings, safety and superior propulsive power to enrich a variety of next-generation journeys to worlds and destinations beyond Earth orbit. To be mentioned in addition to LISA Pathfinder and BepiColombo missions are the *Dawn* probe, *Deep Space 1* and *Hayabusa* propelled by ion engines and *Small Missions for Advanced Research in Technology (SMART-1)* equipped with Hall-Effect thrusters [10] [23] [24] [34]. It is evident from those numbers and the number of research project involved in that electric propulsion is becoming the paradigm for the space propulsion field for the close future.

Chapter 2

Dynamics Model

2.1 Circular Restricted Three Body Problem

2.1.1 Problem statement and equations of motion

The problem is formulated as it follows: two bodies revolve around their center of mass in circular orbits under the influence of their mutual gravitational attraction, and a third body moves attracted by the previous two, without influencing their motion. The *Circular Restricted Three Body Problem (CR3BP)* aims to describing the motion of the third body. The two revolving bodies are called *primaries* and they have a specific spatial mass distribution such that they might be considered as point masses; they respective masses are called m_1 and m_2 while the mass associated to the third body is called m_3. The third body is called *secondary*. It is assumed that m_3 is much smaller that either m_1 and m_2 in such a way that the presence of the third body doesn't affect the motion of the primaries [44].

The equation of motions are described with respect to a non-inertial, co-rotating reference frame $O(xyz)$ whose origin is set to the centre of mass G of the primaries with the x-axis directed toward m_1.; the y-axis lies in the orbital plane while the z-axis complete the right-hand triad. The constant, inertial angular velocity of the rotating frame is named Ω and it's directed along the z-axis [12].

The distance between the primaries, i.e. the radius of the circular orbit of one primary

with respect to the other, is called r_{12} and it is constant. They are named $\boldsymbol{r}$, $\boldsymbol{r_1}$, $\boldsymbol{r_2}$ the positions of the third body with respect to CG in the co-rotating reference frame, as shown in Fig.(2.1).

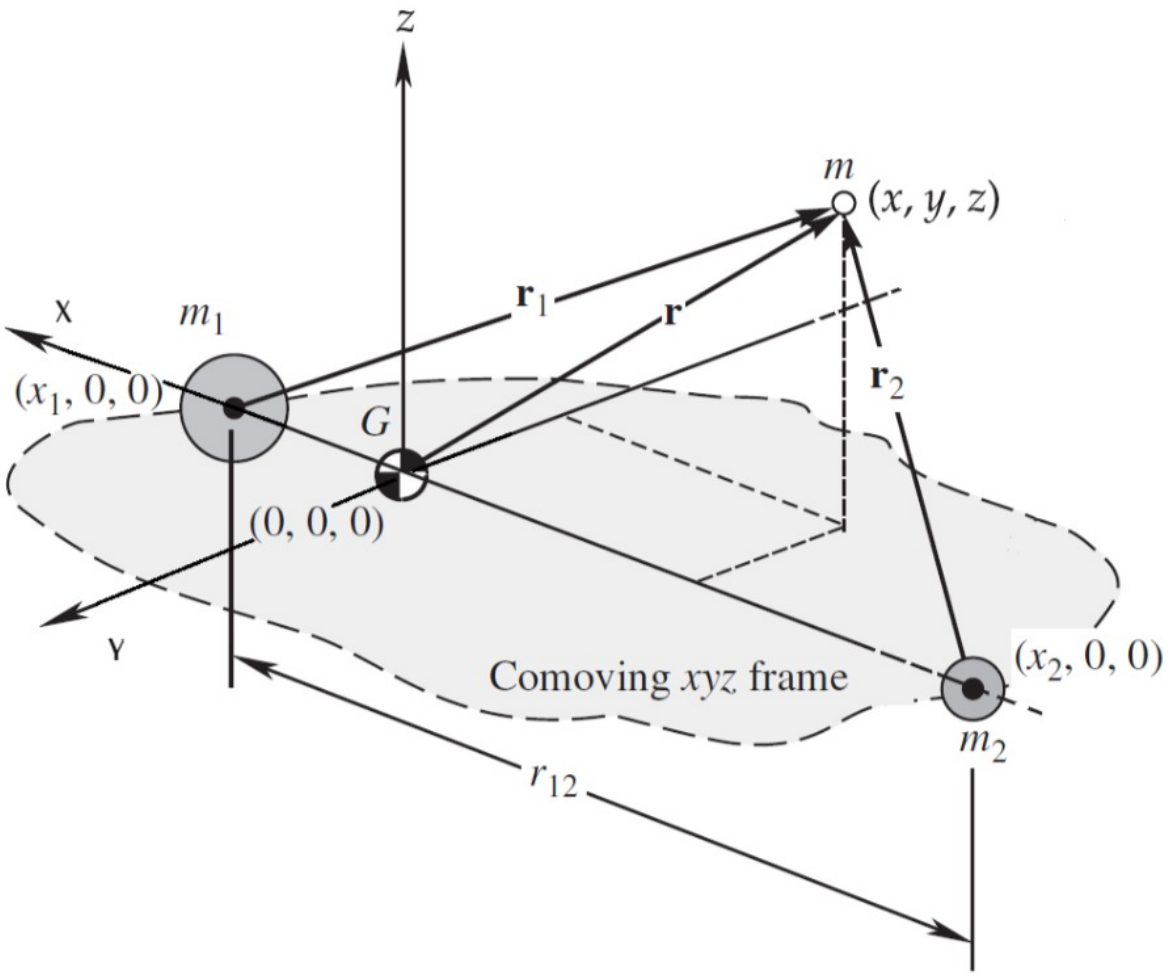

Figure 2.1: CR3BP Reference Frame

Without loss of generality it is assumed $m_2 < m_1$ and it is introduced the following notation:

$$\begin{aligned} M &= m_1 + m_2 \\ \pi_1 &= \frac{m_1}{M} = \pi \\ \pi_2 &= \frac{m_2}{M} = (1 - \pi) \end{aligned} \tag{2.1}$$

It is thus straightforward to derive the position of the primaries with respect to the centre

of mass, Eq.(2.2c) and Eq.(2.2d), by plugging Eq.(2.2a) into Eq.(2.2b).

$$Mx_g = m_1x_1 + m_2x_2 = 0 \tag{2.2a}$$

$$r_{12} = x_1 - x_2 \tag{2.2b}$$

$$x_1 = (1 - \pi)\, r_{12} \tag{2.2c}$$

$$x_2 = -\pi\, r_{12} \tag{2.2d}$$

Then the dynamics of the third mass is expressed according to Eq.(2.3)

$$m_3\ddot{\boldsymbol{r}} = -\frac{\mu_1 m_3}{r_1^3}\boldsymbol{r_1} - \frac{\mu_2 m_3}{r_2^3}\boldsymbol{r_2} \tag{2.3}$$

where

$$r_1 = \sqrt{(x - (1 - \pi)r_{12})^2 + y^2 + z^2} \tag{2.4a}$$

$$r_2 = \sqrt{(x + \pi r_{12})^2 + y^2 + z^2} \tag{2.4b}$$

and $\mu_{1,2}$ is the *standard gravitational parameter* of the respective primary. Expressing $\ddot{\boldsymbol{r}}$ in the non-inertial, co-rotating reference frame, Eq.(2.5)

$$\ddot{\boldsymbol{r}} = (\ddot{x} - 2\Omega\dot{y} - \Omega^2 x)\hat{x} + (\ddot{y} + 2\Omega\dot{x} - \Omega^2 y)\hat{y} + \ddot{z}\hat{z} \tag{2.5}$$

it is possible to derive the EoMs in their scalar form [12]:

$$\begin{cases} \ddot{x} - 2\Omega\dot{y} - \Omega^2 x = -\dfrac{\mu_1(x + (\pi - 1)r_{12})}{r_1^3} - \dfrac{\mu_2(x + \pi r_{12})}{r_2^3} & \text{(2.6a)} \\ \ddot{y} + 2\Omega\dot{x} - \Omega^2 y = -\dfrac{\mu_1}{r_1^3}y - \dfrac{\mu_1}{r_2^3}y & \text{(2.6b)} \\ \ddot{z} = -\dfrac{\mu_1}{r_1^3}z - \dfrac{\mu_1}{r_2^3}z & \text{(2.6c)} \end{cases}$$

Defining the *Three Bodies Potential Energy* as:

$$U = \left(\frac{\mu_1}{r_1} + \frac{\mu_2}{r_2}\right) + \frac{1}{2}\Omega^2(x^2 + y^2) \tag{2.7}$$

Eq.(2.6) might be re-written as:

$$\begin{cases} \ddot{x} - 2\Omega\dot{y} = U_{/x} \\ \ddot{y} + 2\Omega\dot{x} = U_{/y} \\ \ddot{z} = U_{/z} \end{cases} \tag{2.8}$$

which might also be expressed in vectorial notation, Eq.(2.9):

$$\frac{\partial^2 \boldsymbol{r}}{\partial t^2} = \nabla U - 2\Omega \times \frac{\partial \boldsymbol{r}}{\partial t} \tag{2.9}$$

It is furthermore possible to rewrite the EoMs in their adimensional formulation which gives the simplest form of the differential equations set [44]. Introducing

$$\tilde{x} = \frac{x}{r_{12}}; \quad \tilde{y} = \frac{y}{r_{12}}; \quad \tilde{z} = \frac{z}{r_{12}}; \quad \tilde{t} = \Omega t; \quad \tilde{r_1} = \frac{r_1}{r_{12}}; \quad \tilde{r_2} = \frac{r_2}{r_{12}} \tag{2.10}$$

and considering that in the dimensionless form the *Gravitational Constant* $G = 1$, so that $\pi_{1,2} = \mu_{1,2}$, Eq.(2.7) and Eq.(2.8) read:

$$\tilde{U} = \frac{1}{2}(\tilde{x}^2 + y^2) + \frac{1-\mu}{\tilde{r_1}} + \frac{\mu}{\tilde{r_2}} \tag{2.11}$$

$$\begin{cases} \ddot{\tilde{x}} - 2\dot{\tilde{y}} = \tilde{U}_{/\tilde{x}} \\ \ddot{\tilde{y}} + 2\dot{\tilde{x}} = \tilde{U}_{/\tilde{y}} \\ \ddot{\tilde{z}} = \tilde{U}_{/\tilde{z}} \end{cases} \tag{2.12}$$

where it is set $\mu = \mu_2$ and thus $\mu_1 = 1 - \mu$.

It is worth remarking that in Eq.(2.11), $\mu_{1,2}$ represent the adimensional standard gravitational parameter which coincides with the mass ratio $\pi_{1,2}$ defined in Eq.(2.1).

2.1.2 Jacobi Constant

Differently from the *Two Bodies Problem*, the CR3BP is characterized by a single integral of motion which is called the *Jacobi Integral* and its related constant called *Jacobi Constant* C.

It is here derived by multiplying Eq.(2.6a) times $\dot{x}$, Eq.(2.6b) times $\dot{y}$ and Eq.(2.6b) times $\dot{z}$ and then summing the results up together obtaining:

$$\frac{1}{2}v^2 - \frac{1}{2}\Omega^2(x^2+y^2) - \frac{\mu_1}{r_1} - \frac{\mu_2}{r_2} = -2C \tag{2.13}$$

By using the potential definition of Eq.(2.7), Eq.(2.13) might be reformulated as:

$$C = 2U - v^2 \tag{2.14}$$

where $v^2 = \dot{x}^2 + \dot{y}^2 + \dot{z}^2$.

The adimensional expression of the Jacobi constant is:

$$\tilde{C} = 2\tilde{U} - \tilde{v}^2 \tag{2.15}$$

with $\tilde{v}^2 = \dot{\tilde{x}}^2 + \dot{\tilde{y}}^2 + \dot{\tilde{z}}^2$.

2.1.3 Libration points

Although the EoMs have no closed form solution, as it exists just one integral of motion for a phase space of dimension 6, they might be used to find the equilibrium points of the system. The equilibrium points of the system are called *"Lagrangian points"* or *"Libration points"* and are defined by the conditions:

$$\dot{\tilde{x}} = \dot{\tilde{y}} = \dot{\tilde{z}} = \ddot{\tilde{x}} = \ddot{\tilde{y}} = \ddot{\tilde{z}} = 0 \tag{2.16}$$

Substituting Eq.(2.16) in Eq.(2.12) yields

$$\begin{cases} \tilde{x} = \dfrac{(1-\mu)(\tilde{x}+\mu)}{\tilde{r_1}^3} + \dfrac{\mu(\tilde{x}-(1-\mu))}{\tilde{r_2}^3} & \text{(2.17a)} \\ \tilde{y} = \dfrac{(1-\mu)}{\tilde{r_1}^3}\tilde{y} + \dfrac{\mu}{\tilde{r_2}^3}\tilde{y} & \text{(2.17b)} \\ 0 = \dfrac{(1-\mu)}{\tilde{r_1}^3}\tilde{z} + \dfrac{\mu}{\tilde{r_2}^3}\tilde{z} & \text{(2.17c)} \end{cases}$$

which is equivalent to impose $\nabla U = 0$.

The solutions of Eq.(2.17) are the location of the Lagrangian points, whose name convention refers to Fig.(2.2).

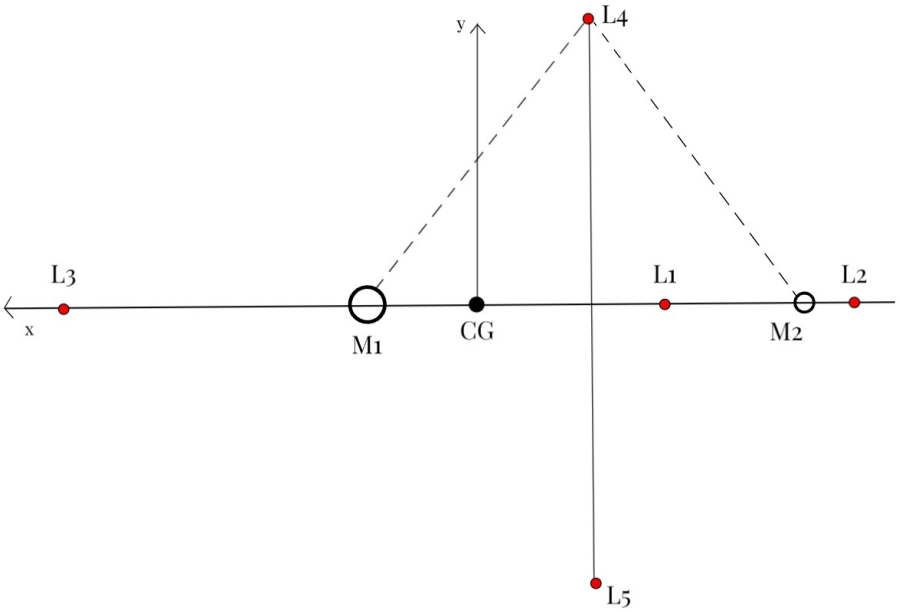

Figure 2.2: Lagrangian points positions in the co-rotating frame.

The coordinates relative to the equilateral Lagrangian points L_4 and L_5 are found by solving Eq.(2.17a) and Eq.(2.17b) and are expressed by Eq.(2.18):

$$L_4, L_5 : \quad x = \mu - \frac{1}{2}, \quad y = \pm\frac{\sqrt{3}}{2}, \quad z = 0 \tag{2.18}$$

Regarding the collinear points L_1, L_2 and L_3, their coordinates are found by setting $y = 0$ and Eq.(2.17a) may be reformulated as [12]:

$$f(\mu, \tilde{x}) = 0 \tag{2.19}$$

where

$$f(\mu, \tilde{x}) = \frac{1-\mu}{|\tilde{x}+\mu|}(\tilde{x}+\mu) + \frac{\mu}{|\tilde{x}+\mu-1|^3}(\tilde{x}+\mu-1) - \tilde{x} \tag{2.20}$$

The locations of the Lagrangian points for the Sun-Earth+Moon system and Earth-Moon system are presented in Tab.(2.1) and Tab.(2.2)

	$\tilde{x}$	$\tilde{y}$
L_1	-0.990027	0
L_2	-1.010034	0
L_3	1.000001	0
L_4	-0.499997	-0.866025
L_5	-0.499997	0.866025

Table 2.1: Lagrangian points coordinates of the Sun-Earth+Moon system

	$\tilde{x}$	$\tilde{y}$
L_1	-0.836915	0
L_2	-1.155682	0
L_3	1.005063	0
L_4	-0.487849	-0.866025
L_5	-0.487849	0.866025

Table 2.2: Lagrangian points coordinates of the Earth-Moon system

2.1.4 Orbits around collinear points

This section is based on the non-dimensional form of the EoMs and, for sake of simplicity on notation, the tilde characterizing adimensional quantities is omitted.
The EoMs expressed by Eq.(2.12) have no closed form solution, thus a numerical approach is required in order to determine orbits around the Lagrangian points. There exists a vast majority of different type of periodic and quasi-periodic orbits around the collinear points L_1, L_2 and L_3 among which the most known ones are [14] [28]

1. Lissajous Orbits.
2. Planar Lyapunov Orbits.
3. Halo Orbits.

Those typologies of orbits born as analytical solutions of approximated EoMs; more precisely, Lissajous orbits are the solution of the first order approximation of Eq.(2.12) while Lyapunov and Halo ones derive from its third order approximation. However all the analytical solutions are not accurate enough to catch the advocated trajectory due to the high

non-linearity behaviour of the equations; a numerical scheme is thus required to refine the analytical solution and get the desired trajectory.

Scope of this section is to briefly summarize the procedure adopted to define and design of such typologies of orbits.

Lissajous Orbit

The analytical formulation of *Small-Size Lissajous Orbits* comes directly from the linearized EoMs [44]:

in order to study the motion around any of the Libration points $L(a, b)$ (where a and b are the coordinates of the Libration points in the co-rotating, dimensioneless system, whose values are listed in Tab.(2.1) and Tab.(2.2)), a new set of coordinates (ξ, η, ζ) is introduced such that:

$$\xi = x - a \qquad \eta = y - b \qquad \zeta = z \tag{2.21}$$

Moreover, the function U is expanded as a Taylor series around L giving:

$$\begin{aligned} U = U(a,b) + U_x(a,b)\xi + U_y(a,b)\eta + \frac{1}{2}U_{xx}(a,b)\xi^2 + U_{xy}(a,b)\xi\eta \\ + U_{xz}(a,b)\xi\zeta + \frac{1}{2}U_{yy}(a,b)\eta^2 + U_{yz}(a,b)\eta\zeta + \frac{1}{2}U_{zz}(a,b)\zeta^2 + \mathcal{O}(3) \end{aligned} \tag{2.22}$$

Substituting Eq.(2.21) and Eq.(2.22) in Eq.(2.12) and neglecting higher order terms, Eq.(2.12) takes the form of a set of *linear variational equations* which, using the state space formalism, reads:

$$\dot{\boldsymbol{x}} = \boldsymbol{A}\boldsymbol{x} \tag{2.23}$$

where

$$\boldsymbol{x} = \begin{bmatrix} \xi \\ \eta \\ \zeta \\ \dot{\xi} \\ \dot{\eta} \\ \dot{\zeta} \end{bmatrix} \qquad \boldsymbol{A} = \begin{bmatrix} \boldsymbol{0_{3x3}} & \boldsymbol{I_{3x3}} \\ \boldsymbol{U_{ij}} & \boldsymbol{C} \end{bmatrix} \qquad \boldsymbol{U_{ij}} = \begin{bmatrix} U^0_{xx} & U^0_{xy} & U^0_{xz} \\ U^0_{yx} & U^0_{yy} & U^0_{yz} \\ U^0_{zx} & U^0_{zy} & U^0_{zz} \end{bmatrix} \qquad \boldsymbol{C} = \begin{bmatrix} 0 & -2 & 0 \\ 2 & 0 & 0 \\ 0 & 0 & 0 \end{bmatrix} \tag{2.24}$$

and $U^0_{ij} = U_{ij}(a, b)$.

The solution of Eq.(2.23) is of the form:

$$\begin{aligned} \xi &= \sum_{i=1}^{4} A_i e^{\lambda_i t} \\ \eta &= \sum_{i=1}^{4} B_i e^{\lambda_i t} \\ \zeta &= \sum_{i=5}^{6} C_i e^{\lambda_i t} \end{aligned} \tag{2.25}$$

where

$$\lambda_{1,2} = \pm\sqrt{-2 + \frac{U^0_{xx} + U^0_{yy}}{2} + \sqrt{\left(\frac{U^0_{xx} + U^0_{yy}}{2}\right)^2 + (U^0_{xx}U^0_{yy})^2}} = \pm\lambda \qquad \in \quad \mathbb{R} \tag{2.26a}$$

$$\lambda_{3,4} = \pm i\sqrt{+2 - \frac{U^0_{xx} + U^0_{yy}}{2} + \sqrt{\left(\frac{U^0_{xx} + U^0_{yy}}{2}\right)^2 + (U^0_{xx}U^0_{yy})^2}} = \pm i\omega \qquad \in \quad i\mathbb{R} \tag{2.26b}$$

$$\lambda_{5,6} = \pm i\sqrt{U^0_{zz}} = \pm i\nu \qquad \in \quad i\mathbb{R} \tag{2.26c}$$

and

$$B_i = \alpha_i A_i \qquad \alpha_i = \frac{\lambda_i^2 - U^0_{xx}}{2\lambda_i} \tag{2.27}$$

where A_i and C_i depend on initial conditions.

As evidenced by Eq.(2.25) and Eq.(2.26) the motion in the z-axis is decoupled by the one in x-y plane. Each λ_i is an eigenvalue of matrix A and, considering Eq.(2.26a), the here-discussed family of orbit is naturally unstable as generally presents an eigenvalue (λ_1) whose real part is grater than zero. Nevertheless it is possible to properly tune the initial condition such that $A_1 = A_2 = 0$ by setting:

$$\dot{\xi} = \frac{\eta_0 \lambda_3}{\alpha_3} \qquad \dot{\eta} = \alpha_3 \lambda_3 \xi_0 \tag{2.28}$$

The result is a periodic motion both in x-y plane and z-axis, as $\lambda_{3,4,5,6}$ are purely imaginary numbers, and an overall quasi-periodic motion is achieved as the oscillation frequencies ω and ν are in general rationally independent.

The quasi-periodic solution might be expressed as Eq.(2.29) by applying Eq.(2.21) to Eq.(2.25), where $A_{x,z}$ represents the oscillation amplitude in the x,z direction with respect to the Lagrangian point position and $k = \alpha_3$.:

$$\begin{cases} x = -A_x cos(\omega t + \phi) & \text{(2.29a)} \\ y = k A_x sin(\omega t + \phi) & \text{(2.29b)} \\ z = A_z sin(\nu t + \psi) & \text{(2.29c)} \end{cases}$$

Lyapunov and Halo Orbits

As demonstrated previously, the linearized EoMs allow stable motion under a proper tuning of the initial conditions. Moreover the in-plane motion and the out of plane motion are characterized by rationally independent oscillation frequencies (ω for the x-y dynamics and ν for the out of plane dynamics), resulting in a quasi-periodic 3D dynamics. Lyapunov and Halo orbits are periodic orbit around Libration points which exploit the non-linear contribution of the system to produce equal eigen-frequencies. The analytical definition refers to the work carried out by Richardson [36] for the design of the nominal orbit of the ISEE-3 mission. The difference between Lyapunov and Halo trajectories relies on the excursion on the out of plane direction: Lyapunov orbits are planar, Halo orbits

are fully three dimensional.

The EoMs are firstly expanded in a truncated third order Linsted-Pointcaré series and then the frequencies corrections are used to cancel out the secular terms appearing in the equations. The complete procedure is presented in [36]. The final, third order solution is:

$$\begin{aligned} x = {} & a_{21}A_x^2 + a_{22}A_z^2 - A_x cos(\omega t + \phi) + (a_{23}A_x^2 - a_{24}A_z^2)cos(2\omega t + \phi) \\ & + (a_{31}A_x^3 - a_{32}A_x A_z^2)cos(3\omega t + \phi) \end{aligned} \tag{2.30a}$$

$$\begin{aligned} y = {} & kA_x sin(\omega t + \phi) + (b_{21}A_x^2 - b_{22}A_z^2)sin(2\omega t + \phi) \\ & + (b_{31}A_x^3 - b_{32}A_x A_z^2)sin(3\omega t + \phi) \end{aligned} \tag{2.30b}$$

$$\begin{aligned} z = {} & A_z cos(\omega t + \phi) + d_{21}A_x A_z(cos(2\omega t + \phi) - 3) \\ & + (d_{32}A_x A_x^2 - d_{31}A_z^3)cos(3\omega t + \phi) \end{aligned} \tag{2.30c}$$

where x, y, z, ω, ϕ, A_x, A_z and k refers to Eq.(2.29).

Moreover, for Halo orbits, a constraints between A_x and A_z is introduced and takes the form:

$$l_1 A_x^2 + l_2 A_z^2 + \Delta = 0 \tag{2.31}$$

All the coefficients l_1, l_2, Δ, a_{ij}, b_{ij}, d_{ij} are function of the dimensionless mass parameter μ introduced in Eq.(2.11). The complete definition of the coefficients can be found in [36].

Numerical Correction Scheme

As previously stated, the analytical solutions so far presented are not accurate enough to deal with the high non-linear behaviour of the system; if any state belonging to the analytical solution is used as initial conditions for the integration of the full EoMs (Eq.(2.12)), the simulation yields a divergent solution. Nevertheless, these initial conditions represents a good starting point for further corrections carried out by the *Shooting Technique* algorithm which is here discussed [8] [50].

The full EoMs, Eq.(2.12), present a symmetric behaviour such that given a solution expressed as $\boldsymbol{x}(t) = [\, x(t), y(t), z(t), \dot{x}(t), \dot{y}(t), \dot{z}(t) \,]$ it is guaranteed the existence of a second solution $\boldsymbol{x}(-t) = [\, x(-t), y(-t), z(-t), \dot{x}(-t), \dot{y}(-t), \dot{z}(-t) \,]$. Thus a trajectory that crosses perpendicularly the $y = 0$ plane twice is a periodic orbit [50].

So let's consider a first guess for the initial conditions $\boldsymbol{x_0} = [\, x_0, 0, z_0, 0, \dot{y}_0, 0 \,]$ whose components come directly from the analytical solutions; the shooting technique method exploits the symmetry property to correct $\boldsymbol{x_0}$ in order to have an orbit which crosses perpendicularly the $y = 0$ plane, thus a periodic orbit.

In order to express it, the *flow operator* $\Phi(\boldsymbol{x_0}, t)$ definition is introduced, Eq.(2.32), as well as its first order expansion, Eq.(2.33):

$$\boldsymbol{x}(t) = \Phi(\boldsymbol{x_0}, t) \tag{2.32}$$

$$\Phi(\boldsymbol{x_0} + \boldsymbol{\Delta x}, T + \Delta t) = \Phi(\boldsymbol{x_0}, T) + \Big[\frac{\partial \Phi(\boldsymbol{x_0}, T)}{\partial \boldsymbol{x}}\Big]\boldsymbol{\Delta x} + \Big[\frac{\partial \Phi(\boldsymbol{x_0}, T)}{\partial t}\Big]\Delta t \tag{2.33}$$

where T is the time of the first return to the x-z plane of the flow operator, i.e:

$$\Phi(\boldsymbol{x_0}, T) = [\, \bar{x}, 0, \bar{z}, \dot{\bar{x}}, \dot{\bar{y}}, \dot{\bar{z}} \,] \tag{2.34}$$

In Eq.(2.33) it appears the *State Transition Matrix (STM)* $\boldsymbol{\Psi}(t)$, called *Monodromy Matrix* for periodic systems, whose definition and its dynamics are expressed by Eq.(2.35) and Eq.(2.36):

$$\boldsymbol{\Psi}(t) = \frac{\partial \Phi(\boldsymbol{x_0}, t)}{\partial \boldsymbol{x}} \tag{2.35}$$

$$\frac{\partial \boldsymbol{\Psi}(t)}{\partial t} = \boldsymbol{F}\boldsymbol{\Psi}(t) \tag{2.36}$$

By imposing $\Phi(\boldsymbol{x_0} + \boldsymbol{\Delta x}, T + \Delta t)$ to match the periodicity condition in Eq., i.e.

$$\Phi(\boldsymbol{x_0} + \boldsymbol{\Delta x}, T + \Delta t) = [\, x', 0, z', 0, \dot{y}', 0 \,]' \tag{2.37}$$

and considering the equations where the components of $\Phi(\boldsymbol{x_0} + \boldsymbol{\Delta x}, T + \Delta t)$ are zero,

the problem might be re-formulated as:

$$\boldsymbol{A}\boldsymbol{\Delta x}^* = \boldsymbol{b} \tag{2.38}$$

$$\boldsymbol{A} = \begin{bmatrix} \Psi_{21} & \Psi_{25} & \dot{\bar{y}} \\ \Psi_{41} & \Psi_{45} & \ddot{\bar{x}} \\ \Psi_{61} & \Psi_{65} & \ddot{\bar{z}} \end{bmatrix} \quad \boldsymbol{\Delta x}^* = \begin{bmatrix} \Delta x \\ \Delta \dot{y} \\ \Delta t \end{bmatrix} \quad \boldsymbol{\Delta b} = \begin{bmatrix} 0 \\ -\dot{\bar{x}} \\ -\dot{\bar{z}} \end{bmatrix}$$

where no correction on z_0 are imposed. Eq.(2.38) is then solved for $\boldsymbol{\Delta x}^*$ and the new initial condition for the iterative procedure is:

$$\boldsymbol{x_0^{new}} = \boldsymbol{x_0^{old}} + \boldsymbol{\Delta x}^* \tag{2.39}$$

until the final accuracy is achieved.

Halo orbits computation follows exactly the so far presented procedure; otherwise Lyapunov orbits are planar so x_0 is imposed to have no corrections in Eq.(2.38) and thus the order of the system is reduced. At each iteration the *Shooting Technique* is required to integrate a differential system of order $n + n^2$ (EoMs and STM dynamics); for halo orbits the full order is 42 while for Lyapunov orbits it is equal to 20.

2.1.5 Results

The three orbit types are computed around the Libration Point L_1 of both the *Earth-Moon System* and $Sun - Earth/Moon$ system.

2.1.6 Lissajous Orbits

Two Lissajous orbits are simulated according to the procedure presented in Section 2.1.4.

A_x [Km]	A_z [Km]	ω $[\frac{rad}{s}]$	ν $[\frac{rad}{s}]$	C
4000	1000	2.334	2.2688	3.194

Table 2.3: Orbit parameters for the Earth-Moon L_1 Lissajous Orbit.

A_x [Km]	A_z [Km]	ω $[\frac{rad}{s}]$	ν $[\frac{rad}{s}]$	C
40000	10000	2.0864	2.0152	3.001

Table 2.4: Orbit parameters for the Sun-Earth/Moon L_1 Lissajous Orbit.

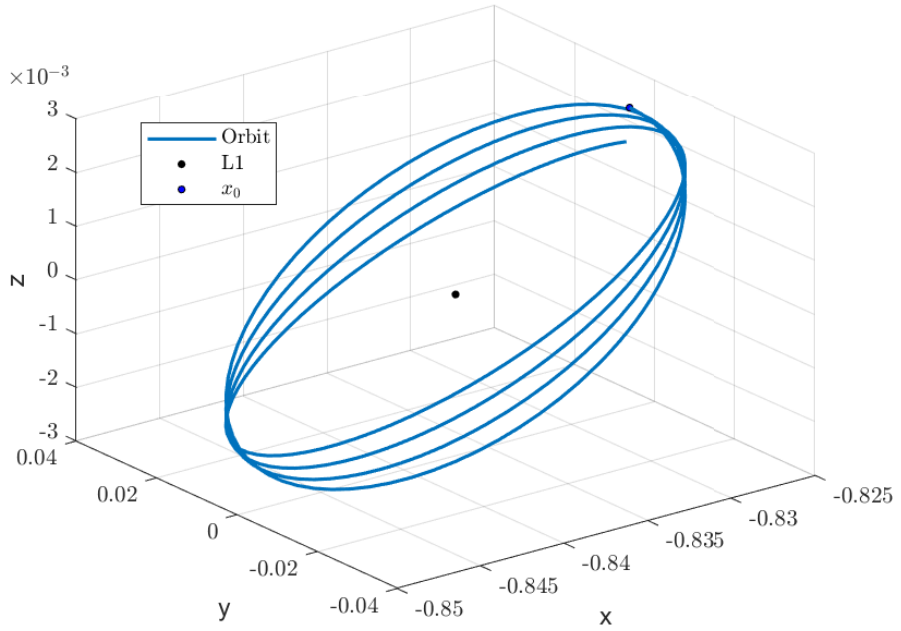

Figure 2.3: Lissajous Orbit around Earth-Moon L_1 Lagrangian point in adimensional coordinates.

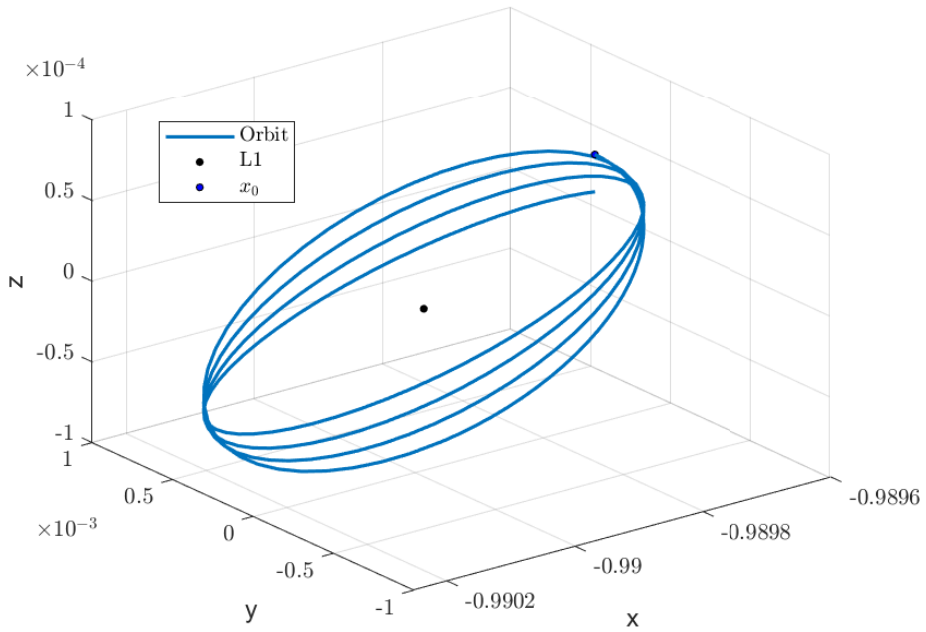

Figure 2.4: Lissajous Orbit around Sun-Earth/Moon L_1 Lagrangian point in adimensional coordinates.

2.1.7 Lyapunov and Halo Orbits

A set of Planar Lyapunov and Halo orbits is presented for both the Earth-Moon and Sun-Earth/Moon system around the Lagrangian point L_1. The orbits are parameterised as function of their respective Jacobi constant value.

Halo Orbits

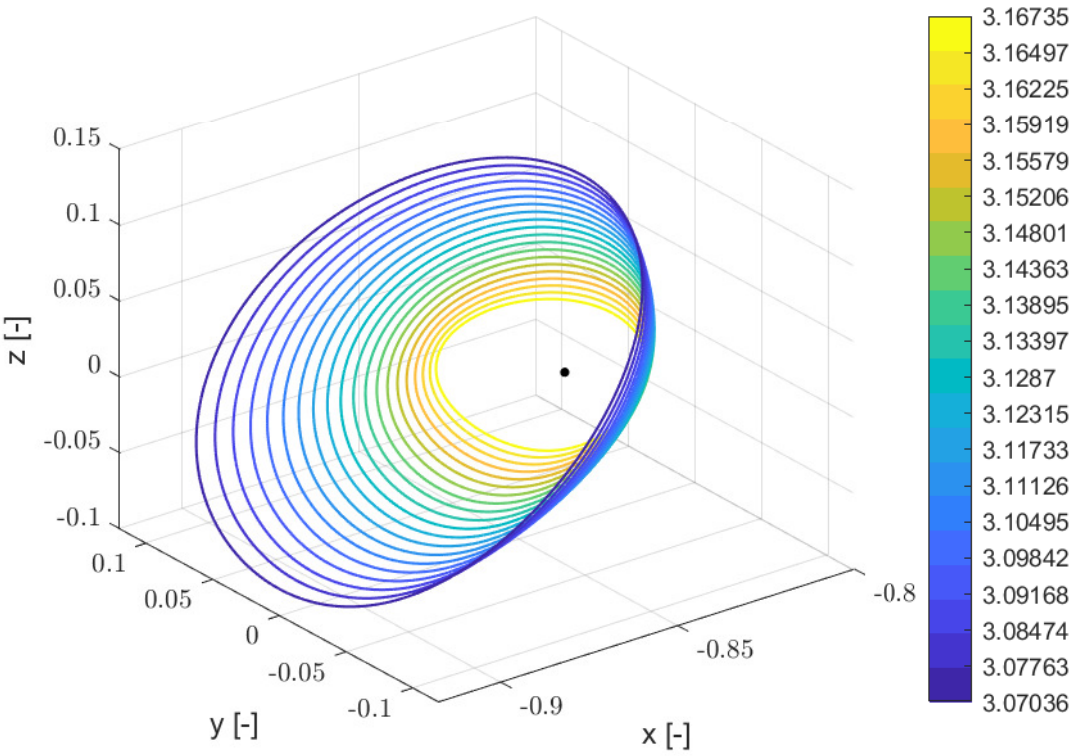

Figure 2.5: Halo Orbits around Earth-Moon L_1. The color-bar refers to the Jacobi constant.

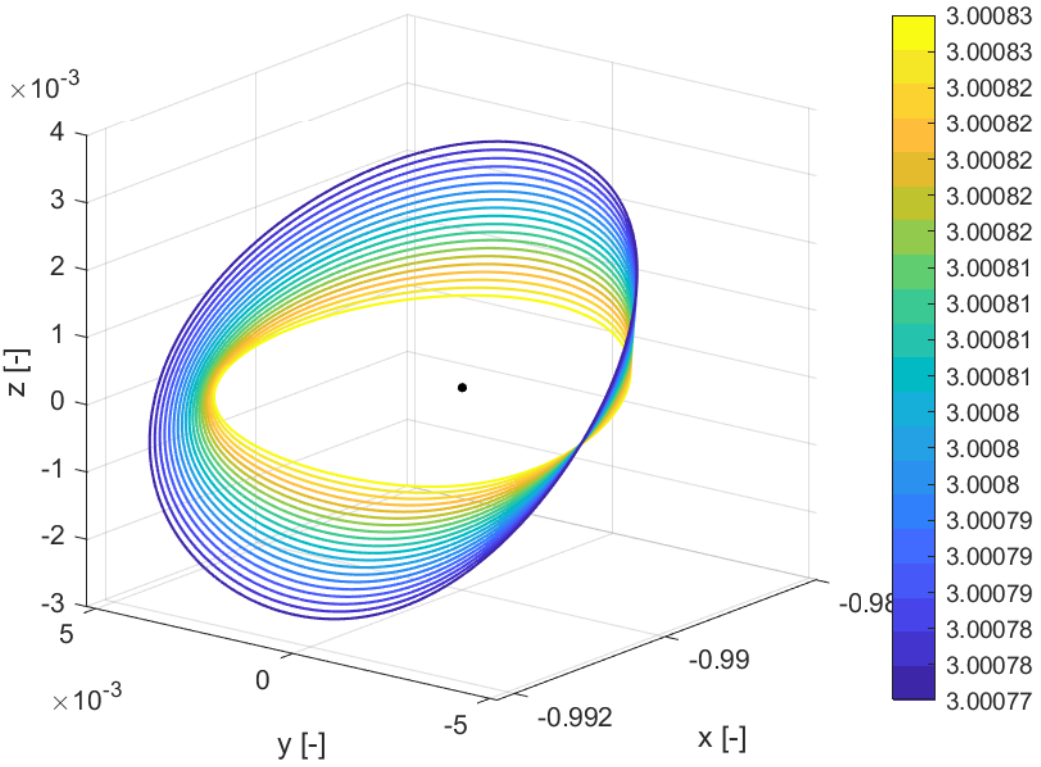

Figure 2.6: Halo Orbits around Sun-Earth/Moon L_1. The color-bar refers to the Jacobi constant.

C	Period	x_0	z_0	v_0
3.167352	2.748506	-0.8234	0.0288	-0.1390
3.164973	2.750344	-0.8235	0.0334	-0.1430
3.162251	2.752424	-0.8235	0.0381	-0.1474
3.159189	2.754729	-0.8236	0.0429	-0.1521
3.155791	2.757242	-0.8238	0.0477	-0.1572
3.152061	2.759942	-0.8239	0.0525	-0.1624
3.148007	2.762799	-0.8242	0.0574	-0.1679
3.143634	2.765780	-0.8244	0.0623	-0.1735
3.138952	2.768844	-0.8247	0.0673	-0.1792
3.133969	2.771941	-0.8251	0.0724	-0.1850
3.128697	2.775011	-0.8255	0.0775	-0.1908
3.123146	2.777981	-0.8260	0.0826	-0.1967
3.117329	2.780763	-0.8265	0.0879	-0.2025
3.111259	2.783251	-0.8271	0.0932	-0.2082
3.104950	2.785315	-0.8278	0.0985	-0.2139
3.098418	2.786798	-0.8285	0.1039	-0.2195
3.091677	2.787507	-0.8293	0.1094	-0.2249
3.084743	2.787202	-0.8301	0.1149	-0.2302
3.077632	2.785585	-0.8311	0.1205	-0.2353
3.070360	2.782278	-0.8321	0.1262	-0.2403

Table 2.5: Orbit parameters of the Halo Orbit family in the Earth-Moon system presented in Fig.(2.5)

C	Period	x_0	z_0	v_0
3.000827	3.059721	-0.988836	0.000768	-0.008928
3.000826	3.059571	-0.988838	0.000890	-0.008960
3.000824	3.059399	-0.988840	0.001012	-0.008997
3.000823	3.059203	-0.988843	0.001135	-0.009038
3.000821	3.058983	-0.988846	0.001257	-0.009083
3.000819	3.058739	-0.988849	0.001380	-0.009133
3.000817	3.058471	-0.988852	0.001504	-0.009186
3.000814	3.058177	-0.988856	0.001627	-0.009244
3.000812	3.057856	-0.988861	0.001751	-0.009306
3.000809	3.057509	-0.988865	0.001875	-0.009371
3.000806	3.057134	-0.988871	0.002000	-0.009440
3.000803	3.056731	-0.988876	0.002126	-0.009513
3.000800	3.056298	-0.988883	0.002252	-0.009589
3.000796	3.055834	-0.988889	0.002378	-0.009669
3.000792	3.055338	-0.988897	0.002505	-0.009751
3.000789	3.054809	-0.988905	0.002632	-0.009837
3.000785	3.054246	-0.988913	0.002760	-0.009926
3.000780	3.053647	-0.988922	0.002888	-0.010017
3.000776	3.053011	-0.988932	0.003017	-0.010111
3.000771	3.052336	-0.988943	0.003147	-0.010207

Table 2.6: Orbit parameters of the Halo Orbit family in the Sun-Earth/Moon system presented in Fig.(2.6)

Planar Lyapunov Orbits

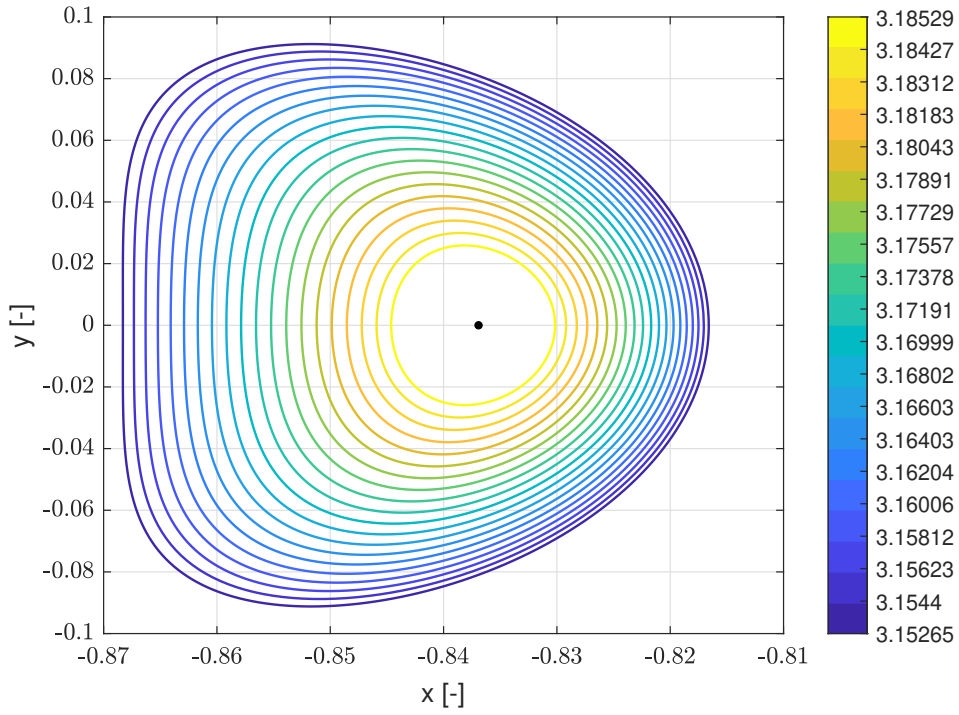

Figure 2.7: Planar Lyapunov Orbits around Earth-Moon L_1. The color-bar refers to the Jacobi constant.

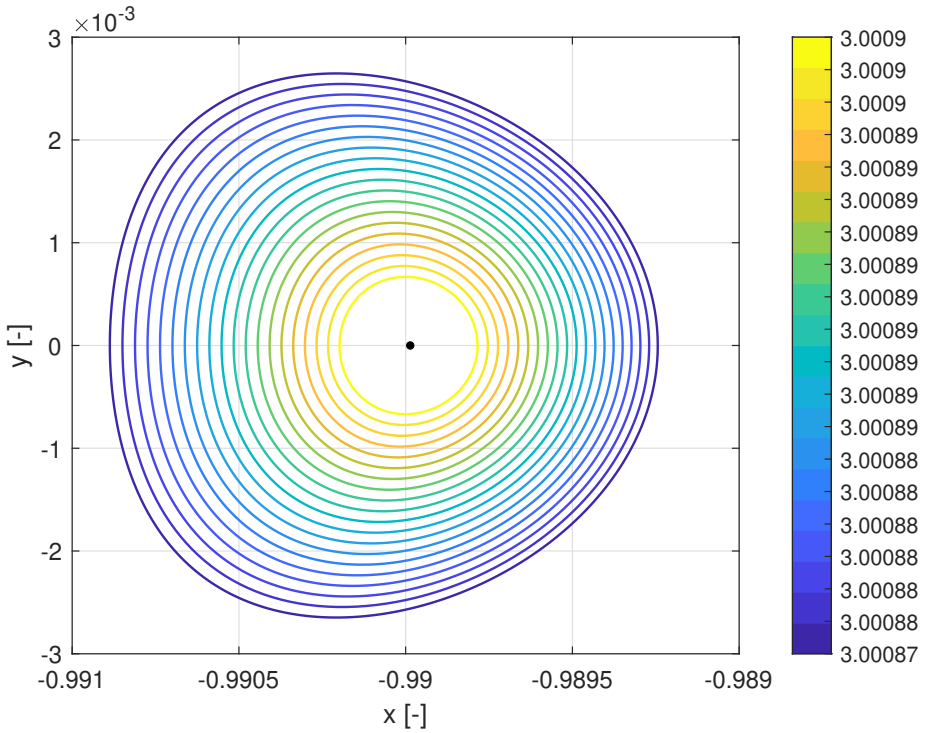

Figure 2.8: Planar Lyapunov Orbits around Sun-Earth/Moon L_1. The color-bar refers to the Jacobi constant.

C	**Period**	x_0	v_0
3.185289	2.702407	-0.830159	-0.059617
3.184270	2.706069	-0.829187	-0.068746
3.183116	2.710245	-0.828241	-0.077767
3.181833	2.714925	-0.827323	-0.086668
3.180428	2.720092	-0.826431	-0.095434
3.178910	2.725729	-0.825568	-0.104052
3.177288	2.731814	-0.824733	-0.112505
3.175572	2.738318	-0.823926	-0.120778
3.173775	2.745212	-0.823148	-0.128855
3.171909	2.752458	-0.822399	-0.136712
3.169987	2.760014	-0.821680	-0.144356
3.168024	2.767836	-0.820991	-0.151740
3.166034	2.775870	-0.820332	-0.158863
3.164033	2.784060	-0.819704	-0.165706
3.162036	2.792346	-0.819107	-0.172255
3.160058	2.800663	-0.818542	-0.178493
3.158117	2.808945	-0.818008	-0.184408
3.156225	2.817121	-0.817506	-0.189987
3.154399	2.825122	-0.817036	-0.195218
3.152651	2.832876	-0.816600	-0.200092

Table 2.7: Orbit parameters of the Planar Lyapunov family in the Earth-Moon system presented in Fig.(2.7)

C	**Period**	x_0	v_0
3.000897	3.011429	-0.989965	-0.000139
3.000897	3.011433	-0.989962	-0.000161
3.000897	3.011437	-0.989959	-0.000183
3.000897	3.011442	-0.989955	-0.000205
3.000897	3.011447	-0.989952	-0.000227
3.000897	3.011453	-0.989949	-0.000249
3.000897	3.011459	-0.989946	-0.000271
3.000897	3.011466	-0.989942	-0.000293
3.000897	3.011473	-0.989939	-0.000315
3.000897	3.011481	-0.989936	-0.000337
3.000897	3.011489	-0.989933	-0.000359
3.000897	3.011498	-0.989930	-0.000381
3.000897	3.011508	-0.989926	-0.000402
3.000897	3.011518	-0.989923	-0.000424
3.000897	3.011528	-0.989920	-0.000446
3.000897	3.011539	-0.989917	-0.000468
3.000897	3.011551	-0.989913	-0.000490
3.000897	3.011563	-0.989910	-0.000512
3.000897	3.011576	-0.989907	-0.000534
3.000897	3.011589	-0.989904	-0.000556

Table 2.8: Orbit parameters of the Planar Lyapunov family in the Sun-Earth/Moon system presented in Fig.(2.7)

Chapter 3

Station-Keeping Strategy

Orbits around *Libration Points* generally presents an unstable behaviour; in the presence of systematic errors and uncertainties, as well as external perturbations, the free motion of the satellite tends to diverge from the desired nominal trajectory. An active *Station-Keeping Strategy* it is thus required to control the spacecraft in its motion around the *Lagrangian point*; part of the strategy objective is to optimize the fuel consumption needed to keep the spacecraft in a close vicinity of the orbit. The first part of the design of *High-Level Motion Control* is thus faced in this chapter. As stated in Section 1.1, the high-level motion control is devoted to the definition of the ideal commanded virtual control inputs required for station-keeping and attitude control purposes. This chapter is centered on the firsts.

Many strategies have been previously investigated by other authors; a detailed and exhaustive survey upon station-keeping techniques may be found in [28]. Among the wide set of strategies, the *Continuous Optimal Control Strategy*[2][9][32], based on *Linear Quadratic (Gaussian) Regulator (LQG/LQR)* is addressed in this study. It is based on *Optimal Control Theory* which enables the designer to perform trade-offs between fuel consumption and tightness of the control. Moreover it represents the baseline method which more sophisticated algorithms are based on. The continuous optimal control algorithm computes low-thrust continuous control during the whole duration of the mission (eventually switched on-off by a *"Bang-Bang Controller"* when some conditions are satisfied) which makes it the ideal candidate for electric propulsion based *Attitute & Orbit Control System*

(AOCS). Moreover it must be capable of handling bounded external perturbations, as well as tracking and control execution errors.

3.1 Continuous Optimal Control

In the context of *Optimal Control Theory*, the problem of designing a particular control law forcing the system to follow a particular reference trajectory is known as *Tracking Problem*. The nominal trajectory is supposed to be known a priori for each time instant. It is firstly required to linearise the dynamics of the spacecraft, Eq.(2.12), with respect to the nominal orbit, Eq.(3.1a), by introducing the *deviation vector* $\delta\boldsymbol{r}$, Eq.(3.1b)

$$\delta\ddot{\boldsymbol{r}}(t) = -2\hat{k} \times \delta\dot{\boldsymbol{r}}(t) + \boldsymbol{U_{rr}}(t)\delta\boldsymbol{r}(t) + \boldsymbol{e}(t) + O(\delta\boldsymbol{r})^2 \tag{3.1a}$$

$$\delta\boldsymbol{r}(t) = \begin{bmatrix} x(t) - x_r(t) \\ y(t) - y_r(t) \\ z(t) - z_r(t) \end{bmatrix} \tag{3.1b}$$

where $x_r(t)$, $y_r(t)$, $z_r(t)$ are the non-dimensional coordinates of the reference orbit at time t while $\boldsymbol{U_{rr}}(t)$ and $\boldsymbol{e}(t)$ are defined as:

$$\boldsymbol{U_{rr}}(t) = \begin{bmatrix} U^*_{xx} & U^*_{xy} & U^*_{xz} \\ U^*_{yx} & U^*_{yy} & U^*_{yz} \\ U^*_{zx} & U^*_{zy} & U^*_{zz} \end{bmatrix} \quad \boldsymbol{e}(t) = \nabla U|_{\boldsymbol{x_r}} - -2\hat{k} \times \delta\dot{\boldsymbol{r}}_{\boldsymbol{n}}(t) - \ddot{\boldsymbol{r}}_{\boldsymbol{n}} \tag{3.2}$$

with $U^*_{ij} = U_{ij}|_{\boldsymbol{x_r}}$

By doing so, Eq.(3.1a) might be reformulated in the usual state space formulation for a *Linear Time Variant (LTV) System*, Eq.(3.3)

$$\dot{\boldsymbol{x}} = \boldsymbol{F}(t)\boldsymbol{x} + \boldsymbol{G}(t)\boldsymbol{u} + \boldsymbol{E}(t) \tag{3.3}$$

where

$$\boldsymbol{x} = \begin{bmatrix} \delta\boldsymbol{r} \\ \delta\dot{\boldsymbol{r}} \end{bmatrix} \boldsymbol{F}(t) = \begin{bmatrix} \boldsymbol{0}_{3x3} & \boldsymbol{I}_{3x3} \\ \boldsymbol{U_{rr}} & 2\boldsymbol{\Omega} \end{bmatrix} \boldsymbol{\Omega} = \begin{bmatrix} 0 & -2 & 0 \\ 2 & 0 & 0 \\ 0 & 0 & 0 \end{bmatrix} \boldsymbol{E}(t) = \begin{bmatrix} \boldsymbol{0}_{3x1} \\ \boldsymbol{e} \end{bmatrix} \boldsymbol{G}(t) = \begin{bmatrix} \boldsymbol{0}_{3x1} \\ \boldsymbol{I}_{3x1} \end{bmatrix} \tag{3.4}$$

It has to be noticed that $\boldsymbol{F}(t)$ and $\boldsymbol{E}(t)$ are periodic with the orbit period T, and for the expression of $\boldsymbol{G}(t)$ three-axes control is assumed. Regarding the error matrix $\boldsymbol{E}(t)$, as well as the error vector $\boldsymbol{e}(t)$, they account for the error on the acceleration on the analytical expression of the nominal orbit [9]; in the case the nominal orbit is computed through a numerical procedure they become equal to zero and disappear from Eq.(3.3).

The tracking problem is intended to find the optimal control $\boldsymbol{u}^*$ such that the *cost function* J, defined in Eq.(3.5), is minimised [3].

$$J = \int_{t_0}^{t_f} \frac{1}{2} \left[\boldsymbol{x}'\boldsymbol{Q}\boldsymbol{x} + \boldsymbol{u}'\boldsymbol{R}\boldsymbol{u} \right] dt + \boldsymbol{x}'(t_f)\boldsymbol{H}\boldsymbol{x}(t_f) \tag{3.5}$$

In Eq.(3.5), $\boldsymbol{Q}$, $\boldsymbol{H}$ and $\boldsymbol{R}$ are appropriate weighting matrices. The solution of the problem takes the expression of:

$$\boldsymbol{u}^* = -\boldsymbol{K}(t)\boldsymbol{x} - \boldsymbol{\beta}(t) \tag{3.6}$$

where the *Gain matrix* $\boldsymbol{K}(t)$ and the *Bias correction* $\boldsymbol{\beta}(t)$ are computed as in Eq.(3.7a) and Eq.(3.7b).

$$\boldsymbol{K}(t) = \boldsymbol{R}^{-1}\boldsymbol{G}'\boldsymbol{S}(t) \tag{3.7a}$$

$$\boldsymbol{\beta}(t) = \boldsymbol{R}^{-1}\boldsymbol{G}'\boldsymbol{b}(t) \tag{3.7b}$$

$\boldsymbol{S}(t)$ is the solution of the *Periodic Algebraic Riccati Equation (PARE)*, Eq.(3.8), and $\boldsymbol{b}(t)$ is the solution of Eq.(3.9).

$$\dot{\boldsymbol{S}} + \boldsymbol{S}\boldsymbol{F} + \boldsymbol{F}'\boldsymbol{S} + \boldsymbol{Q} - \boldsymbol{S}\boldsymbol{G}\boldsymbol{R}^{-1}\boldsymbol{G}'\boldsymbol{S}' = \boldsymbol{0} \qquad \boldsymbol{S}(T) = \boldsymbol{H} \tag{3.8}$$

$$\dot{\boldsymbol{b}}' + \boldsymbol{b}'\big(\boldsymbol{F} - \boldsymbol{G}\boldsymbol{C}\big) - \boldsymbol{E}'\boldsymbol{S} = \boldsymbol{0} \qquad \boldsymbol{b}'(T) = \boldsymbol{0} \tag{3.9}$$

The device encharged of tune properly the control inputs is named *Regulator* and its performance quantity is represented by the *Gain Matrix* $\boldsymbol{K}$(t). Once $\boldsymbol{K}$(t) is computed according to the *Optimal Control Theory*, it is then referred to as *Linear Quadratic Regulator (LQR)*.

In the presence of disturbances and measurement errors, the precise state vector cannot be known, it is thus necessary to introduce a new element in the system control design, called *Observer*, whose role is to estimate the state reducing the noise influence. Among the several way to design the *Observer*, the one that is based on the minimization of a *quadratic cost function*, which weights the noise influence in terms of stochastic quantities, leads to the so called *Optimal Observer*, also known as *Kalman Filter*. The combination of the *Linear Quadratic Regulator (LQR)* and the *Kalman Filter* inside a control system is named *Linear Quadratic Gaussian Compensator*.

To design the regulator and the Kalman filter the reference equations are the *perturbed* EoMs, i.e. the standard EoMs of Eq.(3.3) where the *Gaussian White Noises*, ϵ and η, are introduced to perturb the output equation and the state itself. Eq.(3.3) then reads as Eq.(3.10):

$$\dot{\boldsymbol{x}} = \boldsymbol{F}\boldsymbol{x} + \boldsymbol{G}(\boldsymbol{u} + \boldsymbol{\epsilon}) \tag{3.10a}$$

$$\boldsymbol{y} = \boldsymbol{C}\boldsymbol{x} + \boldsymbol{\eta} \tag{3.10b}$$

Considering the design of the regulator in the presence of stochastic quantities, the cost function of Eq.(3.5) is reformulated as $J = E[\boldsymbol{x}'\boldsymbol{Q}\boldsymbol{x} + \boldsymbol{u}'\boldsymbol{R}\boldsymbol{u}]$, where $E[-]$ is the *Expected Value* operator. The solution to the minimization problem leads to the same solution that

for the deterministic case, the same $\boldsymbol{K}$ matrix solution of Eq.(3.8). The optimal control input is now defined thus as Eq.(3.11):

$$\boldsymbol{u}^* = -\boldsymbol{K}(t)\hat{\boldsymbol{x}} \tag{3.11}$$

where $\hat{\boldsymbol{x}}$ is the *Estimated State* coming from the observer. The observer state space dynamics, which express the evolution of the estimation in time, is represented by Eq.(3.12)

$$\dot{\hat{\boldsymbol{x}}} = \hat{\boldsymbol{F}}\hat{\boldsymbol{x}} + \hat{\boldsymbol{G}}\boldsymbol{u} + \boldsymbol{L}\boldsymbol{y} \tag{3.12}$$

with $\hat{\boldsymbol{F}}$ and $\hat{\boldsymbol{G}}$ are the state space matrix of the observer and $\boldsymbol{L}$ is the observer design matrix. The *estimation error* is introduced as $\boldsymbol{e} = \boldsymbol{x} - \hat{\boldsymbol{x}}$ and its dynamics reads as Eq.(3.13).

$$\dot{\boldsymbol{e}} = (\boldsymbol{F} - \boldsymbol{L}\boldsymbol{C})\boldsymbol{e} + \boldsymbol{G}\boldsymbol{\epsilon} + \boldsymbol{L}\boldsymbol{\eta} \tag{3.13}$$

It has to be noticed that in Eq.(3.13), it is imposed that $\hat{\boldsymbol{F}} = \boldsymbol{F} - \boldsymbol{L}\boldsymbol{C}$ and $\hat{\boldsymbol{G}} = \boldsymbol{G}$ in order to avoid the error evolution to depend directly from the state or the input.
The *quadratic cost function* associated to the observer is then defined as:

$$J_{obs} = E[\boldsymbol{e}'\boldsymbol{e}] \tag{3.14}$$

and its minimization yields the optimal values of the design matrix $\boldsymbol{L}$, expressed in Eq.(3.15a), with $\boldsymbol{P}$ the solution of the Riccati Equation Eq(3.15b).

$$\boldsymbol{L} = \boldsymbol{P}\boldsymbol{C}'\boldsymbol{W}_{nn}^{-1} \tag{3.15a}$$

$$\dot{\boldsymbol{P}} = \boldsymbol{F}\boldsymbol{P} + \boldsymbol{P}\boldsymbol{F}' + \boldsymbol{G}\boldsymbol{W}_{\epsilon\epsilon}\boldsymbol{G}' - \boldsymbol{P}\boldsymbol{C}'\boldsymbol{W}_{nn}^{-1}\boldsymbol{C}\boldsymbol{P} \quad \boldsymbol{P}(0) = \boldsymbol{\sigma}_{\boldsymbol{e}\boldsymbol{e}}(0) \tag{3.15b}$$

In Eq.(3.15), $\boldsymbol{W}_{nn}$ and $\boldsymbol{W}_{\epsilon\epsilon}$ are the *Covariance Matrices* of, respectively, η and ϵ.

3.1.1 Numerical Implementation

The *Linear Quadratic Gaussian (LQG)* regulator is implemented for all the orbit families presented in Section 2. The control execution errors as well as the tracking errors are implemented in the algorithm as *White Gaussian Noise (WGN)* whose standard deviations are listed in Tab.(3.1). By doing so, the control inputs and the state measurement become stochastic quantities having a *Mean Value* μ determined by the algorithm with a standard deviation σ determined by the perturbation itself.

Uncertainty on	**Symbol**	**Value**
Position along x	σ_{xx}	1.5 [Km]
Position along y	σ_{yy}	2.5 [Km]
Position along z	σ_{zz}	15 [Km]
Velocity along $\dot{x}$	$\sigma_{\dot{x}\dot{x}}$	1 $\left[\frac{mm}{s}\right]$
Velocity along $\dot{y}$	$\sigma_{\dot{y}\dot{y}}$	1 $\left[\frac{mm}{s}\right]$
Velocity along $\dot{z}$	$\sigma_{\dot{z}\dot{z}}$	3 $\left[\frac{mm}{s}\right]$
Control input u_x u_y u_z	σ_{uu}	10^{-9} [g]

Table 3.1: Standard deviations of control execution and tracking errors.

The choice of the values presented in Tab.(3.1) is consistent with [9] [22] [25]. For each orbit type, a particular reference orbit is chosen as nominal path in order to compare the results to a specific reference. The results of a sample simulation are then given to demonstrate the efficacity of the method.

Halo Family

It is chosen, as nominal path, a Southern Halo Orbit around the Earth-Moon Lagrangian point L_1 whose parameters are listed in Tab.(3.2).

C	**Period**	$\boldsymbol{x_0}$	$\boldsymbol{z_0}$	$\boldsymbol{v_0}$	$\boldsymbol{A_z}$ [Km]
3.05811	2.7719	-0.833951	-0.135648	-0.247853	42592

Table 3.2: Orbit Parameter of the nominal Halo orbit.

The orbit in consideration is selected in order to compare the results with [32]. The set-up of the control algorithm is consistent with [32] and its parameters are listed in Tab.(3.3). It is introduced an initial deviation δx_0 to simulate a potential injection that might occur during the orbit insertion.

Parameter	**Value**
Q	diag([2.25; 2.25; 1.75; 1.75; 1.25; 1.25])
R	diag([0.0002; 0.034; 0.034])
H	diag([2.25; 2.25; 1.75; 1.75; 1.25; 1.25])
δx_0	[0.0005;-0.0005;-0.0005;-0.0130;-0.0005;0.0005]
Integration Time	5.06 [-] / 22 days

Table 3.3: LQG and simulation set up for the continuous optimal control

The nominal orbit representation, as well as the evolution in time of the control inputs, deviations and error estimations in positions and velocities are presented from Fig.(3.1) to Fig.(3.6).

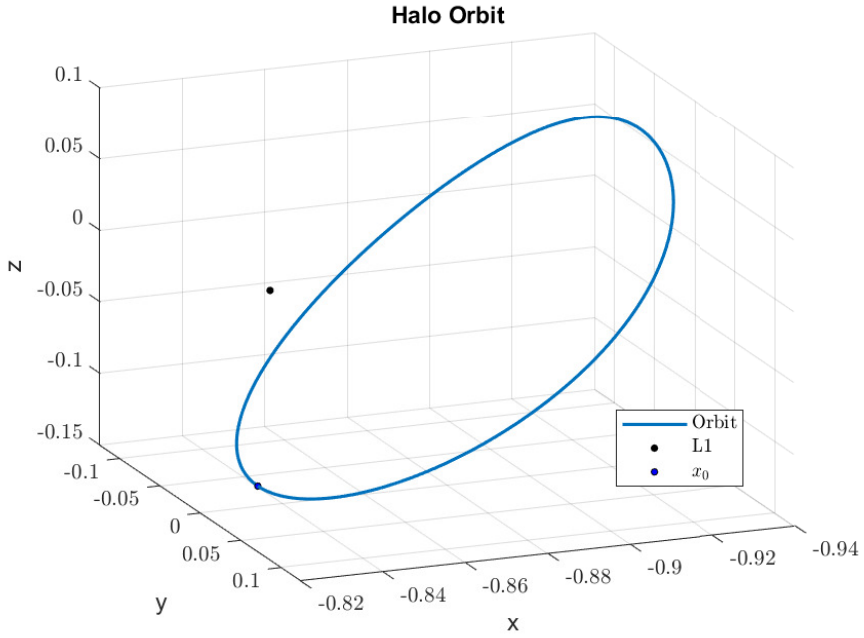

Figure 3.1: Reference Halo Orbit for the LQG

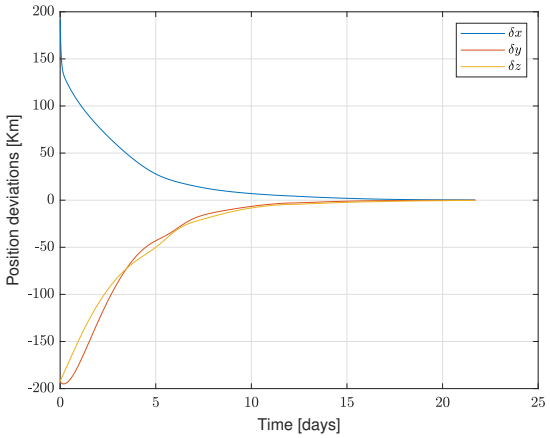

Figure 3.2: Position deviation evolution in time.

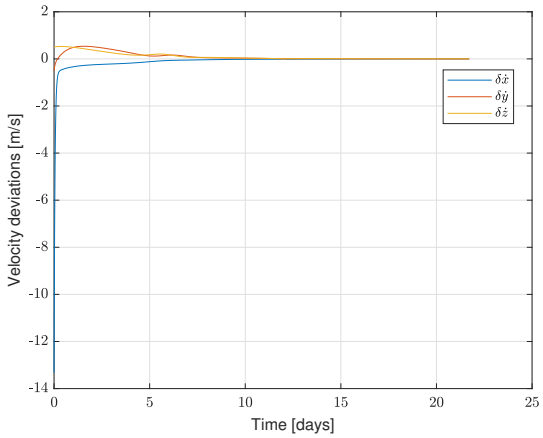

Figure 3.3: Velocity deviation evolution in time.

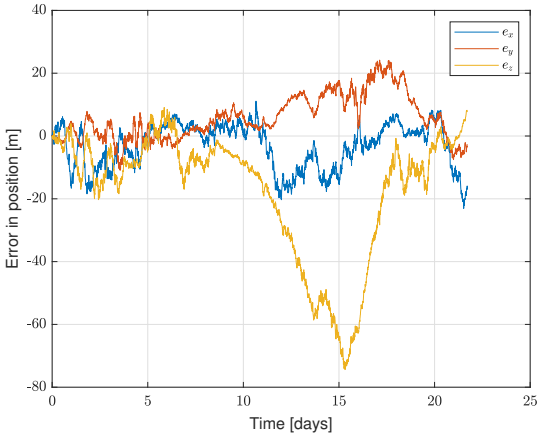

Figure 3.4: Estimation error in position.

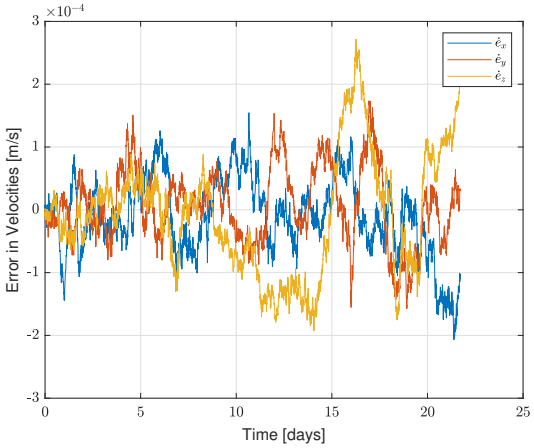

Figure 3.5: Estimation error in velocity.

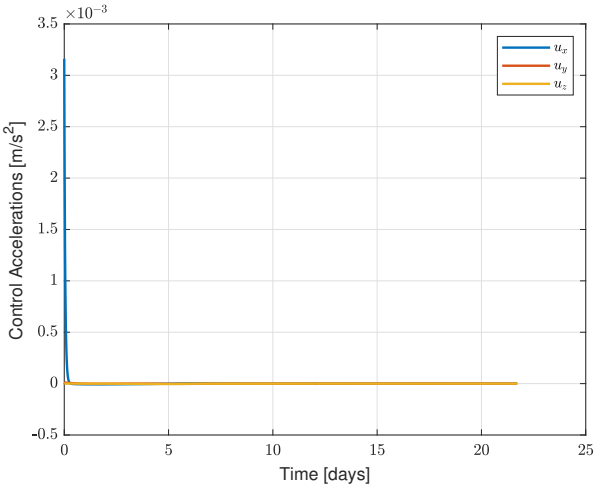

Figure 3.6: Control inputs evolution in time.

The total cost in terms of control effort is $\Delta V = 15.4301\ [\frac{m}{s}]$. The deviation from the

nominal state, both in terms of position and velocity, converge to zero with an approximate settling time of one orbit period (T = 2.7719, i.e. 12 days). The error on the estimation remains bounded close to zero.

Lyapunov Family

The Planar Lyapunov orbit of Fig.(3.7), determined by the parameters listed in Tab.(3.4), is chosen as the nominal trajectory for the LQG algorithm. It refers to the Earth-Moon Lagrangian point L_1 and its sizes are comparable to the reference Halo Orbit of [32].

C	**Period**	$\boldsymbol{x_0}$	$\boldsymbol{v_0}$	$\boldsymbol{A_y}$ [Km]
3.1442	2.872	-0.814621	-0.222206	50000

Table 3.4: Orbit Parameter of the nominal Lyapunov orbit.

Consistently with [32], the control parameters are selected as in Tab.(3.5).

Parameter	**Value**
Q	diag([2.25; 2.25; 1.75; 1.25])
R	diag([0.0002; 0.034])
H	diag([2.25; 2.25; 1.75; 1.25])
δx_0	[0.0005;-0.0005;-0.0130;-0.0005]
Integration Time	5.06 [-] / 22 days

Table 3.5: LQG and simulation set up for the continuous optimal control on Lyapunov orbit.

The results are presented from Fig.(3.8) to Fig.(3.12). It is worth underlining how the deviation from the nominal trajectory, both in terms of position and velocity, converge to zero with a settling time of around 12 day, around one orbit period. Also in this case, the state estimation is able to tackle the noise effects remaining bounded close to the real value ($\boldsymbol{e} \to 0$)

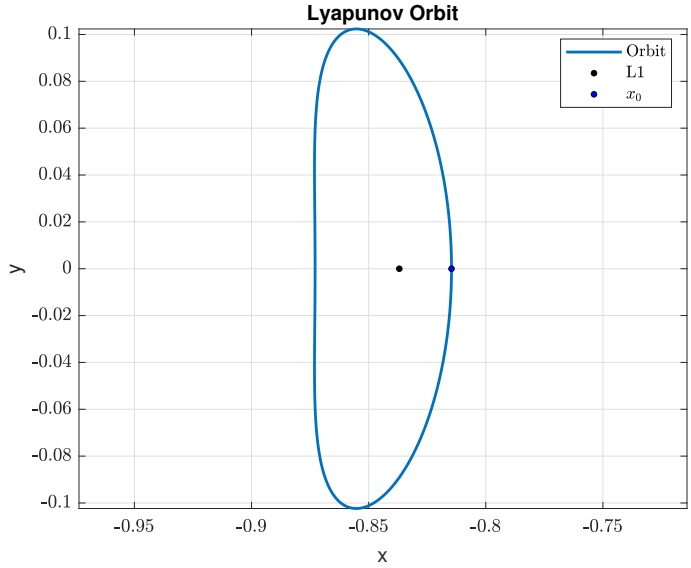

Figure 3.7: Reference Lyapunov Orbit for the LQG

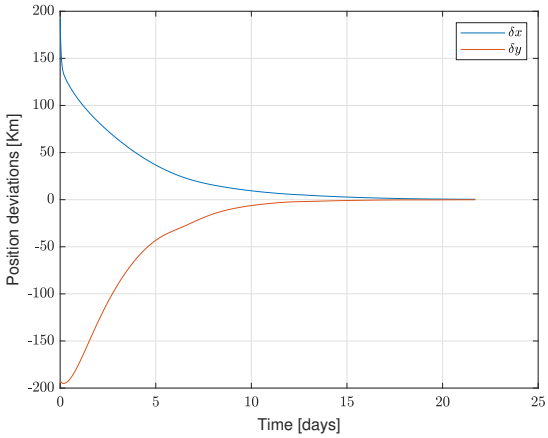

Figure 3.8: Position deviation evolution in time.

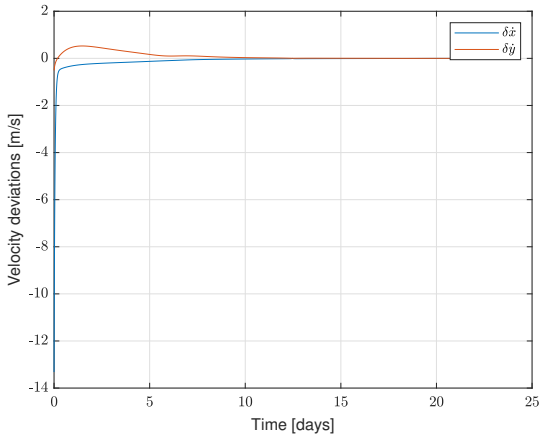

Figure 3.9: Velocity deviation evolution in time.

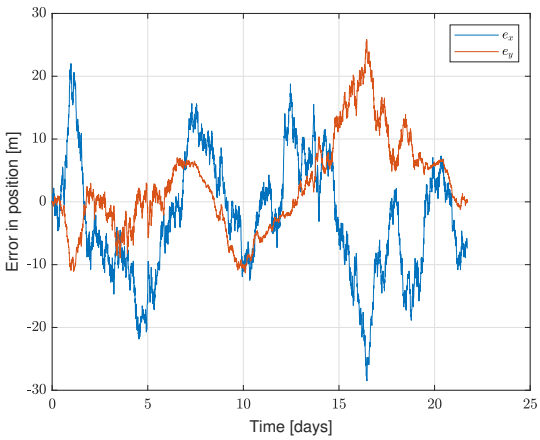

Figure 3.10: Estimation error in position.

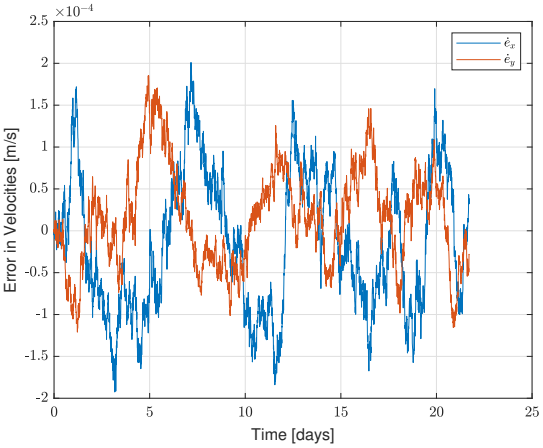

Figure 3.11: Estimation error in velocity.

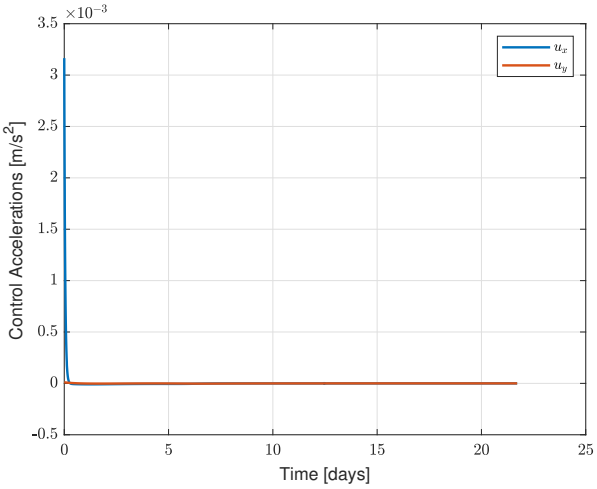

Figure 3.12: Control inputs evolution in time.

Lissajous Family

The Lissajous orbit defined in [11] is taken as nominal orbit. The main parameters of the orbit are shown in Tab.(3.6)

C	**Period**	$\boldsymbol{y_0}$	$\boldsymbol{\dot{x}_0}$	$\boldsymbol{A_y}$ [Km]	$\boldsymbol{A_z}$ [Km]
3.1995	2.6916	-0.009105	-0.005926	-3500	3500

Table 3.6: Orbit Parameter of the nominal Lissajous orbit.

As no indication on the control tuning is provided by [11], arbitrary values are chosen to regulate the LQG regulator. Their values are presented in Tab.(3.7)

Parameter	**Value**
Q	I_{6x6}
R	I_{3x3}
H	I_{6x6}
Integration Time	10.7663 [-] / 47 days

Table 3.7: LQG and simulation set up for the continuous optimal control on Lyssajous orbit.

No injection error is here considered in order to focus on the operational-life of the satellite and on the effect of the residual error coming from the linearization of the EoMs; differently from Halo and Lyapunov orbits, Lissajous orbit equations are derived from the linearized EoMs and no numerical correction scheme is applied. A residual approximation error is

thus presents and forces the active control to intervene to keep the spacecraft in the desired trajectory, even in the abscence of injection errors nor disturbances. Fig.(3.14) shows the nominal Lissajous orbit while from Fig.(3.16) to Fig.(3.18) the results concerning the LQG control are presented.

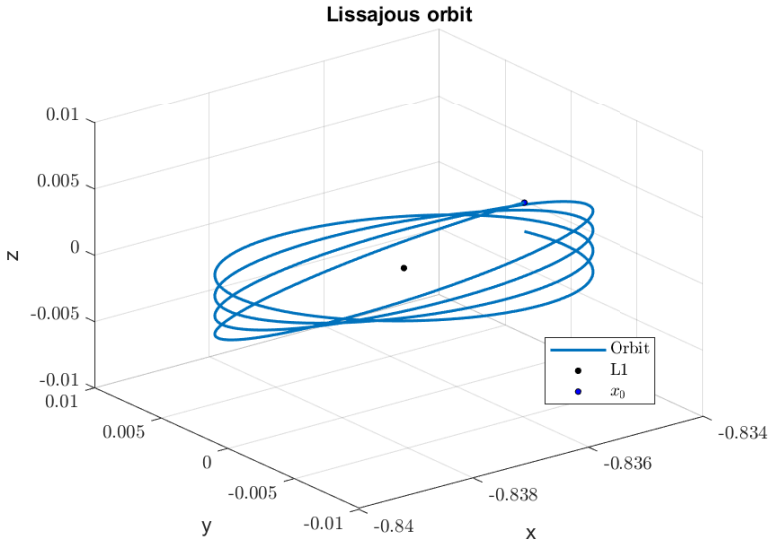

Figure 3.13: Reference Lissajous Orbit for the LQG

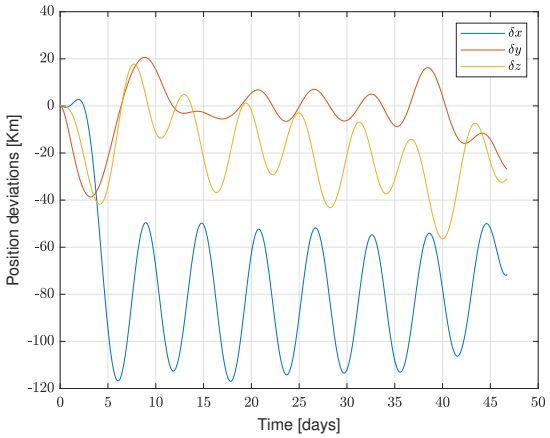

Figure 3.14: Position deviation evolution in time.

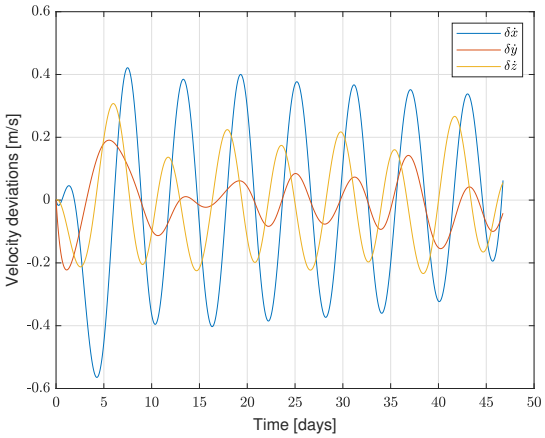

Figure 3.15: Velocity deviation evolution in time.

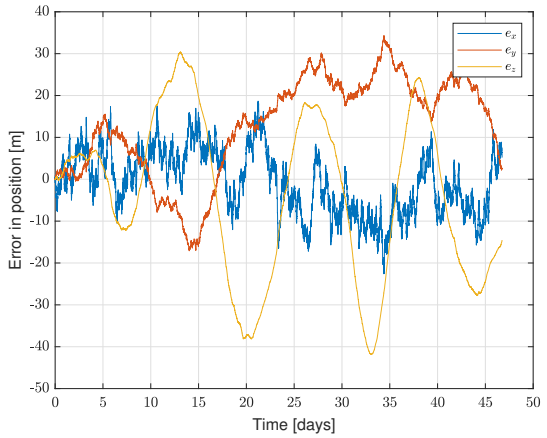

Figure 3.16: Estimation error in position.

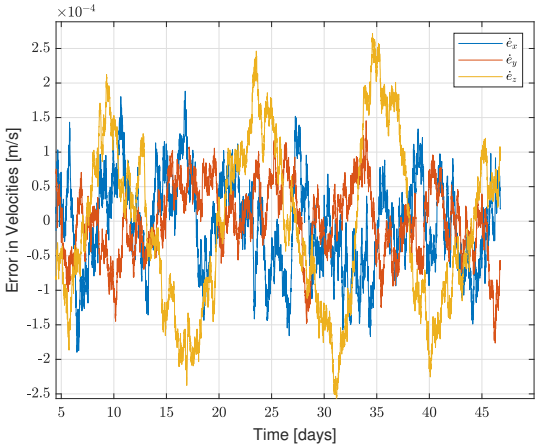

Figure 3.17: Estimation error in velocity.

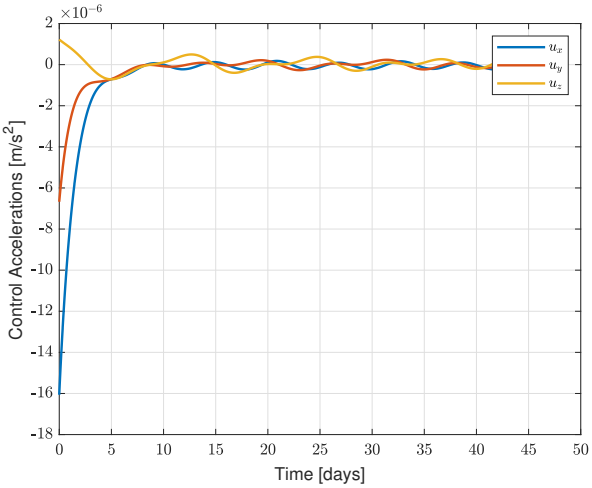

Figure 3.18: Control inputs evolution in time.

The total cost, for a simulation period of 47 days (which is four times the oscillation period in the x-y plane) is $\Delta V = 95 \left[\frac{m}{s}\right]$. The result obtained for the Lissajous trajectory is not comparable with the ones obtained for Halo and Lyapunov orbits. As mentioned before, the most relevant factor driving the behaviour of the control action is the truncation error affecting the nominal trajectory itself. Differently from Halo and Lyapunov families, here the control is not able to lead back the actual spacecraft trajectory on the nominal one. As highlighted in Fig.(3.14), the spacecraft is stabilized in a trajectory close to the nominal one but its position deviation never goes to zero. The imprecision of the nominal trajectory impacts significantly on the cost of the station-keeping; even if the simulation period is higher with respect to the one used for Halo and Lyapunov orbits the costs remains remarkably higher compared to the one required by the other orbits. The

comparison of the station-keeping costs emphasises the importance of the accuracy on nominal trajectory computation; for such highly non-linear system, numerical correction procedures are mandatory in order to filter out the truncation errors which represent the most significant disturbance acting on the spacecraft dynamics.

Nevertheless, the control algorithm is able both to keep the state estimation close to the real value both to ensure the spacecraft to remain close to the reference trajectory.

Chapter 4

Attitude Control

The attitude control represents one of the core-field during the satellite design. Generally, from the payload fairing to the *EOL (End Of Life)*, the attitude of the satellite has to respect precise constraints and the satellite itself has to be driven in the desired attitude complaining the accuracy tolerances coming from the requirements of other subsystems. The *ADCS (Attitude Determination and Control System)* is the satellite subsystem whose role is to determine and control the orientation of the spacecraft, enabling it to perform *slew manoeuvres* (rest-to-rest manoeuvres) or to track a specified desired attitude trajectory.

In the previous chapter the satellite is proven to be stabilized in its orbit around the Libration point via *Continuous Optimal Control*. If the first step of the study is the development of an efficient station-keeping procedure, an efficient attitude tracking control algorithm is the second. It is necessary to develop a relative easy and robust control algorithm to guide the attitude of the spacecraft to track a specified orientation depending on the mission requirements. Although for an under-actuated satellite station-keeping and attitude tracking are coupled, this chapter is devoted to present the development of the attitude control alone in the context of the *High-Level Motion Control* framework, as it is done for the station-keeping case, in order to have an insight about its properties, advantages and disadvantages.

In the first part of this chapter the basis of Attitude Control is addressed; the Euler equations are derived, DCM and quaternion representations are explained to justify their

choice as attitude parameters in the control algorithm and the basis of non-linear control theory is presented. Then the second part is devoted more specifically to the control algorithm chosen for the attitude tracking task.

4.1 Fundamentals of Attitude Control

4.1.1 Kinematics and Dynamics of a Rigid Body

Euler's rotational equations of motion

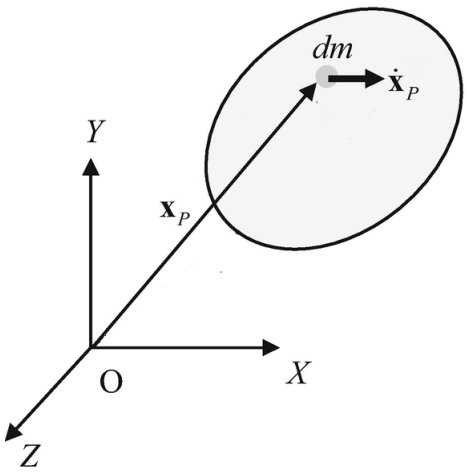

Figure 4.1: Rigid body representation.

Before introducing the kinematic relations and the EoMs governing the rotation of a rigid body, four concepts have to be defined:

1. *Centre of Mass (CoM)*: the position of the centre of mass for a rigid body $\boldsymbol{x_g}$ is defined as:

$$\boldsymbol{x_g} = \frac{\int_V \rho \boldsymbol{x_p} d\tau}{M_{tot}} \tag{4.1}$$

where V is the volume of the rigid body, ρ is the density of the infinitesimal volume $d\tau$, $\boldsymbol{x_p}$ is the position of a generic point P belonging to the body and M_{tot} is the total mass of the rigid body. If $\rho = cst.$ the CoM coincides with the baricentre of the body.

2. *Momentum*: the momentum of a rigid body $\boldsymbol{Q}$ is defined as:

$$\boldsymbol{Q} = \int_V \rho \boldsymbol{v_p} d\tau = M_{tot} \boldsymbol{v_g} \tag{4.2}$$

where $\boldsymbol{v_p}$ is the velocity of a generic point P belonging to the rigid body and $\boldsymbol{v_g}$ is the CoM velocity.

3. *Inertia Matrix*: the inertia matrix $\boldsymbol{I}_O$ with respect to a reference frame *O(X,Y,Z)* of a rigid body is defined as:

$$\boldsymbol{I}_O = \begin{bmatrix} I_{xx} & I_{xy} & I_{xz} \\ I_{yx} & I_{yy} & I_{yz} \\ I_{zx} & I_{zy} & I_{zz} \end{bmatrix} \quad I_{ii} = \int_v \rho (x_j + x_k)^2 d\tau \quad I_{ij} = -\int_v \rho x_i x_j d\tau \tag{4.3}$$

where $x_{i,j,k}$ are the components of $\boldsymbol{x_p}$ and i, j, k are natural indices ranging from 1 to 3. I_{ii} are called *Inertia Moments* while I_{ij} are called *Inertia Products*.

Considering a rotation of the reference O(X,Y,Z) frame through a rotation matrix $\boldsymbol{R}$ to a new reference frame O(X',Y',Z'), the inertia matrix is transformed according to Eq.(4.4).

$$\boldsymbol{I}'_O = \boldsymbol{R}' \boldsymbol{I}_O \boldsymbol{R} \tag{4.4}$$

Moreover it is always possible to find an orthonormal base (i.e. a reference frame) such that:

$$\boldsymbol{I}'_O = \begin{bmatrix} I_x & 0 & 0 \\ 0 & I_y & 0 \\ 0 & 0 & I_z \end{bmatrix} \tag{4.5}$$

In this case the axis of the reference frame are called *Principal Inertia Axes* and I_x, I_y and I_z are the *Principal Inertia Moments*.

4. *Angular Momentum*: the angular momentum $\mathbf{\Gamma}_O$ of a rigid body with respect to a reference frame O(X,Y,Z) is defined as:

$$\mathbf{\Gamma}_O = \boldsymbol{x_g} \times \boldsymbol{Q} + \boldsymbol{I}_g \boldsymbol{\omega} \tag{4.6}$$

where $\boldsymbol{\omega}$ is the angular velocity of a reference frame jointed to the body and centered to the body CoM.

Based on the above presented concepts the *Second Law of Dynamics*, describing the behaviour of a rotating body, might be introduced:

$$\frac{d\mathbf{\Gamma_O}}{dt} = \boldsymbol{Q} \times \dot{\boldsymbol{X}}_O + \boldsymbol{M}_O^e \tag{4.7}$$

where $\dot{\boldsymbol{X}}_O$ is the velocity of the observation point expressed in inertial coordinates and $\boldsymbol{M}_O^e$ represents the resultant external moments acting on the rigid body with respect to the observation point O.

In the case the observation point O is chosen to coincide with the CoM of the rigid body and the reference frame centered in O is aligned with the *Principal Inertia Axes*, Eq.(4.7) simplifies (Eq.(4.8)) and takes the form of the well-known *Euler Equations*, Eq.(4.9):

$$\frac{d\mathbf{\Gamma_g}}{dt} = \boldsymbol{M}_g^e \tag{4.8a}$$

$$\frac{d\mathbf{\Gamma_g}}{dt} = \frac{d}{dt}(\boldsymbol{I}_g \boldsymbol{w}) \tag{4.8b}$$

$$\frac{d\mathbf{\Gamma_g}}{dt} = I_x \dot{w}_x \hat{i} + I_y \dot{w}_y \hat{j} + I_z \dot{w}_z \hat{k} + \boldsymbol{w} \times \mathbf{\Gamma}_g \tag{4.8c}$$

$$\begin{cases} I_x \dot{w}_x + (I_z - I_y) w_z w_y = M_x & \text{(4.9a)} \\ I_y \dot{w}_y + (I_x - I_z) w_z w_x = M_y & \text{(4.9b)} \\ I_z \dot{w}_z + (I_y - I_x) w_x w_y = M_z & \text{(4.9c)} \end{cases}$$

In Eq.(4.8), $\hat{i}$, $\hat{j}$, $\hat{k}$ represent the principal inertia axes versors. In vector notation Eq.(4.9)

reads:

$$\boldsymbol{J}\dot{\boldsymbol{w}} = -\boldsymbol{w} \times \boldsymbol{J}\boldsymbol{w} + \boldsymbol{M} \tag{4.10}$$

Attitude parameters and kinematics

The Euler Equations are non-linear equations ruling the evolution of the angular velocity of the body in time subjected to external torques. It is miss to link the angular velocity to the attitude of the rigid body; there are a number of ways to accomplish this task. There representations include *Direct Cosine Matrices (DCM)*, *Euler Angles*, *Quaternions* and *Gibbs vector* and *Modified Rodriguez Parameters (MRP)*. Among all those possibilities, *DCM* and *Quaternions* are here presented as they are the representations adopted in this study.

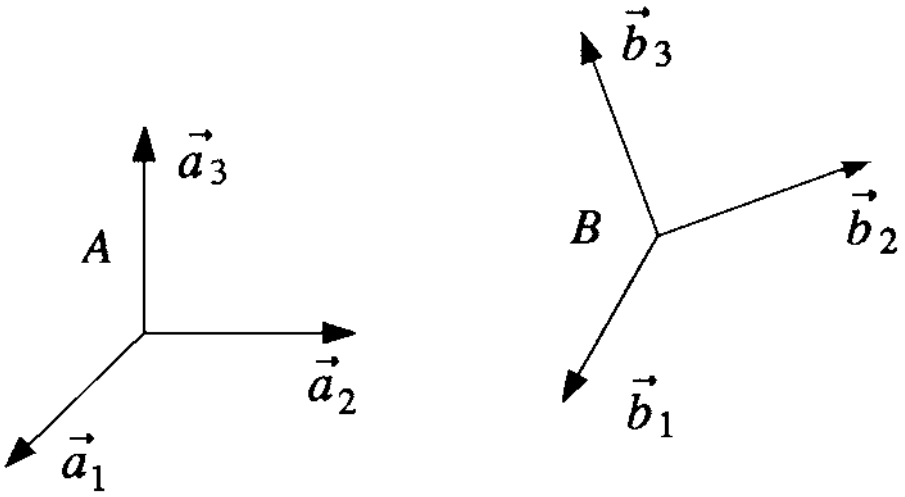

Figure 4.2: Two reference frame A and B.

Consider a reference frame A with a right-hand set of three orthogonal unit vectors $\{\hat{a_1}, \hat{a_2}, \hat{a_3}\}$ and a reference frame B with another right-hand set of three orthogonal unit vectors $\{\hat{b_1}, \hat{b_2}, \hat{b_3}\}$, as shown in Fig.(4.2). Basis vectors $\{\hat{b_1}, \hat{b_2}, \hat{b_3}\}$ of B are expressed in terms of basis vectors $\{\hat{a_1}, \hat{a_2}, \hat{a_3}\}$ of A as follows [4]:

$$\begin{bmatrix} \hat{b}_1 \\ \hat{b}_2 \\ \hat{b}_3 \end{bmatrix} = \begin{bmatrix} C_{11} & C_{12} & C_{13} \\ C_{21} & C_{22} & C_{23} \\ C_{31} & C_{32} & C_{33} \end{bmatrix} \begin{bmatrix} \hat{a}_1 \\ \hat{a}_2 \\ \hat{a}_3 \end{bmatrix} = \boldsymbol{A} \begin{bmatrix} \hat{a}_1 \\ \hat{a}_2 \\ \hat{a}_3 \end{bmatrix} \tag{4.11}$$

where $C_{ij} = \hat{b}_i \cdot \hat{a}_j$ is called *direction cosine* and $\boldsymbol{A}$ is called *Direction Cosine Matrix*. The matrix $\boldsymbol{A}$ is a rotation matrix and it implies that $\boldsymbol{A}\boldsymbol{A}' = \boldsymbol{I}$ and $det(\boldsymbol{A}) = 1$. The DCM allows switching from the representation of a vector in one reference frame to another reference frame. Considering a generic vector $\boldsymbol{x}_a$ expressed in the reference frame A, its formal expression in the reference frame B is given by Eq.(4.12a). Considering multiple rotations a new reference frame C is introduced and the expression which allow switching from A to C passing from B is given in Eq.(4.12c).

$$\boldsymbol{x}_b = \boldsymbol{A}\boldsymbol{x}_a \tag{4.12a}$$

$$\boldsymbol{x}_c = \boldsymbol{A}^1\boldsymbol{x}_b \tag{4.12b}$$

$$\boldsymbol{x}_c = \boldsymbol{A}^1\boldsymbol{A}\boldsymbol{x}_a = \boldsymbol{A}^2\boldsymbol{x}_a \rightarrow \boldsymbol{A}^2 = \boldsymbol{A}^1\boldsymbol{A} \tag{4.12c}$$

Eq.(4.12c) is also referred as the *multiplication rule*. It allows always to pass from a fixed inertial reference frame to the body fixed one. Given the desired attitude $\boldsymbol{A}_d$ it is thus possible to define the *Attitude Error matrix* $\boldsymbol{A}_e$ which represent the attitude error between the actual attitude $\boldsymbol{A}$ and the desired one expressed by $\boldsymbol{A}_d$.

$$\boldsymbol{A}_e = \boldsymbol{A}\boldsymbol{A}_d' \tag{4.13}$$

The attitude evolution in time might be obtained by differentiating the DCM definition (Eq.(4.11)) in time. It yields to the relation between angular velocity and attitude changes. Starting from Eq.(4.11) it is defined $\boldsymbol{B} = \begin{bmatrix} \hat{b}_1 & \hat{b}_2 & \hat{b}_3 \end{bmatrix}'$ and $\boldsymbol{N} = \begin{bmatrix} \hat{a}_1 & \hat{a}_2 & \hat{a}_3 \end{bmatrix}'$ where it is assumed that the reference frame A is inertial and it is referred to as $\boldsymbol{N}$. Eq.(4.14) and Eq.(4.15) show the rest of the procedure.

$$\begin{aligned} \boldsymbol{B} = \boldsymbol{A}\boldsymbol{N} \rightarrow \boldsymbol{A}'\boldsymbol{B} = \boldsymbol{N} \\ \frac{d}{dt}(\boldsymbol{A}'\boldsymbol{B}) = \frac{d}{dt}\boldsymbol{N} \rightarrow \dot{\boldsymbol{A}}' = -\boldsymbol{A}'\dot{\boldsymbol{B}}\boldsymbol{B}' \end{aligned} \tag{4.14}$$

$$\dot{\boldsymbol{B}} = \begin{bmatrix} \dot{\hat{b}}_1 \\ \dot{\hat{b}}_2 \\ \dot{\hat{b}}_3 \end{bmatrix} \qquad \dot{\hat{b}}_i = \boldsymbol{w} \times \hat{b}_i \qquad \dot{\boldsymbol{B}} = -\tilde{\boldsymbol{W}}\boldsymbol{B} \qquad \tilde{\boldsymbol{W}} = \begin{bmatrix} 0 & -w_2 & w_2 \\ w_3 & 0 & w_1 \\ -w_2 & w_1 & 0 \end{bmatrix} \tag{4.15}$$

$$\dot{\boldsymbol{A}} = -\tilde{\boldsymbol{W}}\boldsymbol{A} \tag{4.16}$$

In Eq.(4.15), $\tilde{\boldsymbol{W}}$ is called the *Skew-Symmetric* or *Hat-map* Matrix of the vector $\boldsymbol{w}$. Eq.(4.16) might be integrated in time with the standard integrator. However, due to numerical errors, the matrix $\boldsymbol{A}$ after some steps loses its orthogonality. In order to avoid using or developing complex structure-preserving numerical integration schemes, *quaternion* representation is preferred because of its intrinsically properties and robustness to integration.

Quaternions were developed by William Rowan Hamilton in 1843 as extension to complex numbers. A quaternion $\hat{\boldsymbol{q}}$ is defined as:

$$\hat{\boldsymbol{q}} = q_1 i + q_2 j + q_3 k + q_4 \tag{4.17}$$

where i, j, k are imaginary numbers such that:

$$\begin{aligned} i^2 = j^2 = k^2 = -1 \\ jk = -kj = i \\ ki = -ik = j \\ ij = -ji = k \end{aligned} \tag{4.18}$$

Quaternions are usually represented by composition of a scalar part q_4 and a vector part $\boldsymbol{q}$ such that $\hat{\boldsymbol{q}} = [\boldsymbol{q}\ q_4]$. Quaternions representing rotations are subjected to the normalization constraint such that:

$$q_1^2 + q_2^2 + q_3^2 + q_4^2 = 1 \tag{4.19}$$

Quaternions are used to parametrise rotations but they have no physical meaning so

they are not intuitive. Quaternions express rotations using 4 parameters, differently from DCM representation which relies on 9 parameters. As the number of parameters is not a *minimal set*, quaternions are not affected by singularities in the representation (which happens if Euler angles, MRP or Gibbs vector ase used) and they remains easy to handle and manipulate. They can be related to other rotation parametrisations by mean of specific relations; in the case of DCM the relation reads:

$$\boldsymbol{A} = (q_4^2 - \boldsymbol{q}'\boldsymbol{q})\boldsymbol{I} + 2\boldsymbol{q}\boldsymbol{q}' - 2q_4\tilde{\boldsymbol{Q}} \tag{4.20}$$

and the inverse representation is represented by Eq.(4.21). It must be noticed that quaternions have no singular condition even in the inverse transformation. In fact, should q_4 become zero it is always possible to evaluate one of the other components of the the quaternion which is surely different from zero but to Eq.(4.19) and then evaluate the remaining three components. The set of alternative inverse transformations can be easily found in [47].

$$\begin{cases} q_1 = \frac{1}{4q_4}(A_{23} - A_{32}) \\ q_2 = \frac{1}{4q_4}(A_{31} - A_{13}) \\ q_3 = \frac{1}{4q_4}(A_{12} - A_{21}) \\ q_4 = \pm\sqrt{1 + A_{11} + A_{22} + A_{33}} \end{cases} \tag{4.21}$$

Consecutive rotations are expressed through quaternion multiplication; considering two consecutive rotations expressed by the quaternions $\hat{\boldsymbol{p}}$ and $\hat{\boldsymbol{r}}$ the overall rotation $\hat{\boldsymbol{q}}$ is given in Eq.(4.22)

$$\hat{\boldsymbol{q}} = \hat{\boldsymbol{p}}\hat{\boldsymbol{r}} = p_4 r_4 + p_4\boldsymbol{r} + r_4\boldsymbol{p} + \tilde{\boldsymbol{P}}\boldsymbol{r} \tag{4.22}$$

The attitude error is expressed as the *quaternion error* $\hat{\boldsymbol{q}}_e$ defined as Eq.(4.23), where $\hat{\boldsymbol{q}}$ represents the actual attitude and $\hat{\boldsymbol{q}}_d$ is the desired attitude.

$$\hat{\boldsymbol{q}}_e = \begin{bmatrix} q_{4d} & q_{3d} & -q_{2d} & -q_{1d} \\ -q_{3d} & q_{4d} & q_{1d} & -q_{2d} \\ q_{2d} & -q_{1d} & q_{4d} & -q_{3d} \\ q_{1d} & q_{2d} & q_{3d} & q_{4d} \end{bmatrix} \hat{\boldsymbol{q}} \tag{4.23}$$

Eq.(4.23) is nothing more than the matrix representation of the quaternion multiplication rule applied to the attitude error case.

The quaternion kinematics, which links the angular velocity of the rigid body to the quaternion evolution in time, is obtained by substituting Eq.(4.20) into Eq.(4.16) and reads explicitly:

$$\begin{bmatrix} \dot{q}_1 \\ \dot{q}_2 \\ \dot{q}_3 \\ \dot{q}_4 \end{bmatrix} = \frac{1}{2} \begin{bmatrix} 0 & w_3 & -w_2 & w_1 \\ -w_3 & 0 & w_1 & w_2 \\ w_2 & -w_1 & -0 & w_3 \\ -w_1 & -w_2 & -w_3 & 0 \end{bmatrix} \begin{bmatrix} q_1 \\ q_2 \\ q_3 \\ q_4 \end{bmatrix} \tag{4.24}$$

or equivalently:

$$\begin{cases} \dot{\boldsymbol{q}} = -\frac{1}{2}\tilde{\boldsymbol{W}}\boldsymbol{q} + \frac{1}{2}q_4\boldsymbol{w} \\ \dot{q}_4 = -\frac{1}{2}\boldsymbol{w}'\boldsymbol{q} \end{cases} \tag{4.25}$$

The inverse relation is given in Eq.(4.26).

$$\begin{aligned} w_1 &= 2(\dot{q}_1 q_4 + \dot{q}_2 q_3 - \dot{q}_3 q_2 - \dot{q}_4 q_1) \\ w_2 &= 2(\dot{q}_2 q_4 + \dot{q}_3 q_1 - \dot{q}_1 q_3 - \dot{q}_4 q_2) \\ w_3 &= 2(\dot{q}_3 q_4 + \dot{q}_1 q_2 - \dot{q}_2 q_1 - \dot{q}_4 q_3) \end{aligned} \tag{4.26}$$

4.1.2 Non-linear control theory

Non-linear control theory has its roots in the more general *theory of dynamical systems* where the Lyapunov's theorems are of primary importance. The concepts of *Equilibrium Points* of a non-linear system and of *Stability* of equilibrium points has to be properly

defined as they are fundamental to understand the Lyapunov's theorems which represent the milestones of control theory. In this section the above mentioned concepts and theorem are presented. The definitions and theorem formulations refer to [4].

Equilibrium Point

Consider a nonlinear dynamic system described by

$$\dot{\boldsymbol{x}} = \boldsymbol{f}(\boldsymbol{x}, t) \tag{4.27}$$

where $\boldsymbol{x} = (x_1 \dots x_n)$ is the state vector. An equilibrium point of this dynamic system is a point $\boldsymbol{x}*$ such that

$$\boldsymbol{f}(\boldsymbol{x}*, t) = 0 \qquad \forall t$$

Lyapunov Stability

Consider an autonomous (time is not an explicit variable) non-linear dynamic system

$$\dot{\boldsymbol{x}} = \boldsymbol{f}(\boldsymbol{x}) \qquad \boldsymbol{x}(0) = \boldsymbol{x}_0 \tag{4.28}$$

defined on an open set containing the origin and $\boldsymbol{f}$ is continuous on this open set. Then an equilibrium point $\boldsymbol{x}*$ is said to be:

1. *Lyapunov stable* if for any $\epsilon > 0$ there exists a real positive number $\delta(\epsilon, t_0)$ such that

$$||\boldsymbol{x}(t_0) - \boldsymbol{x}*|| \leq \delta \Rightarrow ||\boldsymbol{x}(t) - \boldsymbol{x}*|| \leq \epsilon \qquad \forall t \geq t_0 \tag{4.29}$$

   where $||\boldsymbol{x}||$ denotes the Euclidean norm of a vector. Moreover if δ does not depend on t_0, then the equilibrium point is said to be *uniformly* Lyaounov stable.

2. *locally asymptotically stable* if it is Lyapunov stable and

$$||\boldsymbol{x}(t_0) - \boldsymbol{x}*|| \leq \delta \Rightarrow \boldsymbol{x}(t) \to \boldsymbol{x}* \qquad as\ t \to \infty \tag{4.30}$$

3. *globally asymptotically stable* if it is Lyapunov stable and $\boldsymbol{x}(t) \rightarrow \boldsymbol{x}*$ as $t \rightarrow \infty$ for any initial conditions $\boldsymbol{x}(t_0)$.

Lyapunov's First Stability Theorem

1. If the origin $\boldsymbol{x} = 0$ of a linearized system is asymptotically stable, then the equilibrium point $\boldsymbol{x}*$ of the original non-linear system, that has been linearized about, is also asymptotically stable.

2. If the origin $\boldsymbol{x} = 0$ of the linearized system is unstable, then the equilibrium point $\boldsymbol{x}*$ of the original non-linear system, that has been linearized about, is also unstable.

   It is important to note, however, that the Lyapunov stability of the equilibrium point at the origin $\boldsymbol{x} = 0$ of the linearized system does not implies the Lyapunov stability of the equilibrium point $\boldsymbol{x}*$ of the non-linear system.

The fist Lyapunov's theorem is extremely important as it defines which pieces of information might be extrapolated from a linearization procedure about the original non-linear system.

Lyapunov's second stability theorem

Consider an autonomous non-linear system described by Eq.(4.28) where $\boldsymbol{x}*$ is an equilibrium point. If there exists in some finite neighborhood Γ of the equilibrium point $\boldsymbol{x}*$ a positive-definite scala function $V(\boldsymbol{x})$ with continuous first partial derivatives with respect to $\boldsymbol{x}$ and t such that the following conditions exist:

1. $V(\boldsymbol{x}) \geq 0$ for all $\boldsymbol{x} \neq \boldsymbol{x}*$ in Γ, $V(\boldsymbol{x}*) = 0$ for all t.

2. $\dot{E}(\boldsymbol{x}) \leq 0$ for all $\boldsymbol{x} \neq \boldsymbol{x}*$ in Γ and for all t

then the equilibrium point $\boldsymbol{x}*$ is Lyapunov stable. If in addition

1. $\dot{E}(\boldsymbol{x})$ is not identically zero along any solution $\boldsymbol{x}$ of Eq.(4.28) other than $\boldsymbol{x}*$ then the equilibrium point $\boldsymbol{x}*$ is locally asymptotically stable.

If in addition

1. there exists in the entire state-space a positive-definite function $V(\boldsymbol{x})$ which is radially bounde, i.e. $V(\boldsymbol{x}) \to \infty$ as $||\boldsymbol{x}|| \to \infty$, then the equilibrium point $\boldsymbol{x}*$ is globally asymptotically stable, i.e. $\boldsymbol{x}(t) \to \boldsymbol{x}*$ as $t \to \infty$ for any initial conditions $\boldsymbol{x}(t_0)$.

Such a positive-definite function $V(\boldsymbol{x})$ is called *Lyapunov function*.
The theorem provides only sufficent conditions for checking the stability of an equilibrium point of a non-linear dynamic system and does not provide a method for determining a positive-definite Lyapunov function for a given non-linear system.

4.2 Attitude tracking control

Spacecraft manoeuvres characterised by a rest-to-rest motion are referred in literature as *slew manoeuvres* and in control theory they are treated as a *regulation problem*. Once the requirement is to track a time dependant attitude trajectory the problem is referred to as *tracking control problem*. Tracking control encompasses regulation as the latter represent a specific case on the former by setting the desired attitude to a constant and the desired angular velocity to zero.
In the wide range of possible method to apply, [29] quotes the *Variable-Structure Control*, also referred as *Sliding-Mode Control*, as an optimal compromise between robustness to uncertainties and disturbances and simplicity in design. According to [29], optimal control methods, which are based on solving two-point boundary value problems are excellent method for analysis purposes but they cannot be implemented in real spacecraft mission as they cannot be executed in real time. Feedback methods overcome this issue but their major drawbacks are that they are not general as they have to be properly specialised depending on the mission and are sensitive to noise effects, modeling errors or external disturbances.
As mentioned before, robust and relative easy controllers are found in the framework of the *sliding-mode techniques*. The reasons adduced by [29] has convinced the author to adopt a sliding-mode controller to face the tracking problem.

A brief overview of the sliding-mode control is here presented; later is presented the typology of sliding-mode control chosen to solve the tracking problem as well as the results coming from the simulation carried out to validate the procedure.

4.2.1 Sliding-Mode Control - Fundamentals

Sliding-mode control is based on the intuitively idea that it is much easier to design an efficient control for a 1^{st}-order system, be it nonlinear or uncertain than it is for a n^{th}-order system. Accordingly a particular transformation in model description is introduced which allows n^{th}-order problems to be replaced by equivalent 1^{st}-order problems [42]. The control law is then derived by the analysis conducted on the equivalent 1^{st}-order system and it is generally composed by a nominal part and an additional terms aimed at dealing with model uncertainty and undesired behaviours of the control input (such as *chattering phenomena*).

The concepts are presented for SISO systems which allows a direct and intuitive explanation of the main aspects of nonlinear control design.

So, consider the single-input dynamic system [42]

$$x^{(n)} = f(\boldsymbol{x}) + b(\boldsymbol{x})u \tag{4.31}$$

where the scalar x is the output of interest, the scalar u is the control input, $\boldsymbol{x}$ is the state vector. The function $f(\boldsymbol{x})$, in general non-linear, is not exactly known but the extent of the imprecision on $f(\boldsymbol{x})$ is upper bounded by a known continuous function of $\boldsymbol{x}$; similarly, the control gain $b(\boldsymbol{x})$ is not exactly known, but is of known sign and is bounded by known, continuous functions of $\boldsymbol{x}$. The control problem is to get the state $\boldsymbol{x}$ to track a specific time-varying state $\boldsymbol{x}_d$ in the presence of model imprecision on $f(\boldsymbol{x})$ and $b(\boldsymbol{x})$.

Let $\Delta x = x - x_d$ be the tracking error in the variable x, and let $\Delta\boldsymbol{x}$ the tracking error vector defined as:

$$\Delta\boldsymbol{x} = \boldsymbol{x} - \boldsymbol{x}_d = \begin{bmatrix} \Delta x & \Delta\dot{x} & \dots & \Delta x^{(n-1)} \end{bmatrix}' \tag{4.32}$$

It is then introduced a time-varying surface $S(t)$ in the state-space $R^{(n)}$ defined by the scalar equation $s(\boldsymbol{x}, t) = 0$ where

$$s(\boldsymbol{x}, t) = \big(\frac{d}{dt} + \lambda\big)^{n-1} \Delta x \tag{4.33}$$

and λ is a strictly positive constant. Being the initial conditions to Eq.(4.31) given as:

$$\boldsymbol{x}(0) = \boldsymbol{x}_d(0) \tag{4.34}$$

the equation $s(\Delta\boldsymbol{x}, t) = 0$ represents a linear differential equation whose unique solution is $\Delta\boldsymbol{x} = 0$. It means that the problem of tracking $\boldsymbol{x} = \boldsymbol{x}_d$ is equivalent to that of remaining on the surface $S(t)$ $\forall t > 0$. Effectively, the problem of tracking the n-dimensional vector $\boldsymbol{x}_d$ is replaced by a 1^{st}-order stabilization problem in s.

The simplified, 1^{st}-order problem of keeping the scalar s at zero can now be achieved by choosing the control law u of Eq.(4.31) such that outside of $S(t)$ [42]

$$\frac{1}{2}\frac{d}{dt}s^2 \leq -\eta|s| \tag{4.35}$$

where η is a strictly positive constant. Eq.(4.35) states that the squared distance to the surface, as measured by s^2, decreases along all system trajectories in the phase-space and usually it is referred as *sliding condition*. Moreover, satisfying Eq.(4.35) automatically implies that the closed-loop system is *globally asymptotically stable* from *Lyapunov's Second Stability Theorem*. In fact, considering as candidate Lyapunov function $V(s) = \frac{1}{2}s^2$ it is easy to check that if the sliding condition is satisfied, Lypunov's theorem conditions are too.

Once on the surface the system trajectories remain on the surface (the surface represents thus an *invariant set*) and the dynamic of the system when is in the so called *sliding mode* (i.e. when the state lies on the sliding surface s) can be written as:

$$\dot{s} = 0 \tag{4.36}$$

It is worth noticing from Eq.(4.35) that disturbances and uncertainties can be handled by the method while still keeping and invariant set as Lyapunov conditions ($\dot{V} < 0$) are still verified even if a perturbation is applied on s.

The last remark concerning the sliding condition is that, if Eq.(4.34) is not exactly verified, the surface $S(t)$ will nonetheless be reached in a finite time smaller than $\frac{|s(t=0)|}{\eta}$.

As shown by Fig.(4.3) the part of the state-trajectory outside the sliding surface is called *Reaching Phase* or *Mode* while when on the sliding surface it is named *Sliding Phase* or *Mode*.

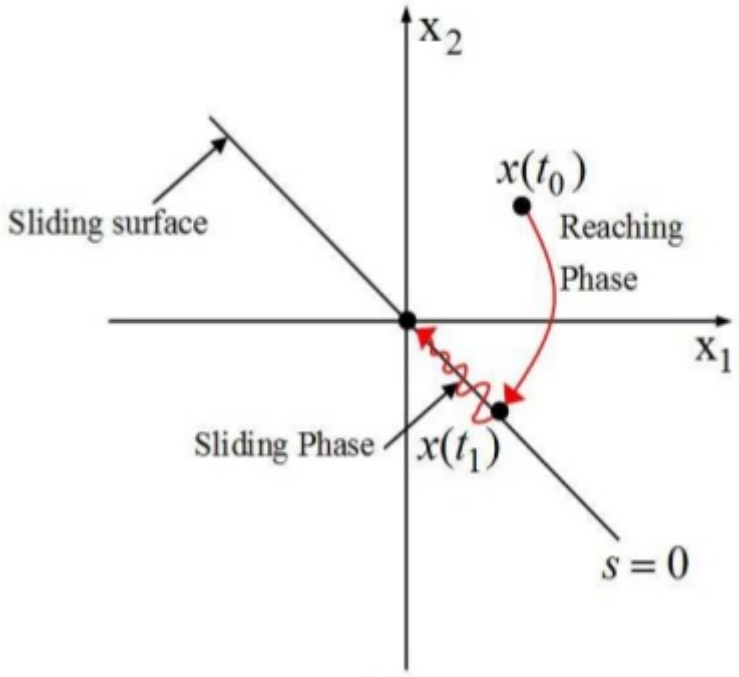

Figure 4.3: Graphical representation of Eq.(4.33) and Eq.(4.35) for $n = 2$

By solving Eq.(4.36) formally for the control input, it is obtained an expression for u called the equivalent control u_e which can be interpreted as the continuous control law that would maintain $\dot{s} = 0$ if the dynamics were exactly known [42]. It must be noticed that Eq.(4.36) cn be solved explicitly for u as it involves the first time-derivative of s which accounts for up to the *n-th - 1* derivative of x; in $\dot{s}$ thus appears $x^{(n)}$ and therefore u according to Eq.(4.31).

In order to satisfy sliding condition despite uncertainty on the dynamics f, or other external disturbances, a discontinuous term u_{dis} has to be added across the surface $s = 0$. The optimal performance is achieved by expressing $u_{dis} = k \cdot sign(s)$ for some scalar k but

at the price of a significant *chattering* behaviour of the control system. A good alternative function is the *saturation function* with a varying boundary layer thickness ϵ such that

$$u = u_e - k \cdot sat(s,\ \epsilon) \qquad sat(s,\ \epsilon) = \begin{cases} 1 & \text{for } s > \epsilon \\ \dfrac{s}{\epsilon} & \text{for } |s| \leq \epsilon \\ -1 & \text{for } s < -\epsilon \end{cases} \tag{4.37}$$

The tracking performance is sub-optimal compared to using the signum function but it provides a good trade-off between robustness and practical implementation for a smoothed control input. [29].

4.2.2 Sliding-Mode Control - NFTSM

The sliding-mode control implemented in this study refers to the family of the so called *Non-singular Fast Terminal Sliding Mode (NFTSM)* controllers. The fundamental idea that rules the controller design is the same as for the classical sliding-mode controllers (described in the previous section); the main difference rely on the choice of the sliding surface which, in the case of NFTSM, is not linear. The main attraction of such approach over the conventional sliding mode control (SMC) is the finite time convergence and the improved steady state accuracy. Nevertheless the choice of a non-linear sliding surface presents two shortcomings [45]:

1. presence of singularities in control
2. slow convergence speed for the remotely located system states

The NFTSM arises as an efficient solution to eliminate those drawbacks and represents a general and global method applicable to all possible circumstances.
The governing equations presented in Sec.(4.1.1) must be slightly manipulated in order to be implemented in the method. Actually the angular velocity error between reference frame and a desired reference frame is required to be established, as well as its dynamics. Starting from the definition of attitude error matrix in Eq.(4.13) the angular velocity error is determined according to Eq.(4.38).

$$\begin{aligned}
&\frac{d}{dt}\boldsymbol{A}_e = \frac{d}{dt}(\boldsymbol{A}\boldsymbol{A}_d') = \frac{d}{dt}\boldsymbol{A}\boldsymbol{A}_d' + \boldsymbol{A}\frac{d}{dt}(\boldsymbol{A}_d)' \\
&-\tilde{\boldsymbol{W}}_e\boldsymbol{A}_e = -\tilde{\boldsymbol{W}}\boldsymbol{A}\boldsymbol{A}_d' + \boldsymbol{A}(-\tilde{\boldsymbol{W}}_d\boldsymbol{A}_d)' = -\tilde{\boldsymbol{W}}\boldsymbol{A}_e + \boldsymbol{A}_e\tilde{\boldsymbol{W}}_d \\
&-\tilde{\boldsymbol{W}}_e = -\tilde{\boldsymbol{W}} + \boldsymbol{A}_e\tilde{\boldsymbol{W}}_d\boldsymbol{A}_e' = -\tilde{\boldsymbol{W}} + \boldsymbol{A}_e\tilde{\boldsymbol{w}}_d \\
&\boldsymbol{w}_e = \boldsymbol{w} - \boldsymbol{A}_e\boldsymbol{w}_d
\end{aligned} \tag{4.38}$$

Then substituting Eq.(4.38) and its derivative into Eq.(4.10) yields:

$$\boldsymbol{J}\dot{\boldsymbol{w}}_{\boldsymbol{e}} = -(\boldsymbol{w}_{\boldsymbol{e}} + \boldsymbol{A}_{\boldsymbol{e}}\boldsymbol{w}_{\boldsymbol{d}}) \times (\boldsymbol{w}_{\boldsymbol{e}} + \boldsymbol{A}_{\boldsymbol{e}}\boldsymbol{w}_{\boldsymbol{d}}) + \boldsymbol{J}(\boldsymbol{w}_e \times \boldsymbol{A}_e\boldsymbol{w}_d - \boldsymbol{A}_e\dot{\boldsymbol{w}}_d) + \boldsymbol{M} \tag{4.39}$$

Thus Eq.(4.23), Eq.(4.25) and Eq.(4.39) are the equations ruling the attitude error dynamics of the spacecraft and represent the cardinal equations of NFTSM.
For the control design purpose the following assumptions are made [45]:

1. In the spacecraft mission, the quaternion $\boldsymbol{q}$ and the body angular velocity vector $\boldsymbol{w}$ are measurable and available throughout the space mission for attitude control design.

2. The desired attitude frame angular velocity $\boldsymbol{w}_d$ and its first time derivative $\dot{\boldsymbol{w}}_d$ are bounded, and the bounds are known.

3. eventual uncertainties of modeling (inertia) or external disturbances are bounded and the bound limit is known in advance.

The *non-linear sliding surface* is designed according to Eq.(4.40) and the control law design refers to Eq.(4.41).

$$\boldsymbol{s} = sig^{\rho}(\boldsymbol{w}_e) + \boldsymbol{C}sig^{\rho}(\boldsymbol{q}_e) + \boldsymbol{D}\boldsymbol{q}_e \tag{4.40}$$

$$\boldsymbol{M}(t) = -\boldsymbol{K}_1\boldsymbol{s} - \boldsymbol{K}_2sig^{l}(\boldsymbol{s}) + \boldsymbol{T} \tag{4.41}$$

where

$$\boldsymbol{T} = (\boldsymbol{w_e} + \boldsymbol{A_e w_d}) \times (\boldsymbol{w_e} + \boldsymbol{A_e w_d}) - \boldsymbol{J}_0(\boldsymbol{w}_e \times \boldsymbol{A}_e \boldsymbol{w}_d - \boldsymbol{A}_e \dot{\boldsymbol{w}}_d)$$
$$-\frac{\boldsymbol{J}_0}{2\rho}(\rho \boldsymbol{C} diag(|\boldsymbol{q}_e|^{\rho-1}) + \boldsymbol{D})(q_{e4}\boldsymbol{I} + \tilde{\boldsymbol{Q}}_e) sig^{2-\rho}(\boldsymbol{w}_e)$$

and the other definitions are listed in Tab.(4.1).

$\boldsymbol{s}$	$[s_1\ s_2\ s_3]' \in R^3$
$\boldsymbol{C}$	$diag(c_1,\ c_2,\ c_3)$ with $c_i > 0\ \forall i$
$\boldsymbol{D}$	$diag(d_1,\ d_2,\ d_3)$ with $d_i > 0\ \forall i$
$\boldsymbol{K}_1$	$diag(k_{11},\ k_{12},\ k_{13})$ with $k_{1i} > 0\ \forall i$
$\boldsymbol{K}_2$	$diag(k_{21},\ k_{22},\ k_{23})$ with $k_{2i} > 0\ \forall i$
ρ	$\in (1, 2)$
l	$\in (0, 1)$
$sig^{\rho}(\xi)$	$[\lvert\xi_1\rvert sign(\xi_1), \lvert\xi_2\rvert sign(\xi_2), \lvert\xi_3\rvert sign(\xi_3)]'$

Table 4.1: Definitions of parameters appearing in Eq.(4.40) and Eq.(4.41)

In order to demonstrate the *finite time stable equilibrium* of Eq.(4.40) and Eq.(4.41) the following lemma, which can be interpreted as an extension to Lyapunov's second theorem, is here reported [45].

Lemma:[39] for a continuous system $\dot{x} = f(x)$, $f(0) = 0$ $x \in R^n$, suppose there exists a continuous positive definite function $V : R^n \to R$, a real number $a > 0$ and $\alpha \in (0, 1)$ and an open neighborhood $U_0 \subseteq R^n$ of the origin such that an extended Lyapunv description is defined by

$$\dot{V}(x) + aV(x) + bV^{\alpha}(x) \leq 0 \tag{4.42}$$

Then the origin is a finite time stable equilibrium. If $U_0 = R^n$, then the origin is a globally finite time stable equilibrium. Further, depending on the initial state $x(0) = x_0$, the origin can be achieved in finite time t_1 given by

$$t \leq \frac{1}{a(1-\alpha)} ln \frac{aV^{1-\alpha}(x_0) + b}{b} \tag{4.43}$$

The finite-time convergence proof is structured in two parts: firstly it is demonstrated the attitude states will converge to the equilibrium in finite time once the attitude trajectory falls on $\boldsymbol{s} = 0$; the candidate Lyapunov function is selected as $V_1 = \boldsymbol{q}_e \boldsymbol{q}_e'$. Then it is proved the finite time stability in reaching phase, where the candidate Lyapunov function reads $V_2 = \frac{1}{2}\boldsymbol{s}'\boldsymbol{J}\boldsymbol{s}$. The detail if the proof might be found in [45].

Results

The simulations are based on the results obtained from the *Station-keeping Continuous Optimal Control (LQG)* presented in Sec.(3.1). Both reference orbits and the control tuning reflect those used in Sec.(3.1) and the results are used to generate the baseline track for the attitute tracking problem.
Eq.(4.40) and Eq.(4.41) require the knowledge of the desired angular velocity $\boldsymbol{w}_d$ and acceleration $\dot{\boldsymbol{w}}_d$. It is thus necessary to define the *Spacecraft Desired Attitude* along the orbit. Two are the most natural choices: the first one requires the satellite to constantly point the lighter primary of the *R3BP* which means the Moon in the Earth-Moon system or the Earth in the Sun-Earth system. The second, conversely, envisages the satellite to point to the heavier one. Depending on mission objectives one solution may be more convenient than the other; for this project it is chosen to orient the satellite towards the lighter primary, which is also the closer body to L1 and L2. The desired attitude is thus computed by means of DCM whose components are determined by fixing the satellite body axes in the following way:

1. The x-axis of the desired body reference frame is aligned to the vector joining the spacecraft with the smaller body, in the direction of the smaller body.

2. The desired y-axis of the body frame belongs to the plane defined by the x-axis and the vector joining the spacecraft position to the libration point.

3. The desired z-axis of the body frame completes the right-handed triad.

The actual position of the spacecraft along its motion around the libration point is given by the combination of the nominal trajectory position and the position deviation arising

from LQG analysis. Once the DCM is determined along the orbit, it is applied Eq.(4.21) to pass from DCM to quaternion representation. Consequently Eq.(4.26) is used to extract the desired angular velocity along the orbit and, numerically differentiating the result, the desired angular acceleration. It must be noticed that, due to the fact that the reference frame is not inertial, the rotation velocity of the latter has to be taken into consideration once computing $\boldsymbol{w}_d$.

Numerical differentiation is accomplished using *central finite difference scheme* for the interior point of the set and *forward/backward finite difference scheme* for the boundary points.

What is left is to define the NFTSM control parameter values, which are listed in Tab.(4.2), and the disturbance torques acting on the spacecraft. Tab.(4.3) summarise the disturbances affecting attitude determination and control input execution, as it is done in Chapter 3 for the LQG algorithm. Each quaternion measure is perturbed by adding to the nominal value an *Additive Gaussian White Noise (AGWN)* having mean value $\mu_N = 0$ and variance $\sigma_{NN} = 1e-9$. Execution errors are simulated adding AGWN characterised by $\mu_D = 0$ and $\sigma_{DD} = 1e-8$ [gm], to each of the $\boldsymbol{M}$ components. The simulation starts with an initial error of the 5% with respect to desired attitude and angular velocity.

$\boldsymbol{J_0 = J}$	diag(22.7 23.3 24.5) [Kg·m^2]
ρ	1
l	0.99
$\boldsymbol{C}$	diag(0.42 0.42 0.42)
$\boldsymbol{D}$	diag(1.9 1.9 1.9)
$\boldsymbol{K}_1$	diag(7 7 7)
$\boldsymbol{K}_2$	diag(0.5 0.5 0.5)
$\hat{\boldsymbol{q}}_0$	$\hat{\boldsymbol{q}}_d$
$\boldsymbol{w}_0$	[0 0 0]'

Table 4.2: NFTSM control parameters used for the simulations.

Initial error	$\boldsymbol{\delta q_0} = 0.05 \cdot \boldsymbol{q_0^d}$ $\boldsymbol{\delta w_0} = 0.05 \cdot \boldsymbol{w_0^d}$
Affected quantities	**AWGN parameters**
δq_1 δq_2	$\mu_{NN} = 0$
δq_3 δq_4	$\sigma_{NN} = 1e^{-9}$
δM_1	$\mu_{DD} = 0$
δM_2 δM_3	$\sigma_{DD} = 1e^{-8}$ [gm]

Table 4.3: Attitude tracking perturbation definition. All the disturbances are simulated as Additive White Gaussian Noise with mean values and variances defined in the table.

- **Halo orbit**: from Fig.(4.4) to Fig.(4.7) the attitude evolution as well as the control effort required by the attitude control system is presented.

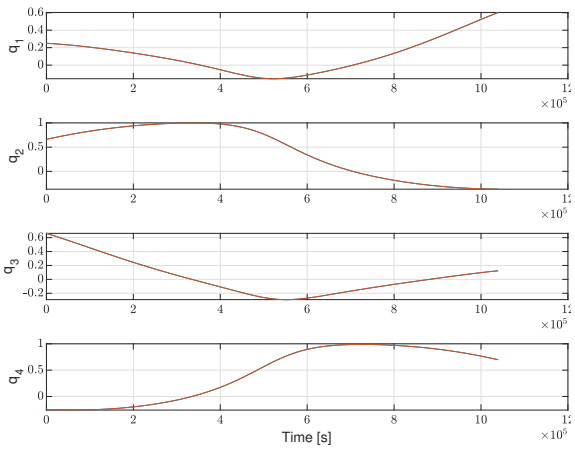

Figure 4.4: Actual and Desired quaternion evolution along orbit.

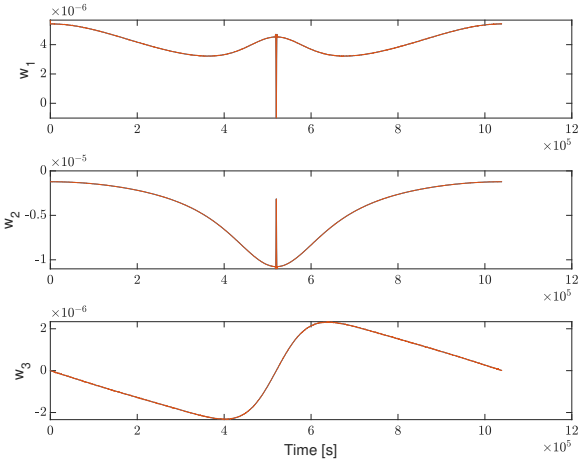

Figure 4.5: Actual and desired angular velocity evolution along the orbit.

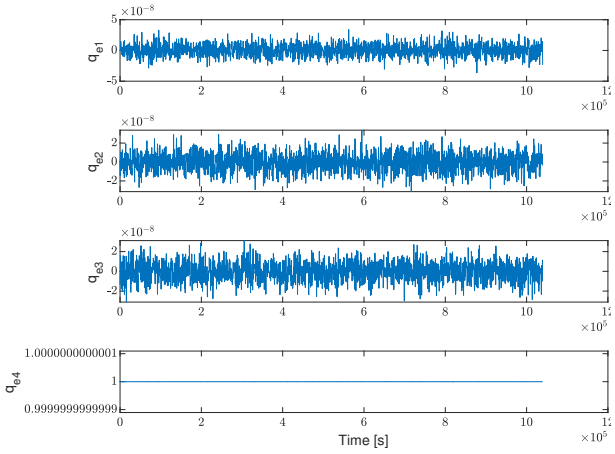

Figure 4.6: Quaternion error evolution along the orbit.

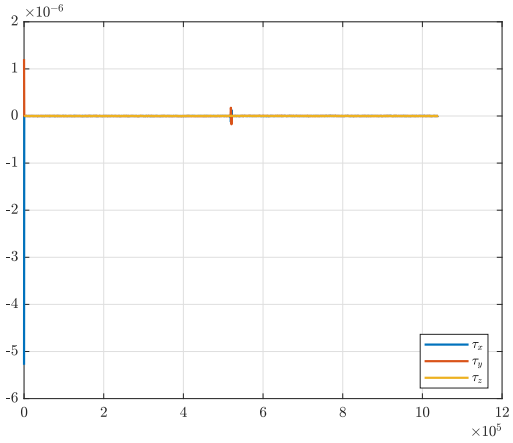

Figure 4.7: Control torques $\boldsymbol{M} = [\tau_x\ \tau_y\ \tau_z]'$ evolution along the orbit.

As it is shown by Fig.(4.4) and Fig.(4.5), the attitude tracking is accomplished perfectly by the NFTSM controller. Excect for the beginning, when the angular velocity has to link up with the initial desired value, the quaternion error is kept close to zero with a very modest control effort.

- **Lyapunov orbit**: the results concerning the attitude tracking control for a Lyapunov orbit are shown from Fig.(4.8) to Fig.(4.11).

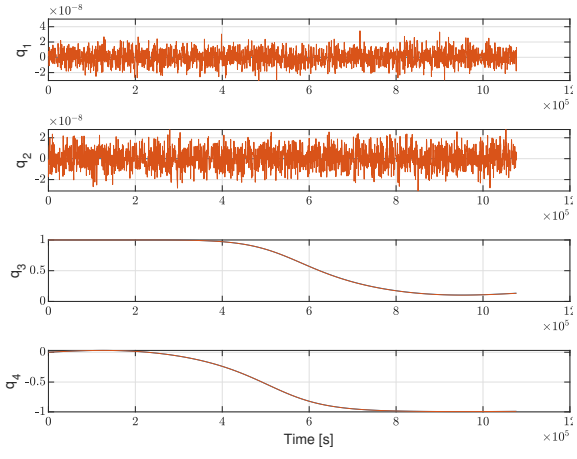

Figure 4.8: Actual and Desired quaternion evolution along orbit.

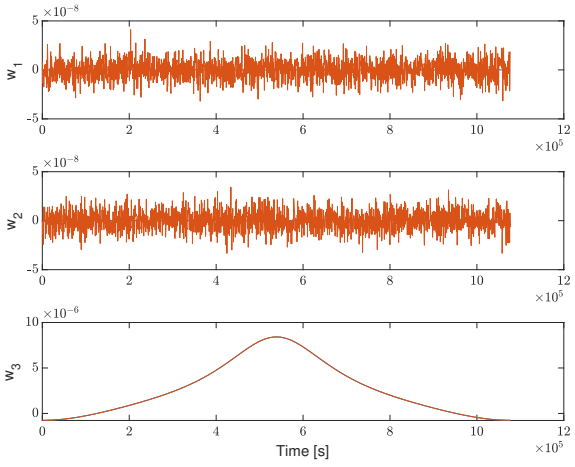

Figure 4.9: Actual and desired angular velocity evolution along the orbit.

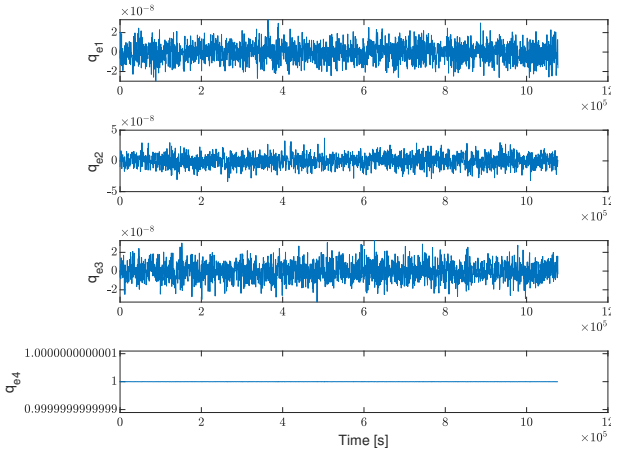

Figure 4.10: Quaternion error evolution along the orbit.

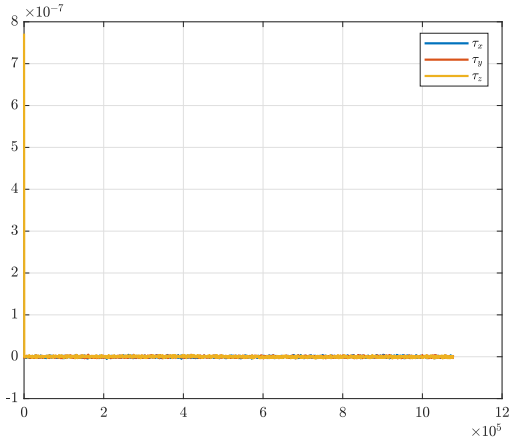

Figure 4.11: Control torques $\boldsymbol{M} = [\tau_x\ \tau_y\ \tau_z]'$ evolution along the orbit.

The characteristic of being planar is reflected both in the evolution of angular velocity and quaternion. The first two components of $\tilde{\boldsymbol{q}}$ and $\boldsymbol{w}$ are not influenced at all by the dynamics and keep their values constant to zero. Being a planar orbit in fact it is just w_3 that is requested to vary in order to track the desired attitude. Also in this case, with a slightly more significan control effort at the beginning, the NFTSM controller is able to keep the spacecraft attitude close to the reference trajectory.

- **Lissajous orbit**: for the Lissajous case the results are shown from Fig.(4.12) to Fig.(4.15).

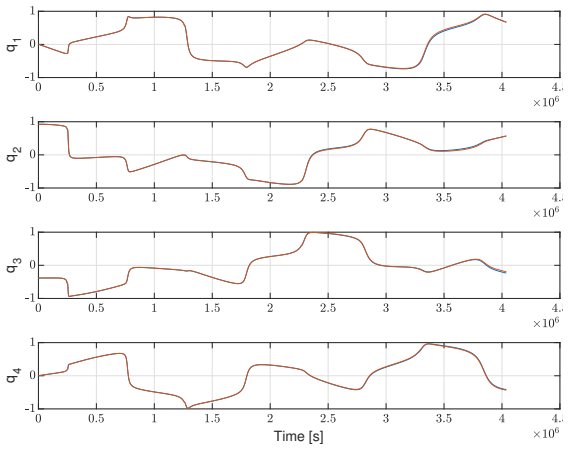

Figure 4.12: Actual and Desired quaternion evolution along orbit.

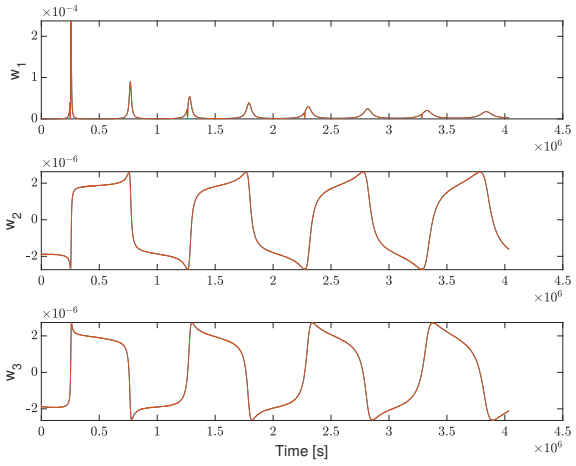

Figure 4.13: Actual and desired angular velocity evolution along the orbit.

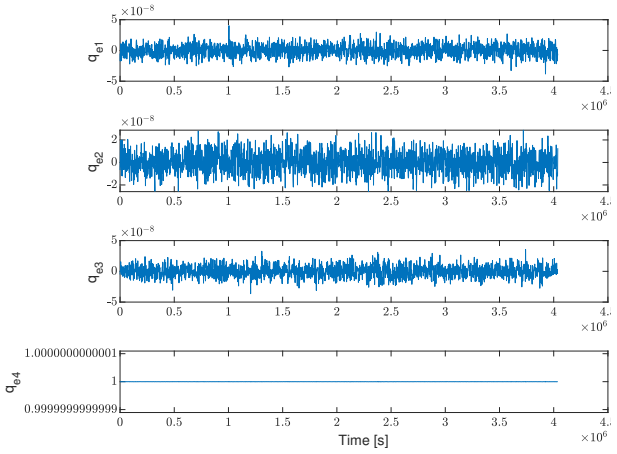

Figure 4.14: Quaternion error evolution along the orbit.

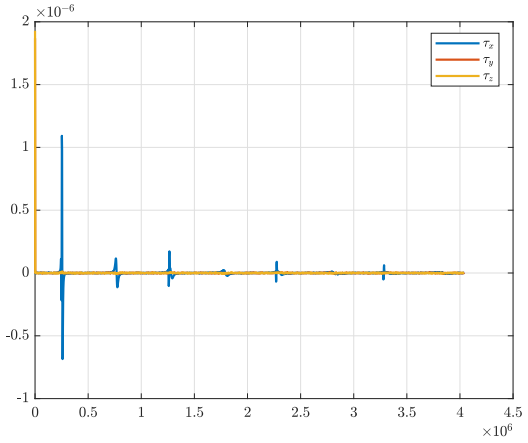

Figure 4.15: Control torques $\boldsymbol{M} = [\tau_x\ \tau_y\ \tau_z]'$ evolution along the orbit.

Differently from the Halo case and Lyapunov case, the Lissajous trend of angular velocity and quaternion is slightly more oscillatory. This evidence might be explicated considering the results obtained in Sec.(3.1). Because Lissajous orbit are analytical and are characterized by a truncation error, the position deviation and the control inputs oscillates in order to stabilise the spacecraft in a trajectory close to the nominal, never reaching it; this peculiarity is reflected also in the trace left by the desired (and consequently actual) angular velocity/quaternion trajectory. Nevertheless the NFTSM controller is able to keep the spacecraft orientation on the desired path with modest control effort.

As depicted by the results above reported, the NFTSM control is extremely efficient ,both in terms of convergence time both in terms of control effort, on commanding the spacecraft attitude to follow a particular desired trajectory. The method is general and applicable to whatever circumstance the mission implies; it has not been introduced any uncertainty upon the inertia matrix but, thank to the proofs developed in [45], it is proven that bounded uncertainties might be tolerated by the method. Moreover, the choice on the definition of the desired attitude trajectory is completely subjective and may vary depending on the mission; also in this case the method is proven to run whatever attitude trace is selected.

Chapter 5

Control Allocation

With Chapter 3 and Chapeter 4, High Level Motion Control is succesfully completed; the spacecraft is able to stay close to the reference orbit and maintain orientation despite external disturbances and tracking and execution errors. The overall mission control objectives are matched. What is missing now is to map the desired control forces and moments onto actuator actions. This procedure is called *Control Allocation* and its objective is to coordinate the different *effectors* (devices incharged of producing control inputs) such that they together produce the desired virtual control efforts, if possible; otherwise, the objective is shifted to minimise the error between the actual produced control inputs and the ideal ones.

The main goal of the work is to demonstrate the feasibility of station-keeping and attitude control using the minimum number of actuators possible. Station-keeping requires forces to act on the spacecraft which can be generated, in deep-space, only by thrusters. It is thus chosen to avoid the adoption of classical *Reaction Wheels (RW)* or *Control Moment Gyroscopes (CMG)* assemblies and rely only on four electrical gimbaled thrusters. The field has been reduced to electric propulsion because it is the only technology available capable of continuous, fine low thrust activity, indispensable features for the purposes of the project. Even if recent developments in micro-chemical propulsion systems allow precise responses to commanded inputs, the low efficiency in terms of energy conversion (expressed by the *Specific Impulse* I_{sp}) would require an enormous amount of propellant to grant the control objectives throughout the duration of the mission. Electric propulsion

can in fact boast specific impulses up to 100 times higher than chemical propulsion.
It is at this level that the coupling between station-keeping and attitude control arises. It is thus of paramount importance to understand how the coupling effect influences the behavior of the control system. The thruster configuration and the allocation procedure must be capable of handling technological gimbal limitations. Ideally, a 2-DOFs gimbal could orient the engine thrust all over the semi-sphere centered on the engine location and opposite to the satellite body, but practical technological issues prevent the achievement of such performance. Gimbals have a limited opening angle which narrow the field of possible thrust directions. For this reasons, two scenarios are simulated for each kind of orbit:

1. Unconstrained gimbals.

2. Constrained gimbals.

The term "*unconstrained*" means that the gimbal has no restriction as regards its opening angles; oppositely, "*constrained*" stands for limited allowed directions achievable by gimbal mechanisms.

5.1 Spacecraft thruster configuration

The first design choice to face is the location of the thrusters on the spacecraft. The system must be able to provide input forces and torques along each direction of the the body reference frame without any a priori preference. Among the infinite number of possibility, the configuration shown in Fig.(5.1) appears to be the more versatile and robust to any typology of mission.

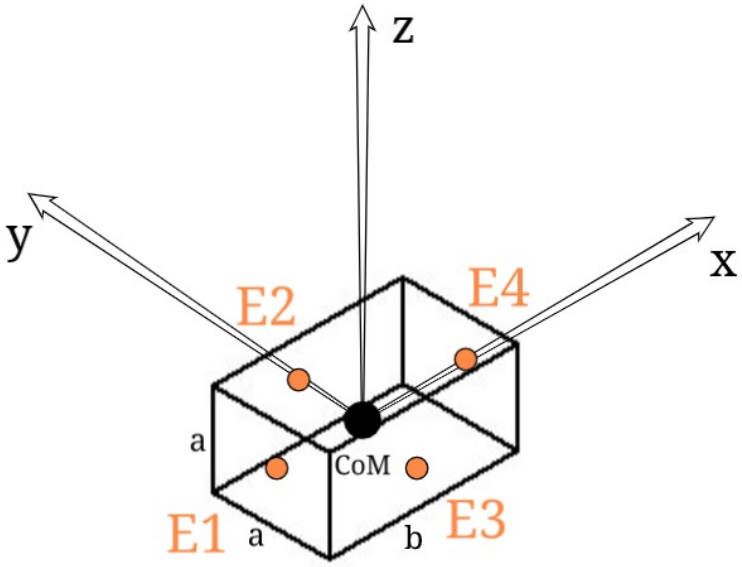

Figure 5.1: Actuator configuration. The reference frame *O(X,Y,Z)* is assumed to be centerd on the centre of mass of the satellite. The axes are assumed to be coincident with the principal inertia axes of the spacecraft. Engines E1 and E4 lie on the x-axis while E2 and E3 lie on the y-axis.

Engine 1 (E1) and Engine 4 (E4) are located along the x-axis of the body reference frame. Engine 2 (E2) and Engine 3 (E3) are located along the y-axis. The body reference frame *O(X,Y,Z)* represented in Fig.(5.1) is supposed to be aligned with the principal inertial axes of the satellite and centered on its Centre of Mass (CoM). Each of the engines is equipped with a 2-Degrees Of Freedom (DOFs) gimbal which allows thrust vector control on each thruster. The CubeSat designed for the LUMIO mission [6] is taken as baseline case; the dimensions, mass and inertia matrix are listed in Tab.(5.1).

Quantity	**Value**	**Units**
a	20	cm
b	30	cm
Mass	25	Kg
Inertia $\boldsymbol{J}$	diag(22.7 23.3 24.5)	Kg m^2

Table 5.1: Spacecraft dimensions, mass and inertia matrix.

The angle convention used to describe the orientation of the thrust produced by the

engines refers to Fig.(5.2) for E1 and E4 and to Fig.(5.3) for E2 and E3.

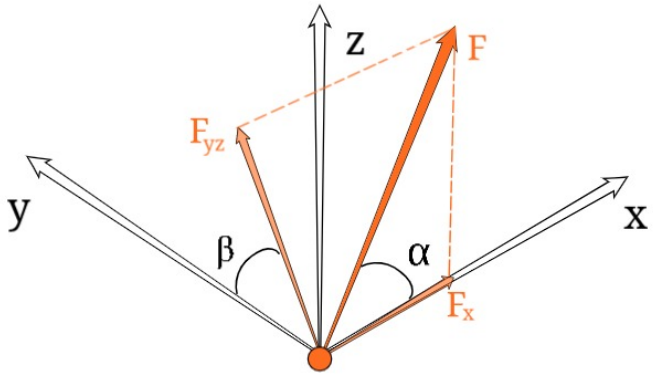

Figure 5.2: Angle convention for E1/E4 thrust direction.

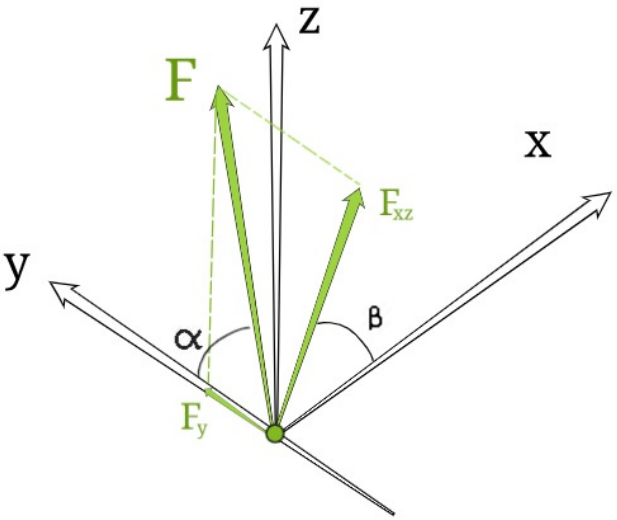

Figure 5.3: Angle convention for E2/E3 thrust direction.

It is thus possible to draw the *Thrust Matrix* $\boldsymbol{T}$, i.e. the matrix that links the engine thrusts to the produced global forces and moments acting on the spacecraft. Eq.(5.1) shows the relation between the produced control inputs $\boldsymbol{\tau}$ and the engine thrust level vector $\boldsymbol{\eta}$. In Eq.(5.1) F_i for $i = x, y, z$ is the produced control force along x, y and z-axis, M_i for $i = x, y, z$ is the produced control torque along x,y and z-axis and η_i for $i = 1, \ldots, 4$ is the thrust magnitude of the i-th engine. Eq.(5.2) shows explicitly the mathematical

definition of $\boldsymbol{T}$ for the chosen configuration and angle convention; s and c stand for sin and cos functions.

$$\boldsymbol{\tau} = \boldsymbol{T}\boldsymbol{\eta} \qquad \boldsymbol{\tau} = \begin{bmatrix} F_x \\ F_y \\ F_z \\ M_x \\ M_y \\ M_z \end{bmatrix} \qquad \boldsymbol{\eta} = \begin{bmatrix} \eta_1 \\ \eta_2 \\ \eta_3 \\ \eta_4 \end{bmatrix} \tag{5.1}$$

$$\boldsymbol{T} = \begin{bmatrix} c\alpha_1 & s\alpha_2 c\beta_2 & s\alpha_3 c\beta_3 & c\alpha_4 \\ s\alpha_1 c\beta_1 & c\alpha_2 & c\alpha_3 & s\alpha_4 c\beta_4 \\ s\alpha_1 s\beta_1 & s\alpha_2 s\beta_2 & s\alpha_3 s\beta_3 & s\alpha_4 s\beta_4 \\ 0 & a(s\alpha_2 s\beta_2) & -a(s\alpha_3 s\beta_3) & 0 \\ b(s\alpha_1 s\beta_1) & 0 & 0 & -b(s\alpha_4 s\beta_4) \\ -b(s\alpha_1 c\beta_1) & -a(s\alpha_2 c\beta_2) & a(s\alpha_3 c\beta_3) & b(s\alpha_4 c\beta_4) \end{bmatrix} \tag{5.2}$$

5.2 Allocation Techniques

In Eq.(5.2) the unknowns to be determined are: η_1, η_2, η_3, η_4, α_1, α_2, α_3, α_4 and β_1, β_2, β_3, β_4. In other words, it must be computed the thrust level of the engines $\boldsymbol{\eta}$ and the orientation of the gimbals described by $\boldsymbol{\alpha} = \begin{bmatrix} \alpha_1 & \alpha_2 & \alpha_3 & \alpha_4 \end{bmatrix}'$ and $\boldsymbol{\beta} = \begin{bmatrix} \beta_1 & \beta_2 & \beta_3 & \beta_4 \end{bmatrix}'$. In order to solve this task there exist plenty of methods; it is firstly necessary to introduce the classical notation of control allocation problem.

The design of control algorithms is often divided into several levels. First, a high level motion control algorithm is designed to compute a vector of virtual inputs $\boldsymbol{\tau_c}$ to the mechanical system. The virtual inputs are usually chosen as a number of forces and moments that equals the number of degrees of freedom that the motion control system wants to control, m, and such that the basic requirement of controllability is met. For a wide range of mechanical systems, this leads to a dynamic model that is linear in the

virtual input and can be written as Eq.(5.3) [20]:

$$\begin{aligned} \dot{\boldsymbol{x}} &= f(\boldsymbol{x}, t) + g(\boldsymbol{x}, t)\boldsymbol{\tau} \\ \boldsymbol{y} &= l(\boldsymbol{x}, t) \end{aligned} \tag{5.3}$$

where f, g, l are functions generally of the state vector $\boldsymbol{x} \in R^n$ and time t, and $\boldsymbol{y}$ is the output vector of the system. $\boldsymbol{\tau}$ is the vector of virtual control inputs that should equal the the output command $\boldsymbol{\tau_c}$ of the high-level motion control algorithm, i.e. $\boldsymbol{\tau} = \boldsymbol{\tau_c}$. For the specific case of the project, $\boldsymbol{\tau_c}$ is the vector condensing the ideal control forces and moments computed from station-keeping and attitude tracking control analyses in Chapter 3 and Chapter 4 while $\boldsymbol{\tau}$ is the produced control input coming from the combination of engines thrust, Eq.(5.1).

Second, a control allocation algorithm is designed in order to map the vector of commanded virtual input forces and moments $\boldsymbol{\tau_c}$ into individual effector forces or moments such that the total forces and moments generated by all effectors amounts to the commanded virtual input $\boldsymbol{\tau_c}$. The relation between virtual control inputs and effector action $\boldsymbol{u}$ is described by Eq.(5.4), which in this context takes the form of Eq.(5.5).

$$\boldsymbol{\tau} = h(\boldsymbol{u}, \boldsymbol{x}, t) \tag{5.4}$$

$$\boldsymbol{\tau} = \boldsymbol{T}(\boldsymbol{\alpha}, \boldsymbol{\beta})\boldsymbol{\eta} \tag{5.5}$$

Eq.(5.5) is the basic equation which rules the control allocation problem. The objective in fact is to optimise $\boldsymbol{\alpha}$, $\boldsymbol{\beta}$ and $\boldsymbol{\eta}$ such that $\boldsymbol{\tau} = \boldsymbol{\tau_c}$ with the minimum possible effort in terms of engine thrusts. The optimisation problem thus reads:

$$\begin{aligned} &\min_{\boldsymbol{\alpha},\boldsymbol{\beta},\boldsymbol{\eta}} \quad f(\boldsymbol{\alpha}, \boldsymbol{\beta}, \boldsymbol{\eta}) = ||\boldsymbol{\eta}|| \\ &\text{subjected to} \begin{cases} \boldsymbol{\tau} = \boldsymbol{\tau_c} = \boldsymbol{T}(\boldsymbol{\alpha}, \boldsymbol{\beta})\boldsymbol{\eta} \\ \boldsymbol{\eta} \geq 0 \end{cases} \end{aligned} \tag{5.6}$$

In the case the primary objective turns out to be unfeasible and constrains are not respected, the control allocation algorithm focuses on the secondary objective of minimising

the error between the produced control command $\boldsymbol{\tau}$ and the desired $\boldsymbol{\tau_c}$. It reads:

$$\begin{aligned} &\min_{\boldsymbol{\alpha},\boldsymbol{\beta},\boldsymbol{\eta}} \quad f(\boldsymbol{\alpha},\boldsymbol{\beta},\boldsymbol{\eta}) = |\boldsymbol{\tau_c} - \boldsymbol{T}(\boldsymbol{\alpha},\boldsymbol{\beta})\boldsymbol{\eta}| \\ &\text{subjected to } \boldsymbol{\eta} \geq 0 \end{aligned} \tag{5.7}$$

Eq.(5.6) and Eq.(5.7) are the most general mathematical expression of the control allocation goals. Anyway it must be noticed that the following problem formulation presents some undesirable mathematical characteristics (from an optimisation point of view): firstly in Eq.(5.6) the constraints are highly non-linear, as it can be noticed from Eq.(5.5); secondly, in Eq.(5.7) non-linear constraints of Eq.(5.6) appear in the cost function $f(\boldsymbol{\alpha},\boldsymbol{\beta},\boldsymbol{\eta})$ which additionally is defined by means of the $L_1 - norm$, adding extra non-linearities to the problem. The presence of non-linearities forces the adoption of non-linear optimisation algorithms which guarantee the convergence to local minimum solutions only under specific assumptions. Moreover they are extremely sensible to the choice of the starting point required to initiate the process; thus, depending on the goodness of initial guess, algorithm performances can strongly be affected and different solutions achieved without any chance of control. These characteristics are enhanced by the presence of strong non-linearities in the problem.

Therefore, it is necessary to find an alternative formulation of the problem to avoid the non-linearities depicted before. The following sections presents the alternative formulations used to run the optimisation process. In fact it is possible to demonstrate that in case of *unconstrained gimbal angles*, the problem 5.6 and 5.7 can be posed in *Linear Programming (LP)* formulation; non-linearities in this case are completely circumvented and *LP algorithms* are employed to find the solution. In case of *constrained gimbal angles* small non-linearities need to be introduce in the constrains; it is thus required to adopt *Non-Linear Programming (NLP) algorithms.*

5.2.1 Linear Programming formulation

Mathematical foundations

The general mathematical programming problem is written as:

$$\min_x f(x)$$
$$\text{subjected to } \begin{cases} h_i(x) = 0 \quad \forall i = 1 \dots m \\ g_j(x) \leq 0 \quad \forall j = 1 \dots r \\ x \in S \end{cases} \tag{5.8}$$

where $f(x)$ is the *cost function*, $h_i(x)$ is the i-th equality constraint, $g_j(x)$ is the j-th inequality constraint ans S is the defined space which the unknown x belongs to. Once the problem is characterised by a cost function linear in the unknowns and the constraints consist in linear equalities and inequalities, the problem is called *Linear Programming (LP) Problem*. The standard formulation of a LP problem is:

$$\min_x f(x) = \boldsymbol{c}'\boldsymbol{x}$$
$$\text{subjected to } \begin{cases} \boldsymbol{A}\boldsymbol{x} = \boldsymbol{b} \\ \boldsymbol{x} \geq 0 \end{cases} \tag{5.9}$$

By means of slack variables and specific expedients, linear inequalities can be embedded in 5.9, as well as the so called *free variables* (not constrained to be non-negative). So considering the constraints, a solution is said to be *feasible* if it satisfies the set of constraints. Moreover under the

- *Full Rank Assumption*: the $m \times n$ matrix $\boldsymbol{A}$ with $m \leq n$ has m lineraly independent rows.

it is possible to give the definition of *(degenerate) basic solution*:

- *Definition*: given the set of m simultaneous linear equations in n unknowns

$$\boldsymbol{A}\boldsymbol{x} = \boldsymbol{b}$$

let $\boldsymbol{B}$ be any non-singular $m \times m$ sub-matrix made up by columns of $\boldsymbol{A}$. Then if all the $n - m$ components of $\boldsymbol{x}$ not associated to columns of $\boldsymbol{B}$ are set equal to

zero, the solution to the resulting set of equations is said to be a *basic solution* with respect to the basis $\boldsymbol{B}$. The components of $\boldsymbol{x}$ associated with columns of $\boldsymbol{B}$ are called *basic variables*. If one or more basic variables in a basic solution have value zero the solution is said to be a *degenerate basic solution*.

Mathematically Eq.(5.10) explains the definition of basic solution $\boldsymbol{x_{bs}}$.

$$\begin{aligned} \boldsymbol{Ax = b} \Longrightarrow \begin{bmatrix} \boldsymbol{B} & \boldsymbol{C} \end{bmatrix} \begin{Bmatrix} \boldsymbol{x_b} \\ \boldsymbol{x_c} \end{Bmatrix} = \boldsymbol{b} \Longrightarrow \begin{cases} \boldsymbol{Bx_b = b} \\ \boldsymbol{Cx_c = 0} \end{cases} \Longrightarrow \begin{cases} \boldsymbol{x_b = B^{-1}b} \\ \boldsymbol{Cx_c = 0} \end{cases} \\ \Longrightarrow \boldsymbol{x_{bs}} = \begin{Bmatrix} \boldsymbol{x_b} \\ \boldsymbol{0} \end{Bmatrix} \end{aligned} \tag{5.10}$$

It is possible to demonstrate that under the *Full Rank Assumption* the system $\boldsymbol{Ax = b}$ has at least one basic solution.

Based on these considerations the *Fundamental Theorem of Linear Programming* is here presented. It is the keystone all the linear programming algorithms.

- *Fundamental Theorem of Linear Programming*: given a linear program as

$$\begin{aligned} &\min_x f(x) = \boldsymbol{c'x} \\ &\text{subjected to } \begin{cases} \boldsymbol{Ax = b} \\ \boldsymbol{x} \geq 0 \end{cases} \end{aligned} \tag{5.11}$$

  where $\boldsymbol{A}$ is a $m \times n$ matrix of rank m, then:

  - if there is a feasible solution, there exists a basic feasible solution.
  - if there exists and optimal feasible solutions, there exists also an optimal basic feasible solution.

The main result of the theorem is that it converts the LP problem into a seek over the set of basic solutions which are then compared to extract the one which minimise the cost

function. It is possible to demonstrate that the basic solution set has at most $n^{\circ}_{B.S.}$ basic solutions, where $n^{\circ}_{B.S.}$ may be computed by Eq.(5.12):

$$n^{\circ}_{B.S.} = \frac{n!}{m!(n-m)!} \tag{5.12}$$

Linear Programming algorithms are extremely easy to implement and fast in execution which makes them ideal candidates for solving control allocation problems.

Control Allocation as LP problem

The Control Allocation problem expressed in Eq.(5.6) may be rewritten in LP formulation only when the gimbals are not affected by any opening angle restriction; conversely, the case of *unconstrained gimbal angles* is solved using LP algorithms. As it is stated in the previous section, the non-linearities affecting the problem 5.6 lie in the explicit formulation of the thrust matrix $\boldsymbol{T}$, Eq.(5.2), where sine and cosine functions of the unknown angles appear in all the equations; they derive from the trigonometric decomposition of the thrust vector along the three body axes. But since the angles are not constrained there is no need to explicitly insert them into the mapping equation Eq.(5.5); it is in fact far more convenient decompose the thrust vector of each engine as simply:

$$\boldsymbol{F}_i = \begin{bmatrix} F_{xi} & F_{yi} & F_{zi} \end{bmatrix} \tag{5.13}$$

where the subscript i stands for the i-th engine. By doing so, the original unknown set $\begin{Bmatrix} \eta_i & \alpha_i & \beta_i \end{Bmatrix}$ is replaced by $\begin{Bmatrix} F_{xi} & F_{yi} & F_{zi} \end{Bmatrix}$ for each engine. Angles no longer appear in the problem formulation as well as non-linearities. The new unknowns are the thrust magnitudes produced by the engines along the body axes.

Firstly we define the function $s(x)$

$$s(x) = \begin{cases} x & \text{if } x > 0 \\ 0 & \text{if } x \leq 0 \end{cases} \tag{5.14}$$

Then each thrust component of each engine, F_{ij}, is decomposed into:

$$F_{ij}^{+} = s(F_{ij}) \qquad F_{ij}^{-} = -s(-F_{ij}) \tag{5.15}$$

so that

$$F_{ij} = F_{ij}^{+} + F_{ij}^{-} \tag{5.16}$$

where $i = x, y, z$ and $j = 1 \dots 4$. Particularly, with regard to F_{x1}^{-}, F_{x4}^{+}, F_{y2}^{+} and F_{y3}^{-}, their value can not be different from zero as it would result in thruster firing inside the spacecraft.

The new set of unknowns is thus:

$$\begin{aligned} \boldsymbol{x} = \Big[& F_{x1} \quad F_{x2}^{+} \quad F_{x2}^{-} \quad F_{x3}^{+} \quad F_{x3}^{-} \quad F_{x4} \quad F_{y1}^{+} \quad F_{y1}^{-} \quad F_{y2} \quad F_{y3} \\ & F_{y4}^{+} \quad F_{y4}^{-} \quad F_{z1}^{+} \quad F_{z1}^{-} \quad F_{z2}^{+} \quad F_{z2}^{-} \quad F_{z3}^{+} \quad F_{z3}^{-} \quad F_{z4}^{+} \quad F_{z4}^{-} \Big] \end{aligned} \tag{5.17}$$

The cost function $f(x)$ to minimize is written as:

$$\begin{aligned} f(\boldsymbol{x}) = & F_{x1} + F_{x2}^{+} - F_{x2}^{-} + F_{x3}^{+} - F_{x3}^{-} - F_{x4} + F_{y1}^{+} - F_{y1}^{-} - F_{y2} + F_{y3} \\ & + F_{y4}^{+} - F_{y4}^{-} + F_{z1}^{+} - F_{z1}^{-} + F_{z2}^{+} - F_{z2}^{-} + F_{z3}^{+} - F_{z3}^{-} + F_{z4}^{+} - F_{z4}^{-} \end{aligned} \tag{5.18}$$

which in vector notation reads:

$$f(\boldsymbol{x}) = \boldsymbol{c'x} \tag{5.19}$$

with

$$\begin{aligned} \boldsymbol{c'} = \Big[& 1 \quad 1 \quad -1 \quad 1 \quad -1 \quad -1 \quad 1 \quad -1 \quad -1 \quad 1 \\ & 1 \quad -1 \quad 1 \quad -1 \quad 1 \quad -1 \quad 1 \quad -1 \quad 1 \quad -1 \Big] \end{aligned} \tag{5.20}$$

The control allocation constraints are formulated as:

$$\begin{cases} F_x^c = F_{x1} + F_{x2}^+ + F_{x2}^- + F_{x3}^+ + F_{x3}^- + F_{x4} \\ F_y^c = F_{y1}^+ + F_{y1}^- + F_{y2} + F_{y3} + F_{y4}^+ + F_{y4}^- \\ F_z^c = F_{z1}^+ + F_{z1}^- + F_{z2}^+ + F_{z2}^- + F_{z3}^+ + F_{z3}^- + F_{z4}^+ + F_{z4}^- \\ M_x^c = a(F_{z2}^+ + F_{z2}^-) - a(F_{z3}^+ + F_{z3}^-) \\ M_y^c = b(F_{z1}^+ + F_{z1}^-) - b(F_{z4}^+ + F_{z4}^-) \\ M_z^c = -b(F_{y1}^+ + F_{y1}^-) - a(F_{x2}^+ + F_{x2}^-) + a(F_{x3}^+ + F_{x3}^-) + b(F_{y4}^+ + F_{y4}^-) \end{cases} \tag{5.21}$$

which in vector notation read:

$$\boldsymbol{\tau_c} = \boldsymbol{A}\boldsymbol{x} \tag{5.22}$$

with

$$\boldsymbol{A} = \begin{bmatrix} \mathbf{1_{1\times 6}} & \mathbf{0_{1\times 14}} & & & & & \\ \mathbf{0_{1\times 6}} & \mathbf{1_{1\times 6}} & \mathbf{0_{1\times 8}} & & & & \\ \mathbf{0_{1\times 14}} & \boldsymbol{a}_{\mathbf{1\times 2}} & -\boldsymbol{a}_{\mathbf{1\times 2}} & \mathbf{0_{1\times 2}} & & & \\ \mathbf{0_{1\times 12}} & \boldsymbol{b}_{\mathbf{1\times 2}} & \mathbf{0_{1\times 4}} & -\boldsymbol{b}_{\mathbf{1\times 2}} & & & \\ \mathbf{0_{1\times 2}} & -\boldsymbol{a}_{\mathbf{1\times 2}} & \boldsymbol{a}_{\mathbf{1\times 2}} & -\boldsymbol{b}_{\mathbf{1\times 2}} & \mathbf{0_{1\times 2}} & \boldsymbol{b}_{\mathbf{1\times 2}} & \mathbf{0_{1\times 8}} \end{bmatrix} \tag{5.23}$$

which must be added the bound constraints to, expressed in Eq.(5.24).

$$\begin{aligned} 0 \leq F_{x1} \leq \infty \\ 0 \leq F_{x2}^+ \leq \infty \\ -\infty \leq F_{x2}^- \leq 0 \\ 0 \leq F_{x3}^+ \leq \infty \\ -\infty \leq F_{x3}^- \leq 0 \\ -\infty \leq F_{x4} \leq 0 \\ 0 \leq F_{y1}^+ \leq \infty \\ -\infty \leq F_{y1}^- \leq 0 \end{aligned} \tag{5.24}$$

$$-\infty \leq F_{y2} \leq 0$$

$$0 \leq F_{y3} \leq \infty$$

$$0 \leq F_{y4}^{+} \leq \infty$$

$$-\infty \leq F_{y4}^{-} \leq 0$$

$$0 \leq F_{z1}^{+} \leq \infty$$

$$-\infty \leq F_{z1}^{-} \leq 0$$

$$0 \leq F_{z2}^{+} \leq \infty$$

$$-\infty \leq F_{z2}^{-} \leq 0$$

$$0 \leq F_{z3}^{+} \leq \infty$$

$$-\infty \leq F_{z3}^{-} \leq 0$$

$$0 \leq F_{z4}^{+} \leq \infty$$

$$-\infty \leq F_{z4}^{-} \leq 0$$

The problem is definitely well-posed to be handled by LP algorithms. The numerical results and their discussion are reported in Section 5.3.

5.2.2 Control Allocation as NLP problem

When gimbal angle limitations have to be taken into account it is necessary to introduce non-linear constraints in the problem formulation. As it was highlighted previously, the angles are the responsible of such non-linearities.

In order to keep the formulation as close as possible to Linear Programming one, it is added to the previous LP formulation (kept unaltered) the angle limitations expressed as force magnitude ratios. More precisely, gimbals are limited to move inside the cone aligned to the gimbal axis and, whose opening is defined by the maximum allowable angle. The cone angle then defines the maximum ratio between the projection of the thrust onto the cone axis and the force projection onto the plane defined by the cone axis itself. Fig.(5.4) explains the concept.

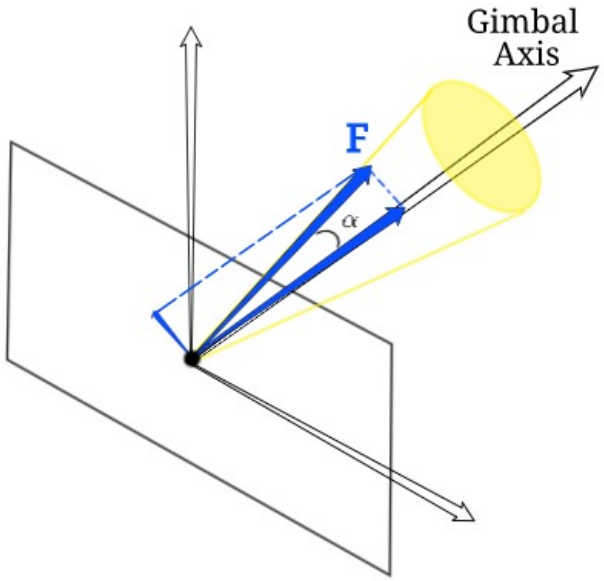

Figure 5.4: Gimbal cone of allowed directions.

Since the cone axis of E1-E4 coincides with the spacecraft body x-axis, and the cone axis of E2-E3 coincides with the body y-axis, the non-linear constraints can easily be represented by means of the thrust components along the CubeSat body axes, Eq.(5.25).

$$\begin{aligned}
\frac{\sqrt{F_{y1}^2 + F_{z1}^2}}{F_{x1}} &\leq tan(\alpha_1^{max}) \\
-\frac{\sqrt{F_{x2}^2 + F_{z2}^2}}{F_{y2}} &\leq tan(\alpha_2^{max}) \\
\frac{\sqrt{F_{x3}^2 + F_{z3}^2}}{F_{y3}} &\leq tan(\alpha_3^{max}) \\
-\frac{\sqrt{F_{y4}^2 + F_{z4}^2}}{F_{x4}} &\leq tan(\alpha_4^{max})
\end{aligned} \tag{5.25}$$

The cost function remains unaltered with respect to LP formulation, as well as the other constraints and bounds. NLP algorithm must be used in order to deal with the new non-linear constraints. For the project, the *Interior-Point Method* is chosen for the simulations. Numerical results and their discussion are presented in Section 5.3.

5.3 Numerical results

This section represent the core part of the control allocation procedure and it is intended to validate the project baseline idea. Two different cases are exposed; the first, the *Unconstrained Gimbal* case, is the ideal scenario from a technological point of view where the thrust vectoring control is able to span the whole available space. The second, the *"Constrained Gimbal"* case, takes into consideration the practical technological issues which affect orientation mechanisms for deep-space missions.

The commanded virtual inputs $\boldsymbol{\tau_c}$ used are the control forces and moments computed in Chapter 3 and Chapter 4. Correspondingly, the nominal orbits chosen are the ones adopted in Chapter 3 whose features are listed in Tab.(3.2), Tab.(3.4) and Tab.(3.6). The commanded virtual forces of Chapter 3, which were expressed in the co-rotating reference frame, are translated into body reference frame coordinates using the Direct Cosine Matrix evaluated along the orbit. For sake of completeness, the ideal input traces $\boldsymbol{\tau_c}$ are presented from Fig.(5.5) to Fig.(5.7), for each nominal orbit.

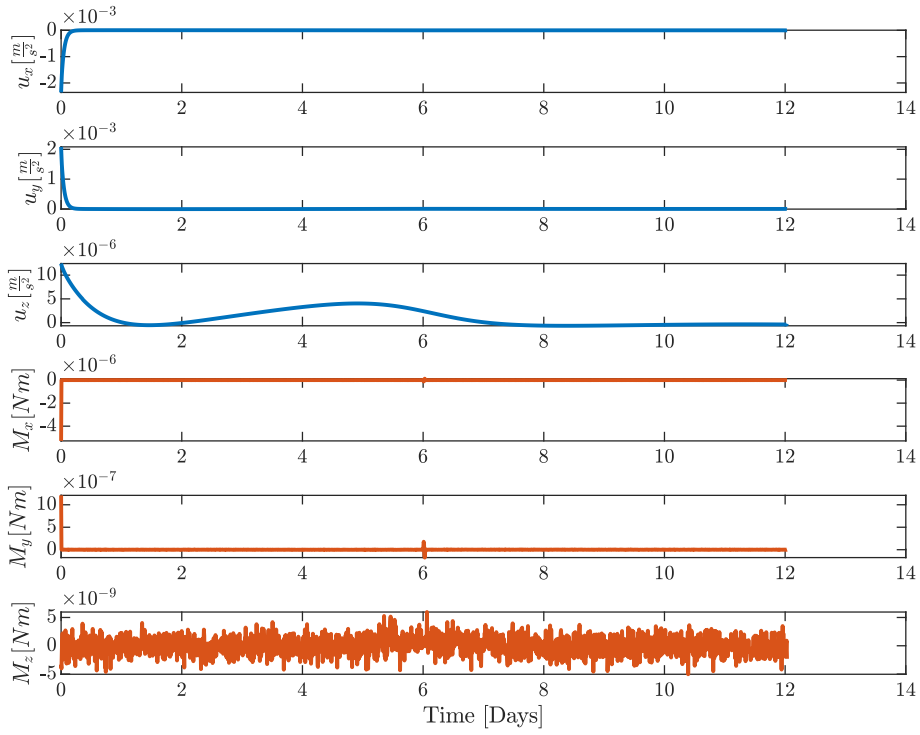

Figure 5.5: Commanded virtual inputs $\boldsymbol{\tau_c}$ for Halo orbit

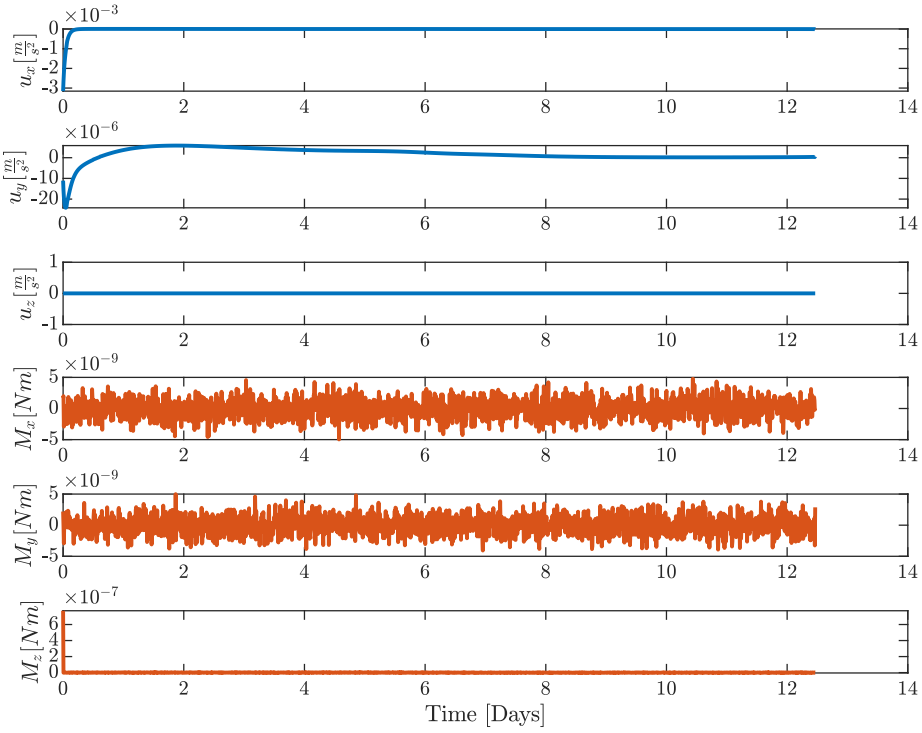

Figure 5.6: Commanded virtual inputs $\boldsymbol{\tau_c}$ for Lyapunov orbit

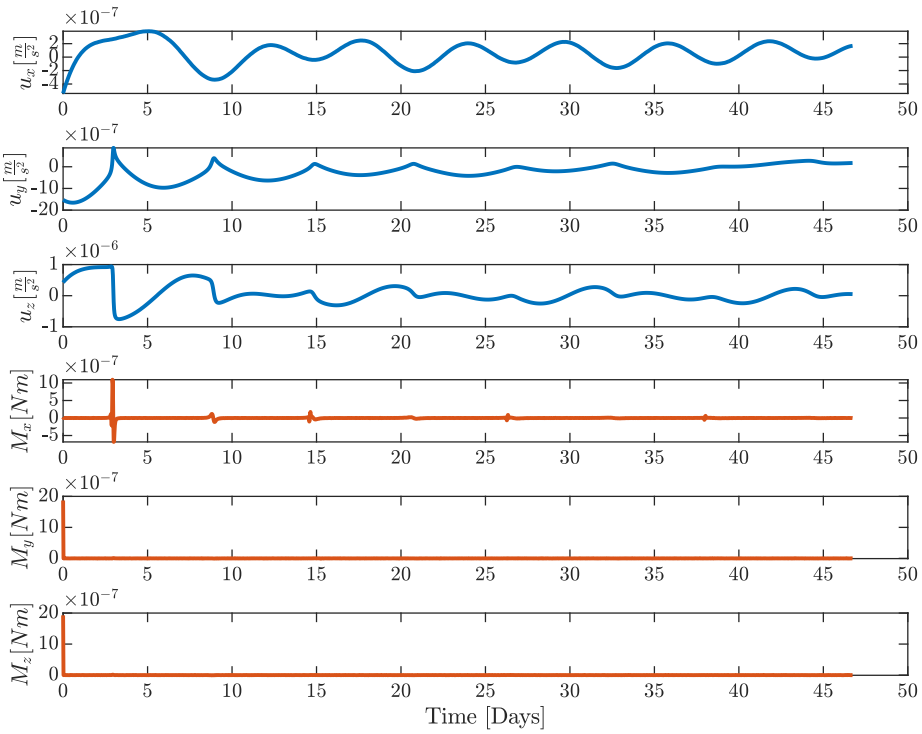

Figure 5.7: Commanded virtual inputs $\boldsymbol{\tau_c}$ for Lissajous orbit

5.3.1 Unconstrained Gimbal Case

The ideal traces are mapped onto the engines using LP *Dual-Simplex Algorithm*. Since the CubeSat dynamics is affected by initial errors, a transient region dominated by strong virtual commanded control efforts is present. In this region the control algorithm acts decisively to guide the spacecraft to its nominal path. In order to better highlight the engines behaviour, the mapping results in the transient zone and in the steady-state zone is analysed separately, as the engine thrust levels differ by several order of magnitudes from one region to the other.

Halo Orbit

The control allocation procedure produces satisfactory results as the commanded virtual inputs $\boldsymbol{\tau_c}$ are perfectly matched by proper coordination of gimbal directions and engine thrusts. As it can be noticed in Fig.(5.8) the error between produced control efforts and ideal ones remains practically zero throughout the entire mission.
Fig.(5.9) and Fig.(5.10) shows the engine thrust envelops of the mission. In Fig.(5.11) the gimbal mechanism envelops are presented.
Significant pieces of information are condensed also in Fig.(5.12). The overall contribution of each engine to each control input is reported by means of pie charts where the comparison of respecitve influences upon control degrees of freedom (DOFs) turns out to be easier and more intuitive to be caught. It must be noticed that the overall produced control input may exceed the amount requested by the high level motion control; this is due to the fact that engines are free to operate in opposite mode, i.e. they can produce forces and moments which cancel out the contributions coming from other engines. Only the absolute values of the contributions are considered, not their sign as they represent the real work provided by each thruster. Referring to Fig.(5.12) the superscript ^{c} refers to the commanded virtual control input and for each pie chart it is reported the ration between the produced control input and the commanded ideal one.

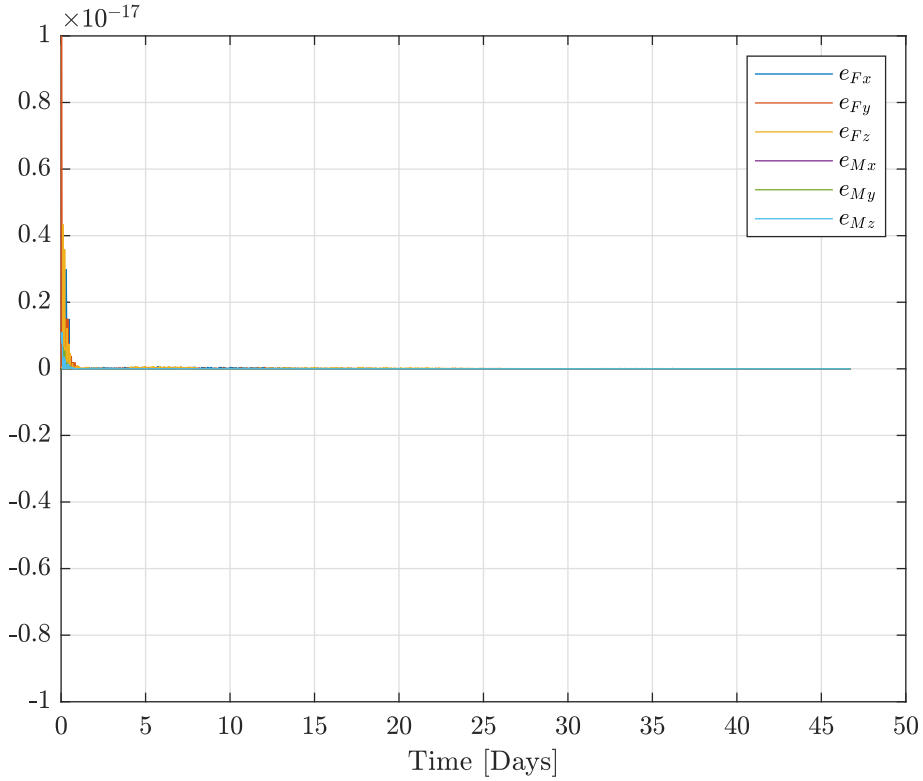

Figure 5.8: Unconstrained gimbal angles - Halo orbit: evolution of the mapping error: $\boldsymbol{e} = \boldsymbol{\tau_c} - \boldsymbol{\tau}$

.

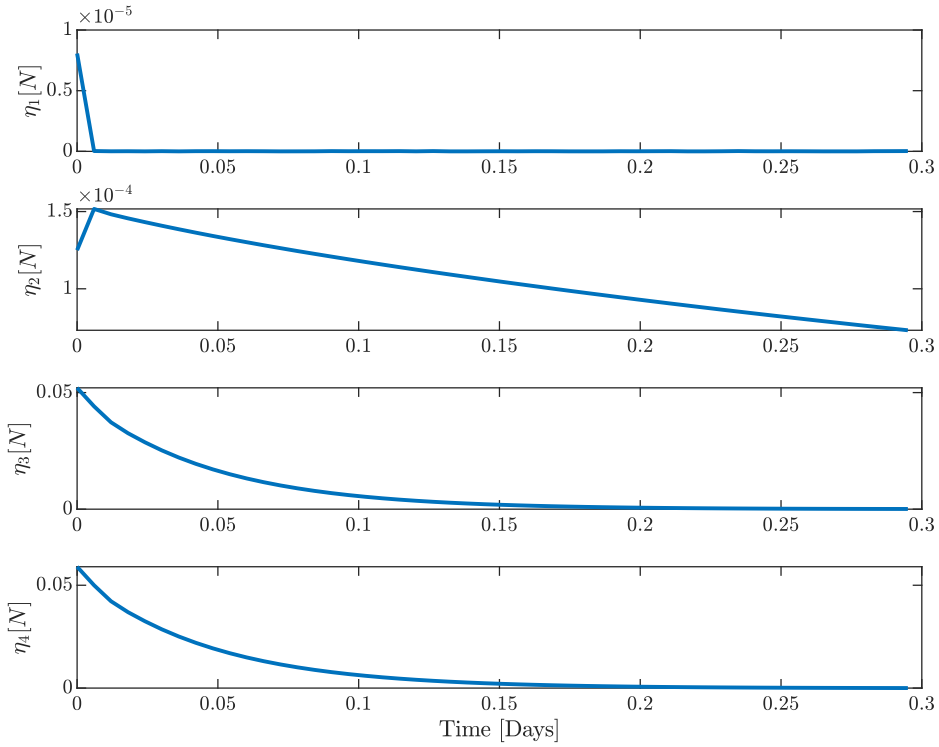

Figure 5.9: Unconstrained gimbal angles - Halo orbit: transient behaviour of engine thrust levels.

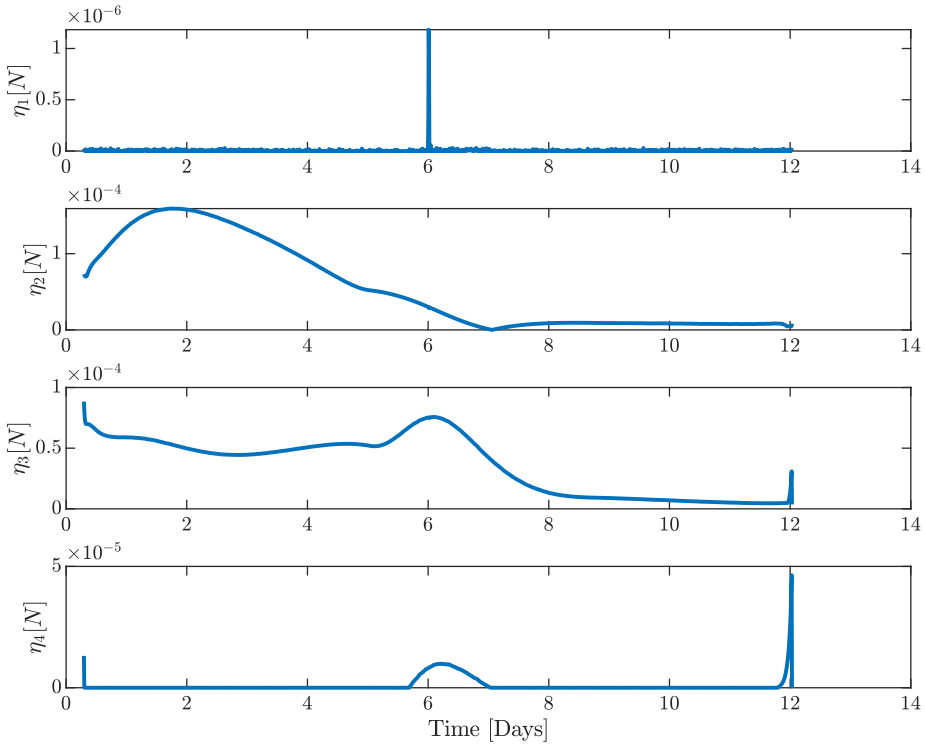

Figure 5.10: Unconstrained gimbal angles - Halo orbit: steady state behaviour of engine thrust levels.

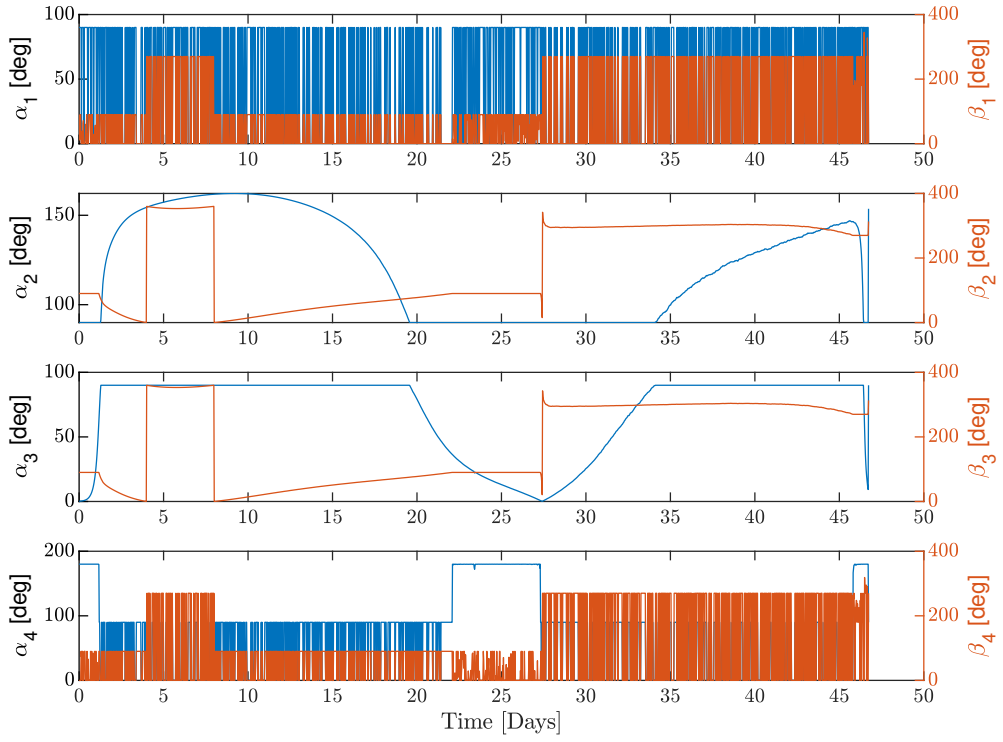

Figure 5.11: Unconstrained gimbal angles - Halo orbit: gimbal orientation during the mission. The right-hand side axis refers to the α angle, the left-hand side axis concerns the β angle. Conventions for α and β are shown in Section 5.1 Fig.(5.2) and Fig.(5.3).

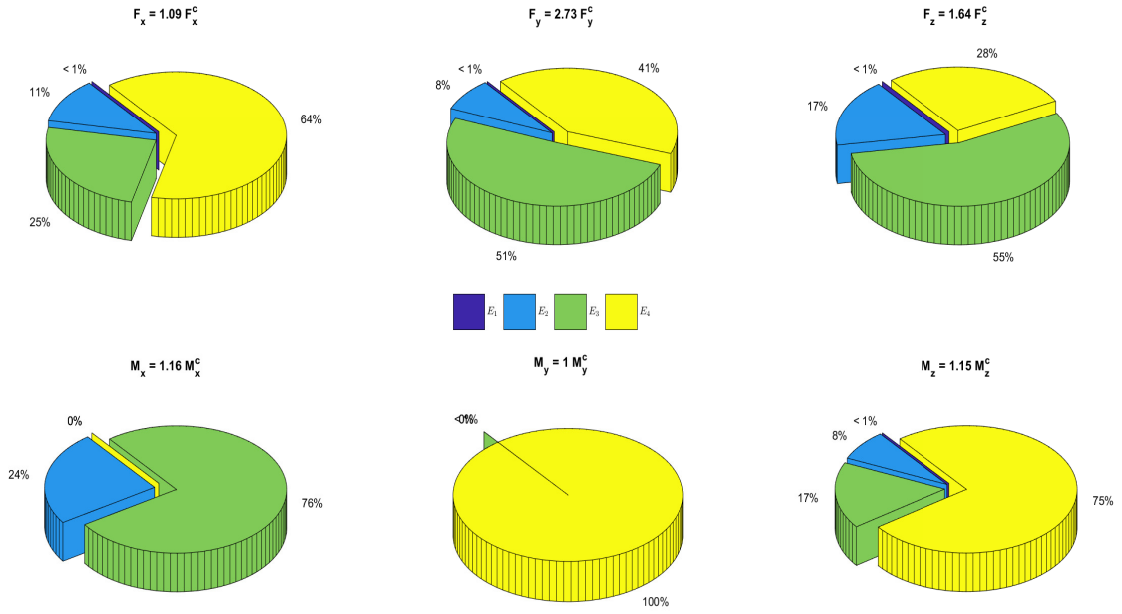

Figure 5.12: Unconstrained gimbal angles - Halo orbit: engine contributions to control inputs. The title of each pie chart represents the ration between the commanded ideal input (denoted by the superscript ^{c}) and the produced one in terms of absolute values. Ratios may exceed unity as only the absolute values of the contributions are considered, not their sign.

From the results proposed by Fig.(5.8) to Fig.(5.11) it is possible to draw some important considerations.

Firstly, it's good to point it out, the engine configuration and the control allocation strategy are perfectly capable of achieving the goals for which they were designed. In the case of a mission in Halo orbit adopting unconstrained thrust vectoring control, the project baseline idea is proved to work properly.

Afterwards, it is good to analyze how the dual-simplex algorithm exploits the propulsion system resources to match the commanded virtual inputs. Engine E1, which is intuitively the most suitable to compensate for the demands along the positive x-axis direction is almost completely out of control roles. In its place, Engines E2, E3 and E4 intervene in a predominant manner in every degree of freedom (DOF). E1 thus appears to be used just for small corrections in specific directions throughout the duration of the mission, as it can be deduced by its thrust level and orientation. In fact, E1 positions never deviates from the noteworthy angles of 0° and 90° for α_1, and 0°, 90°, 180° and 270° for β_1.

Max. Error	e_{Fx} = 2.98e-18
	e_{Fy} = 1.79e-17
	e_{Fz} = 4.33e-18
	e_{Mx} = 5.13e-21
	e_{My} = 6.41e-18
	e_{Mz} = 1.10e-18
Thrust Range	E_1 = [8.06e-06 - 0] [N]
	E_2 = [1.59e-04 - 1.29e-07] [N]
	E_3 = [0.052 - 3.63e-06] [N]
	E_4 = [0.059 - 0] [N]
Average Thrust	E_1 = 8.8752e-09 [N]
	E_2 = 5.6868e-05 [N]
	E_3 = 2.3598e-04 [N]
	E_4 = 2.2711e-04 [N]
Global Av. Thrust	1.2999e-04 [N]
Global Max. Err	1.79e-17
Max. Thrust	T_{MAX} = 0.059 [N]

Table 5.2: Unconstrained gimbals, Halo orbit case - control allocation main results.

E4, on the contrary, plays a dominant role in all degrees of freedom that it is able to intervene on. In the transient region, together with engine E3, it is the primary responsible of the control effort of the satellite. Once the transient ends, its behaviour gets closer to engine E1. Similarly to engine E1, E4 is used mainly to produce control action aligned to the satellite body reference frame. Considering the big drop in thrust magnitude between transient and steady state phases, E4 seems to be adopted mainly during the former phase, after which E2 and E3 seem to be assuming its control duties. It is possible to conclude that the transient phase is mainly ruled by the combination of not-aligned engines (in this case E3 and E4), while during the steady state, E2 and E3 aligned engines can handle

the bulk of the required control effort. Finally, engines E2 and E3 appear to operate in a more coordinate manner in the steady state phase. Because they are preferred to E1 and E4 in steady state conditions, their thrust direction has a more fluctuating trend with respect to E1 and E4 which suggests a multi-tasking control role. If engine E1 and E4 are commanded to provide "*impulsive*", efficient control inputs over one degree of freedom at a time, engine E2 and E3 appear to cover more DOFs using intermediate thrust directions (i.e. not properly aligned with body axes). Such behaviour would explain their higher thrust magnitude in steady state conditions. The last consideration concerns the ratios in Fig.(5.12); the control in F_y and F_z appears to be sensitively affected by cancellation effects, i.e. engines produce control inputs which cancel out the effects produced by other engines. Particularly the control for F_y turns out to be quite "inefficient".
Tab.(5.2) summarise the most relevant results.

Lyapunov Orbit

Also for missions in Lyapunov orbit the propulsion system coordinated by the allocation algorithm is able to produce the required commanded virtual inputs $\boldsymbol{\tau_c}$. Fig.(5.13) shows clearly that mapping errors are kept practically to zero throughout the whole mission.
As it is done for the Halo case, Fig.(5.14) and Fig.(5.15) present the thrust envelops of the four engines while Fig.(5.16) shows gimbal ones. Similarly to the previous case, the control contribution of each engine with respect to each control DOF is evaluated in Fig.(5.17). It shall always be noted that the contribution is evaluated in absolute values, thus the ratio between produced control effort and required one may exceed unity as cancellations arising from opposite sign contributions are not taken into account.

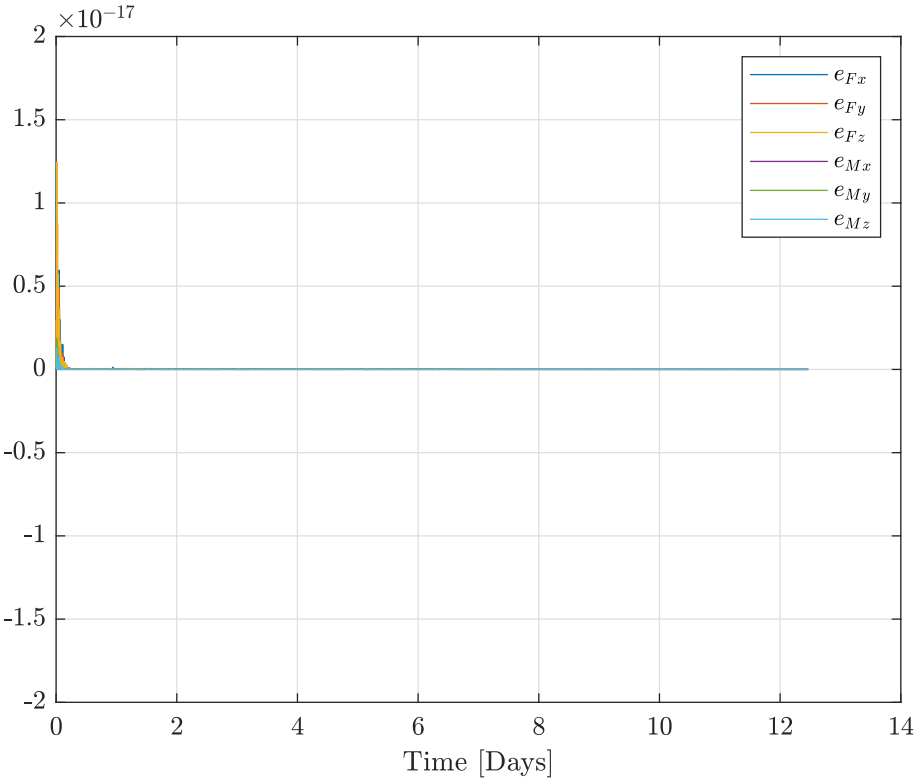

Figure 5.13: Unconstrained gimbal angles - Lyapunov orbit: evolution of the mapping error: $\boldsymbol{e} = \boldsymbol{\tau_c} - \boldsymbol{\tau}$

.

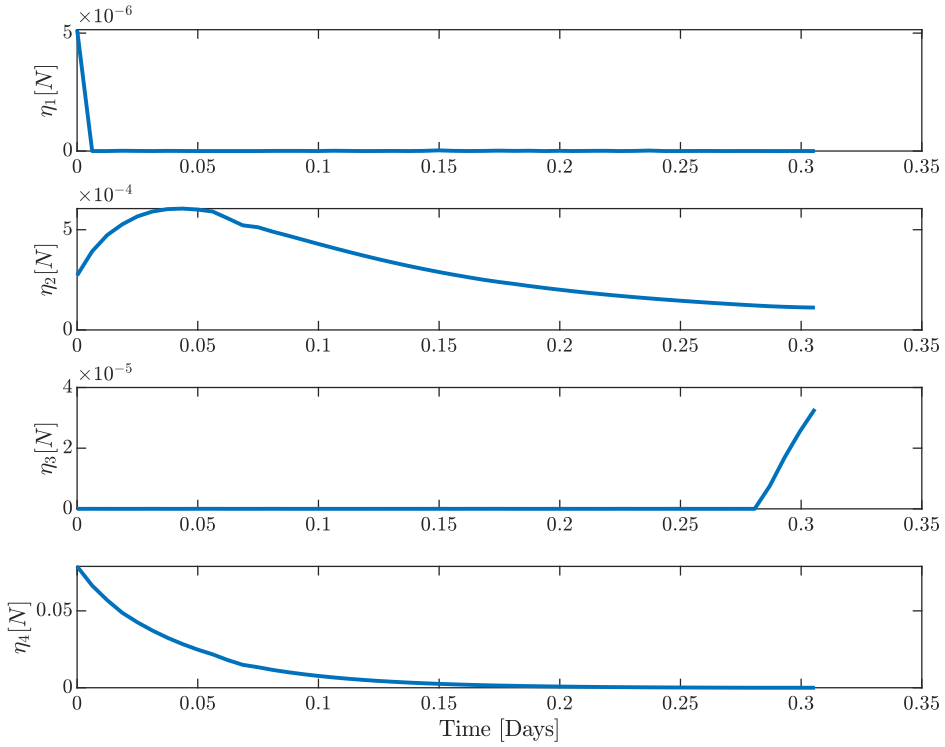

Figure 5.14: Unconstrained gimbal angles - Lyapunov orbit: transient behaviour of engine thrust levels.

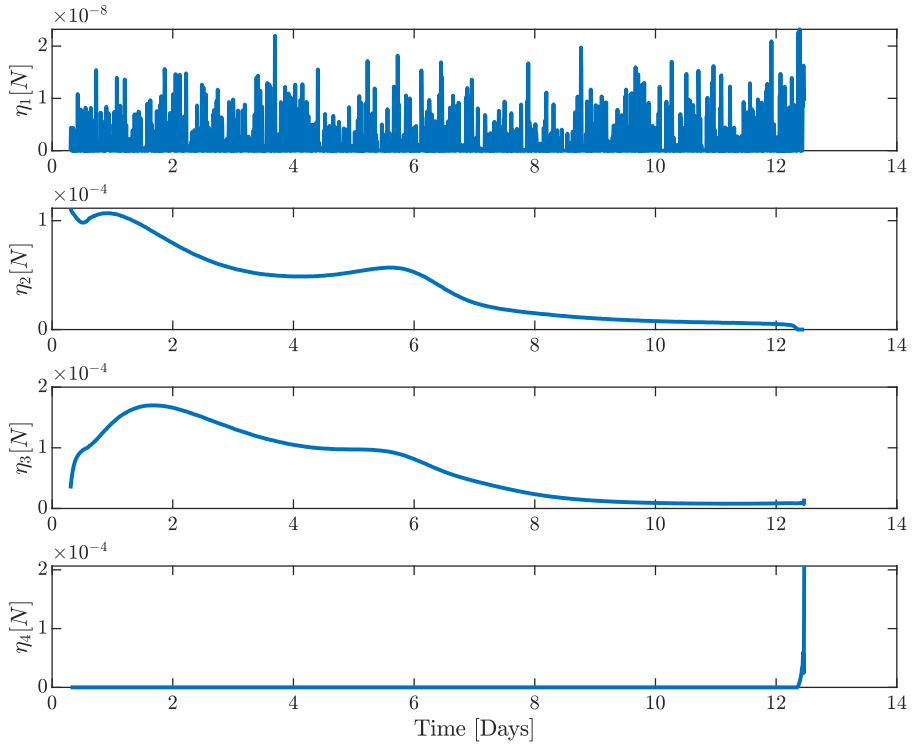

Figure 5.15: Unconstrained gimbal angles - Lyapunov orbit: steady state behaviour of engine thrust levels.

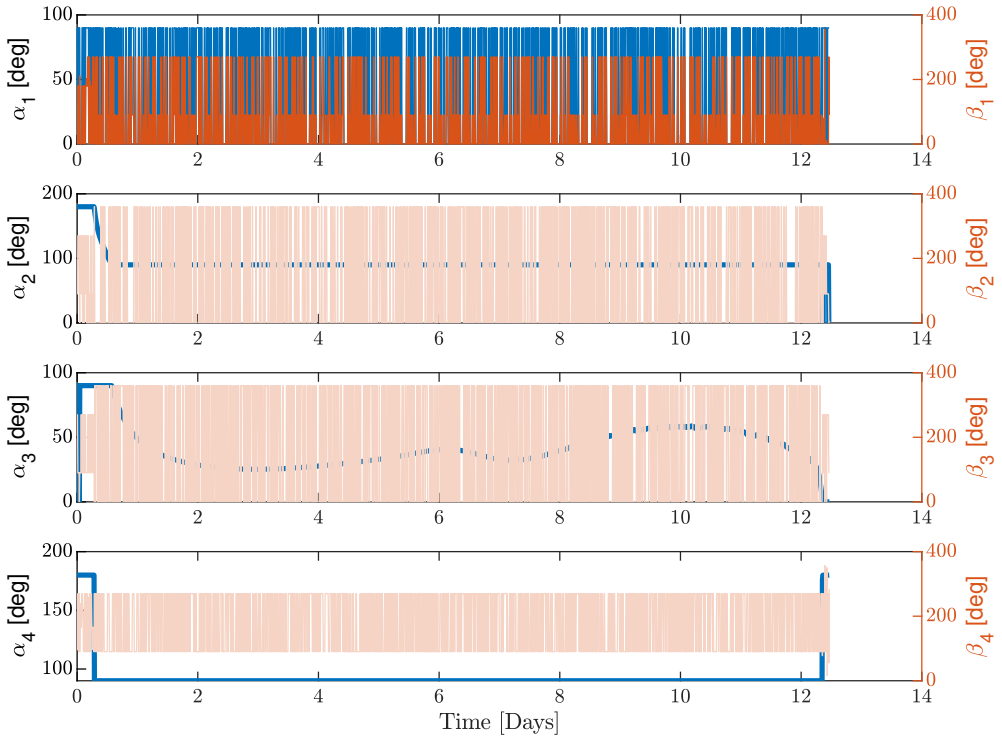

Figure 5.16: Unconstrained gimbal angles - Lyapunov orbit: gimbal orientation during the mission. The right-hand side axis refers to the α angle, the left-hand side axis concerns the β angle. Conventions for α and β are shown in Section 5.1 Fig.(5.2) and Fig.(5.3).

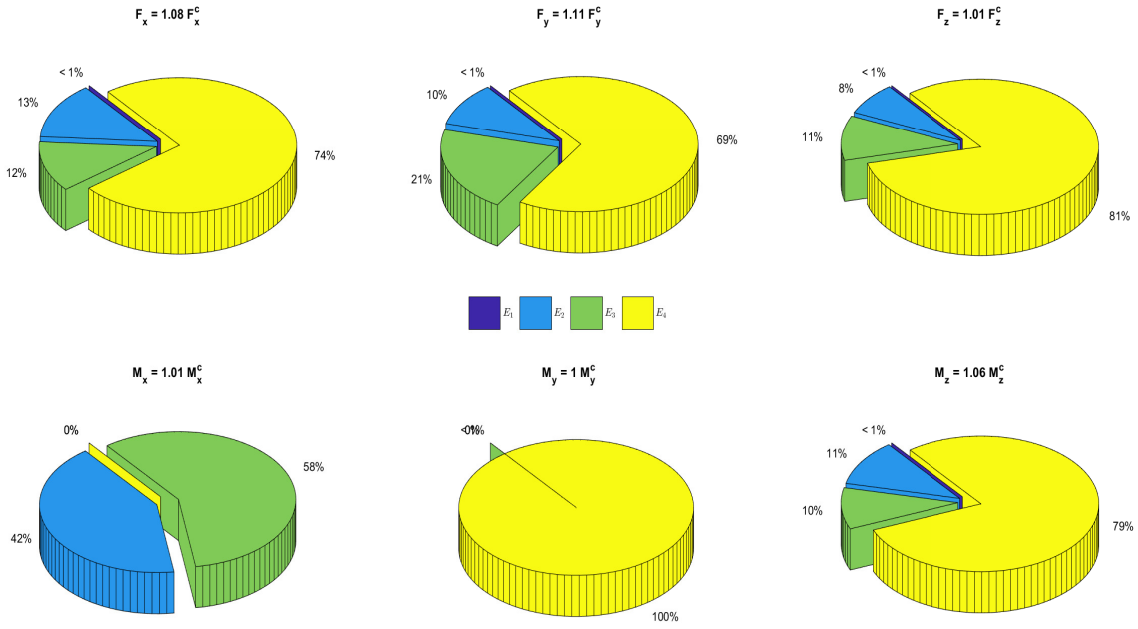

Figure 5.17: Unconstrained gimbal angles - Lyapunov orbit: engine contributions to control inputs. The title of each pie chart represents the ration between the commanded ideal input (denoted by the superscript ^{c}) and the produced one in terms of absolute values. Ratios may exceed unity as only the absolute values of the contributions are considered, not their sign.

Also for the nominal Lyapunov orbit, the control allocation procedure is capable of coordinating the engine directions and thrusts to keep the spacecraft close to its nominal orbit and orient it properly during the whole mission. The control allocation objectives are perfectly reached and no mapping errors affect the spacecraft dynamics.
Similarly to the Halo orbit case, the engine E1 plays a marginal role in the spacecraft control. The values of α_1 keep on oscillating between 0° and 90° degrees as well as β_1 which often reach 270° as well. As it was for the precedent case, E1 is exploited for small corrections, while the bulk of the control task is devoted primarily to E4 during the transient phase and to E2 and E3 in the steady state region. Fig.(5.17) highlights the key role of E4 in providing the required control effort. During the transient period, the control allocation algorithm makes intensively use of E4 to deliver the vast majority of the amount of control forces and moments needed by the high level motion control. Not surprisingly, the thrust level of E4 is several order of magnitude greater than the one provided by the other thrusters. It must be kept in mind that it is during the transient period that the largest amount of control actions is requested, thus, as this task pours more into E4, the contribution of E4 results preponderant compared to the contribution of other engines. It is interesting to note how after the transient, where the α_4 position slightly varies around 180° and E4 provides the greatest amount of thrust, the engine gets practically shut down (such consideration comes from the α_4 value which is set to zero); in turn E3 starts working providing almost the entire control effort needed, in conjunction with E2 and E1. The gimbal angle β_4 provide significant pieces of information only when α_4 is different form 0°, values that is used in the simulation as indication of the engine inactivity; E4 working with $\alpha_4 = 0$ would result the engine firing on the spacecraft body. During the period of activity of E4, β_4 never strays from 90° and 270°, which explain why M_y is uniquely supplied by this engine. In steady state conditions, the control allocation procedure behaves similarly to the Halo case. E1 is mainly used to perform small impulsive corrections along the body axes of the spacecraft. E4 is turned off, except at the end when it performs small corrections, and the control of the spacecraft is mainly entrusted to E2 and E3. Differently from the Halo case, here the control allocation achieve to provide all

the control inputs in an efficient way; all the ratios in Fig.(5.17) are close to unity which means that almost no cancellation occur.

Tab.(5.3) summarise the most relevant results.

Max. Error	$e_{Fx} = 1.19\text{e-}17$
	$e_{Fy} = 8.42\text{e-}18$
	$e_{Fz} = 1.24\text{e-}17$
	$e_{Mx} = 1.27\text{e-}20$
	$e_{My} = 1.86\text{e-}18$
	$e_{Mz} = 1.26\text{e-}18$
Thrust Range	$E_1 = [5.14\text{e-}06 - 0]$ [N]
	$E_2 = [6.05\text{e-}04 - 0]$ [N]
	$E_3 = [1.7\text{e-}04 - 0]$ [N]
	$E_4 = [0.079 - 5.75\text{e-}12]$ [N]
Average Thrust	$E_1 = 4.3513\text{e-}09$ [N]
	$E_2 = 4.6553\text{e-}05$ [N]
	$E_3 = 6.7360\text{e-}05$ [N]
	$E_4 = 2.8664\text{e-}04$ [N]
Global Av. Thrust	1.0014e-04 [N]
Global Max. Err	1.24e-17
Max. Thrust	$T_{MAX} = 0.079$ [N]

Table 5.3: Unconstrained gimbals, Lyapunov orbit case - control allocation main results.

Lissajous Orbit

Definitely Lissajous results confirm the functioning of the procedure. The baseline idea of the project is completely proved to work when gimbal angles are not constrained. No mapping errors arise also in the Lissajous case, as it can be noticed from Fig.(5.18) The control allocation results are exposed from Fig.(5.19) to Fig.(5.21). As it is staded in Chapter 2, Lissajous orbits are defined analytically and no numerical scheme is used for their simulation. It results in a significant approximation error which implies a tougher control effort to keep the spacecraft close to its nominal orbit. It implies also that there is no transient period in terms of control efforts; the control is always called to correct the spacecraft position throughout the mission and initial errors do not require stronger control inputs to be accommodated, compared to the ones used just for station-keeping purposed.

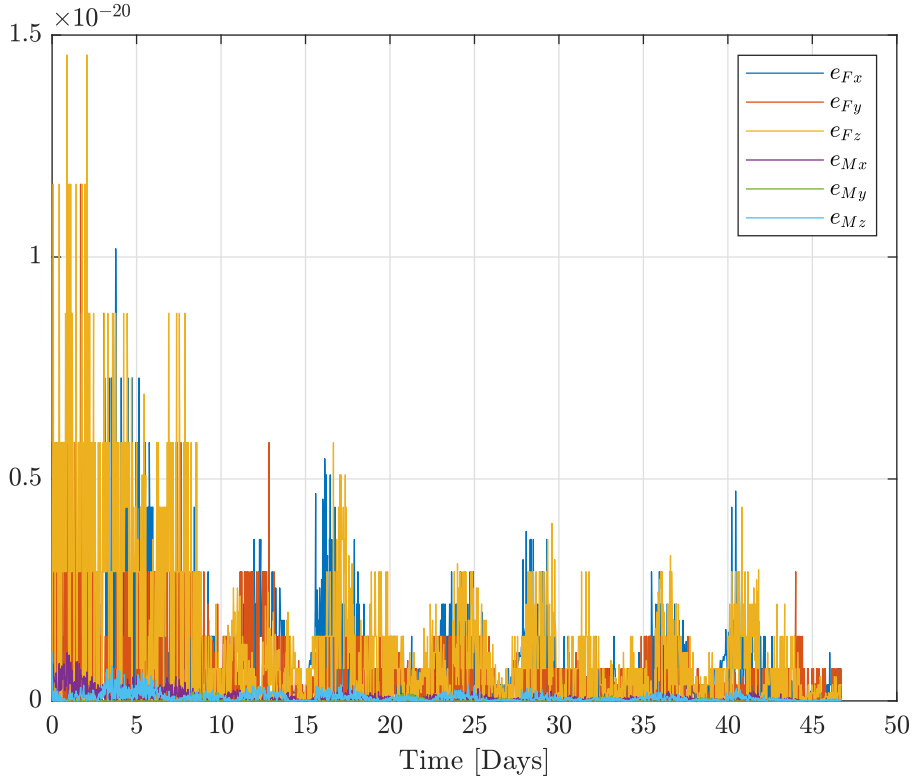

Figure 5.18: Unconstrained gimbal angles - Lissajous orbit: evolution of the mapping error: $\boldsymbol{e} = \boldsymbol{\tau_c} - \boldsymbol{\tau}$

.

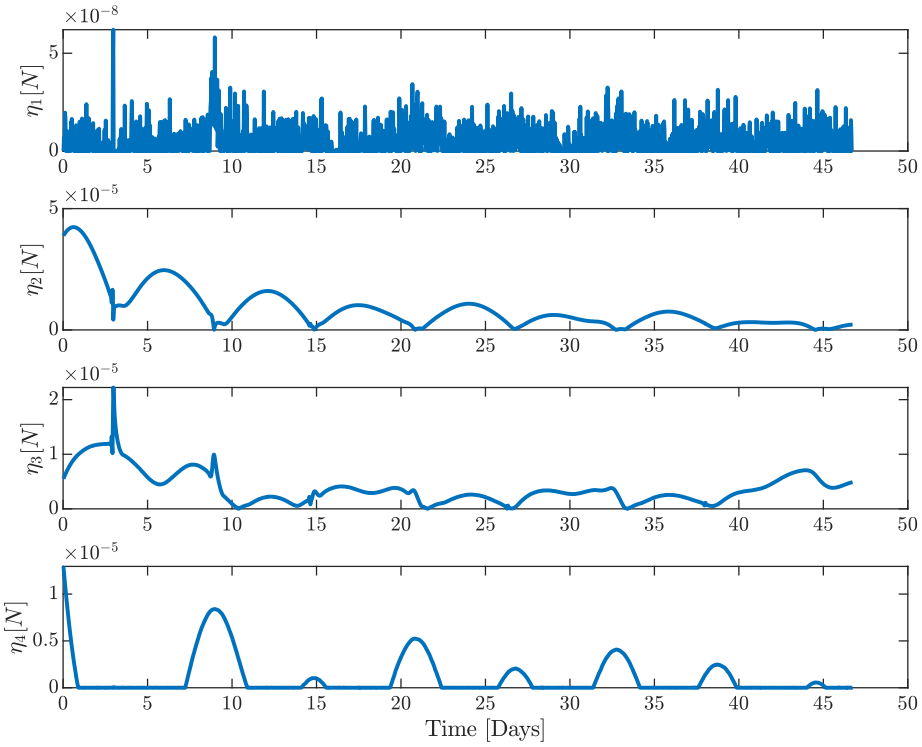

Figure 5.19: Unconstrained gimbal angles - Lissajous orbit: Thrust envelop of the mission.

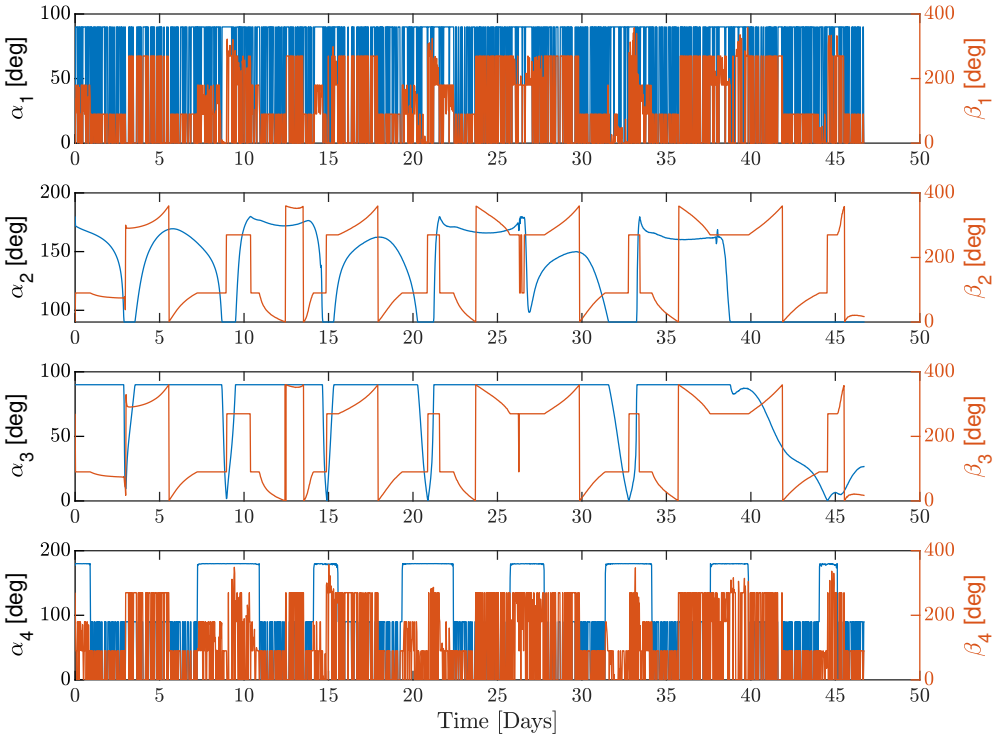

Figure 5.20: Unconstrained gimbal angles - Lissajous orbit: gimbal orientation during the mission. The right-hand side axis refers to the α angle, the left-hand side axis concerns the β angle. Conventions for α and β are shown in Section 5.1 Fig.(5.2) and Fig.(5.3).

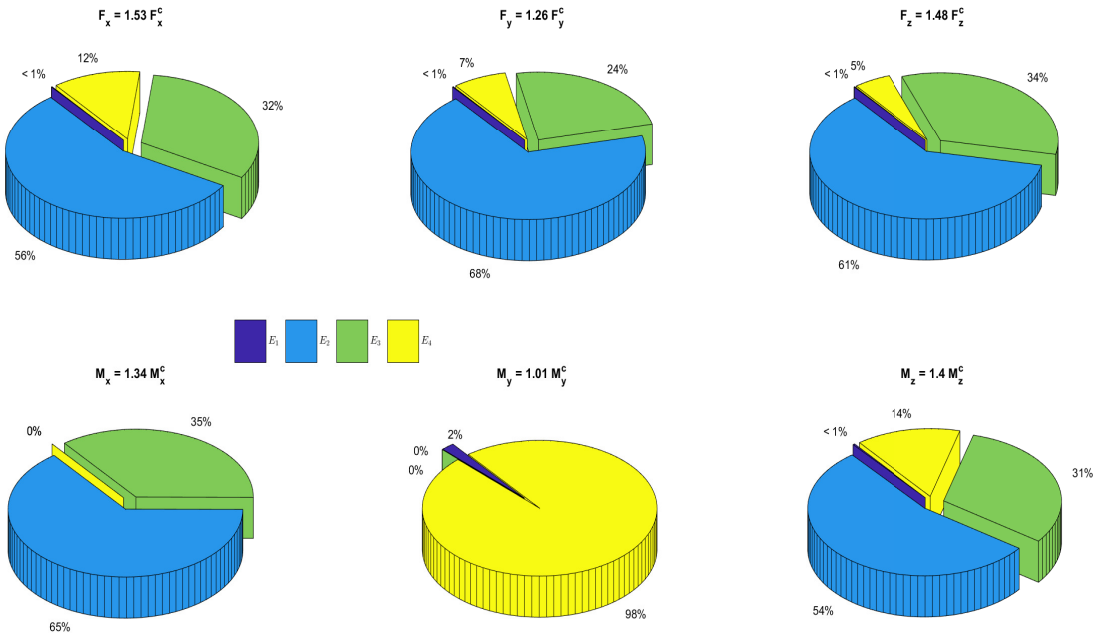

Figure 5.21: Unconstrained gimbal angles - Lissajous orbit: engine contributions to control inputs. The title of each pie chart represents the ration between the commanded ideal input (denoted by the superscript ^{c}) and the produced one in terms of absolute values. Ratios may exceed unity as only the absolute values of the contributions are considered, not their sign.

Lissajous results confirm the marginal role of engine E1. Also in this case the E1 thrust magnitude has lower values with several orders of magnitude of difference with respect to the other engine thrusts. Nonetheless, the E1 feeble contributes appear to have a non negligible impact on M_y control. Generally, the control effort is more equally allocated among E2, E3 and E4. The role of the latter, except in M_y, is downsized to the advantage of E2 and E3 which take on most of the control work. Since E4 remains the principal actuator handling M_y control, β_4 keeps dwelling at around 90° and 270° but in a looser way with respect to previous cases; intermediate values of β_4 appear clearly and quite frequently from Fig.(5.20). The same consideration is valid for E1 attitude. The thrust vectoring control of E2 and E3 is always requested to span almost the entire space allowable in order to properly contribute to all the control DOFs. The Lissajous control allocation is affected by engine cancellation effects which characterise all the control degrees.

Finally, Tab.(5.4) condenses the main results of the Lissajous case.

Max. Error	e_{Fx} = 1.02e-20
	e_{Fy} = 1.16e-20
	e_{Fz} = 1.45e-20
	e_{Mx} = 1.08e-21
	e_{My} = 3.64e-22
	e_{Mz} = 1.09e-21
Thrust Range	E_1 = [1.73e-05 - 0] [N]
	E_2 = [4.23e-05 - 6.53e-09] [N]
	E_3 = [2.22e-05 - 1.74e-09] [N]
	E_4 = [1.35e-05 - 0] [N]
Average Thrust	E_1 = 1.4193e-08 [N]
	E_2 = 8.5341e-06 [N]
	E_3 = 3.7916e-06 [N]
	E_4 = 1.0648e-06 [N]
Global Av. Thrust	3.3512e-06 [N]
Global Max. Err	1.16e-20
Max. Thrust	T_{MAX} = 4.23e-05 [N]

Table 5.4: Unconstrained gimbals, Lissajous orbit case - control allocation main results.

5.3.2 Constrained Gimbal Case

In the present case the gimbal mechanisms are not allowed to span all the space at their disposal. They are limited to move inside a cone aligned with the gimbal axis whose opening coincides with the maximum permitted angle. Fig.(5.4) represents graphically the concept. This section, together with *"Unconstrained Gimbal Case"* part, represent the core foundation of the work; unlike the latter, here practical technological limitations are taken into account so it takes on an important meaning from a practical point of view. For each orbit case, the control allocation procedure is tested for different angle limitations which are: $\alpha_{max} = 45°$, $\alpha_{max} = 20°$, $\alpha_{max} = 10°$ and $\alpha_{max} = 5°$ degrees. In the first part

of the section, mapping errors and engines thrust ranges are compared for all the values of α_{max} and for all the orbits. The intent is to underline the effects that α_{max} has on the satellite dynamics in terms of control effort and perturbation production. Nevertheless, a detailed report of all the results concerning all the α_{max} values for all the orbit considered so far, would lead to an overly disperse discussion; for sake of compactness, considering the recent developments pursued by NASA in CubeSat gimbal technologies [31], $\alpha_{MAX} = 10°$ is used as representative case to present the results in details, in the same way it is done for the unconstrained gimbals case.

Global results

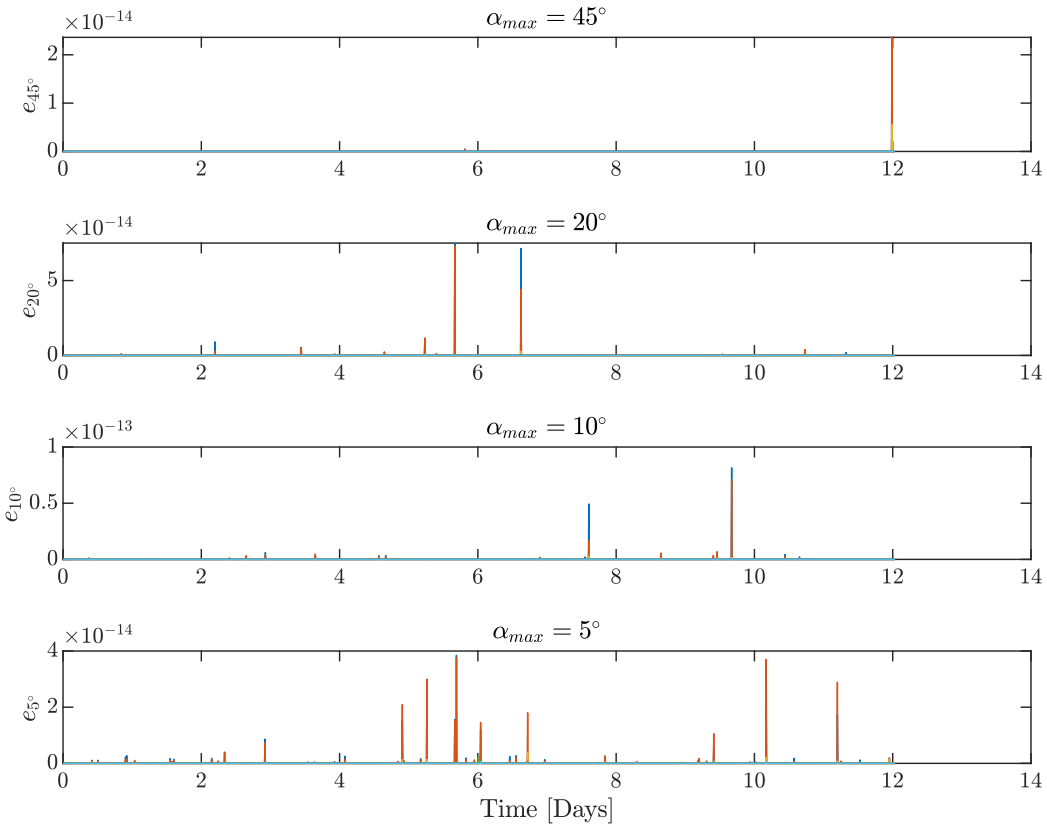

Figure 5.22: Control allocation mapping errors for Halo mission case. Each subplot refers to a specific α_{max}.

The mapping errors produced by the allocation procedure during the mission in Halo, Lyapunov and Lissajous orbits are presented from Fig.(5.23) to Fig.(5.24). Each subplot refers to a specific case of α_{max}. Thrust magnitude information is collected in Fig.(5.25), Fig.(5.26) and Fig.(5.27). Specifically, Fig.(5.25) shows the thrust ranges without distinction among the engines; the minimum thrust and the maximum thrust here appearing are the minimum and maximum thrust magnitudes among all the engines during the whole mission period. Fig.(5.26) and Fig.(5.27) collect the information regarding the change in maximum and average thrust due to increasingly stringent angle constraints. Maximum and average thrust are computed among all the engines for the entire mission duration.

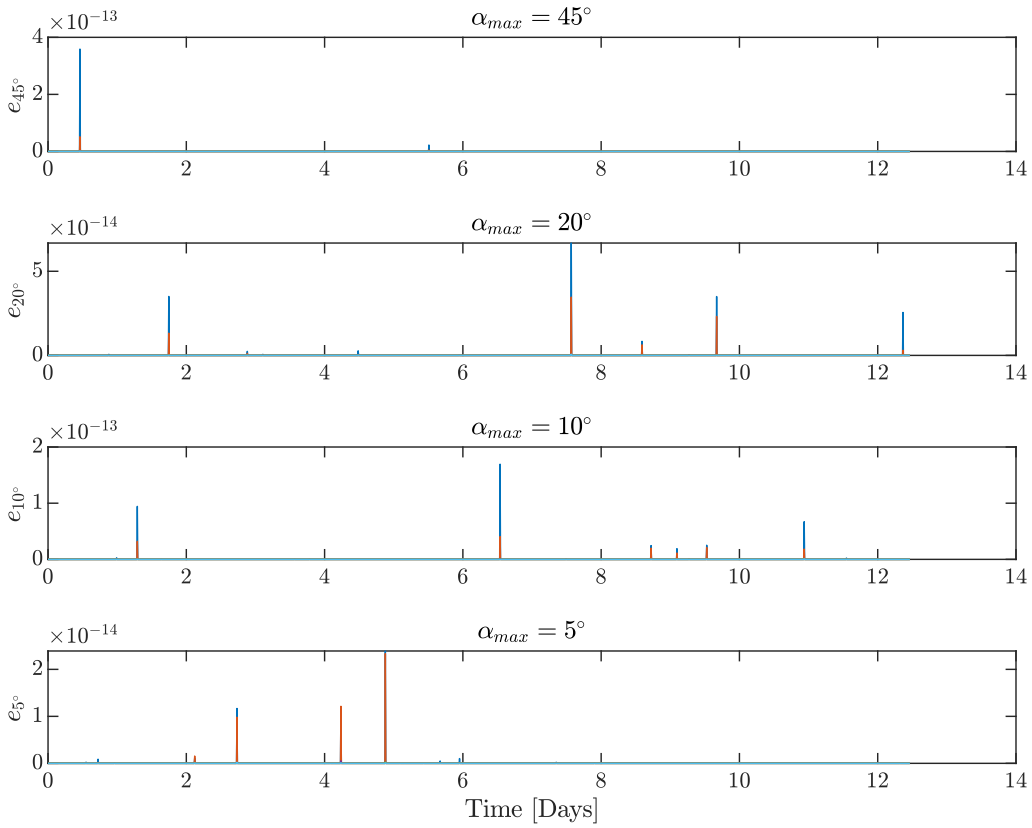

Figure 5.23: Control allocation mapping errors for Lyapunov mission case. Each subplot refers to a specific α_{max}.

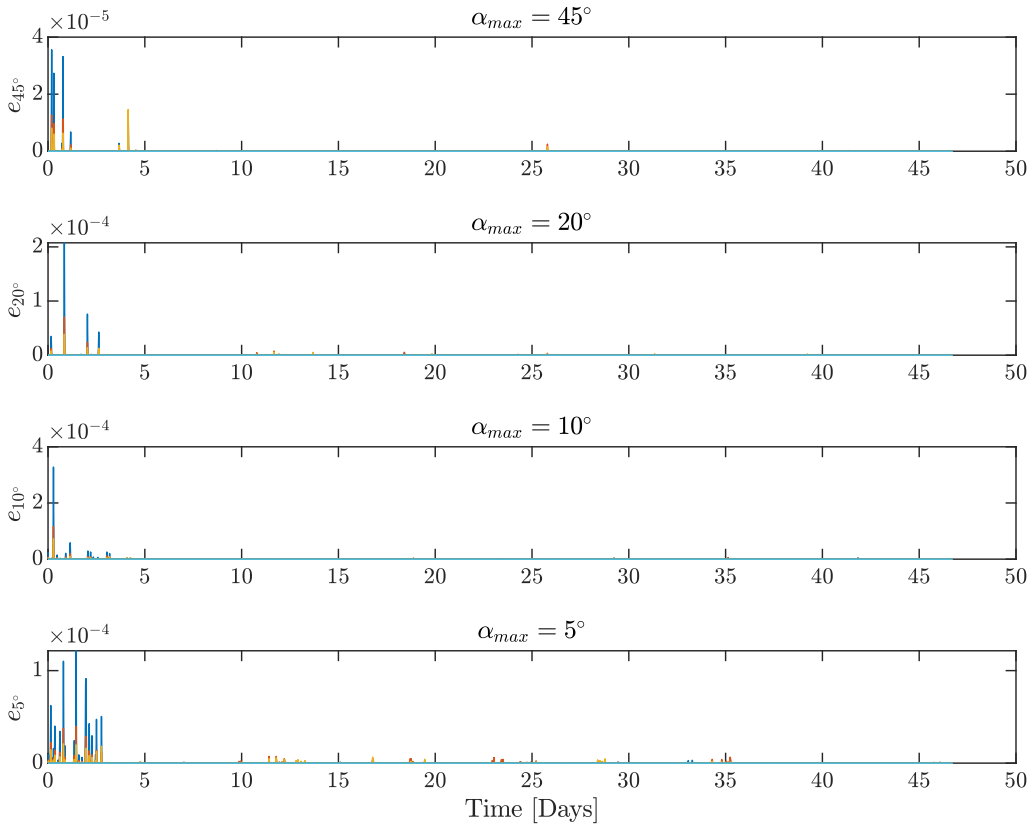

Figure 5.24: Control allocation mapping errors for Lissajous mission case. Each subplot refers to a specific α_{max}.

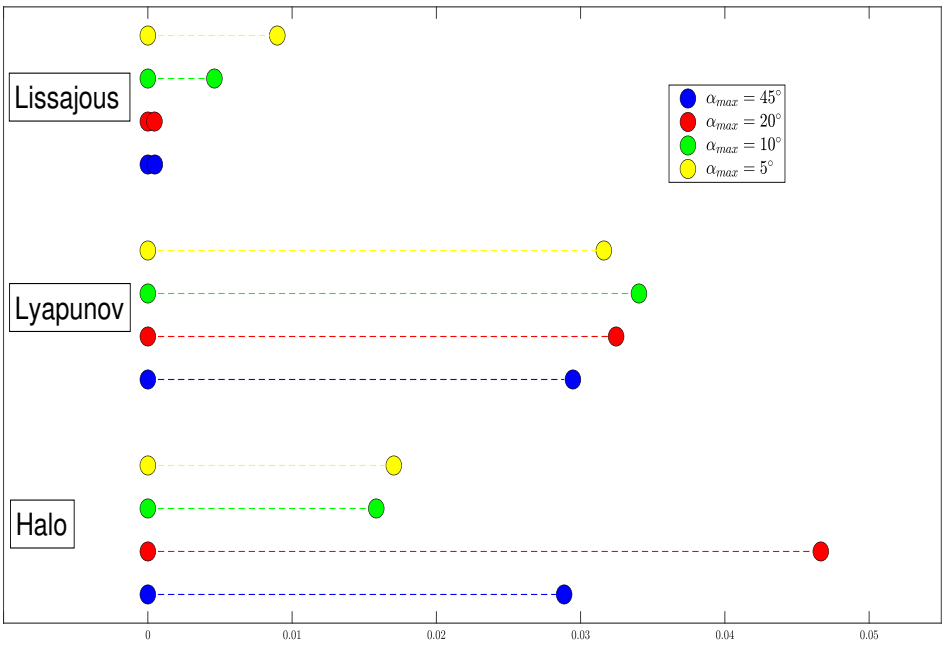

Figure 5.25: Required thrust ranges for the different missions. The colours refer to different gimbal angle constraints.

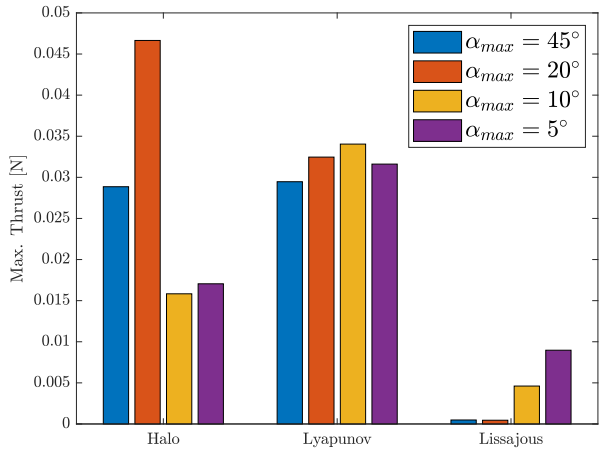

Figure 5.26: Maximum thrust provided during mission in Halo, Lyapunov and Lissajous orbits. The colours refer to different gimbal angle constraints.

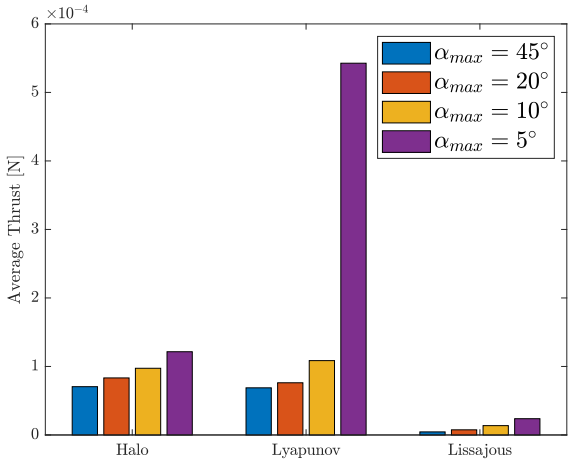

Figure 5.27: Average thrust provided during mission in Halo, Lyapunov and Lissajous orbits. The colours refer to different gimbal angle constraints.

Fig.(5.22) to Fig.(5.24) confirms the validity of the procedure for Halo and Lyapunov cases. The mapping errors are way below the noise values used in the high-level motion control design to simulate control execution errors; it is thus possible to conclude that station-keeping, attitude control and allocation strategies are capable of successfully control the spacecraft during its mission, both with unconstrained gimbals, both with constrained ones. Unfortunately, as far as the Lissajous case is concerned, huge mapping errors are produced specially during the first part of the mission. Those errors are several order of magnitude more significant with respect to the noise accounted in Chapter 3 and Chapter 4. This would probably bring the satellite to diverge from the nominal orbit as well as from the desired attitude. In order to asses if the methodology proposed in this work is be able to accommodate such errors, a second iteration should be carried out with the mapping errors inserted as disturbances in the high-level motion control algorithms, but it is out of the scope of the project.

Nevertheless, Fig.(5.25) to Fig.(5.27) point out some important features. As it was expected, the average thrust required increases as the angle constrains become tighter and tighter, for all the mission orbits. In particular, the Lyapunov case suffers a dramatic rise in the value of average thrust once gimbals are limited to an opening angle of $\alpha_{max} = 5°$.

Since the maximum thrust is not affected by such a peak, it is possible to affirm that an important performance degradation occurs in terms of fuel consumption; in fact, in order to match the commanded virtual inputs, the propulsion system is required to work almost five time more intensively with respect to the cases with looser constraints. Halo and Lissajous orbits anyway do not present such a drastic change in performance. Moreover the average thrust in the Lissajous case is expected to be higher in magnitude compared to the other orbits (because Lissajous orbits are analytically computed, without adopting any numerical correction scheme), but it is not the case. The most plausible cause of this evidence is that the control process is not able to achieve the required control effort, especially at the mission beginning, where the influence of initial errors is significant; the engines do not work at full power which is then reflected in the values of the average thrust, causing also significant mapping errors to occur. It is worth noticing also how, in the Halo case, the reduction of control freedom pushes the control allocation algorithm to exploit more equally the engines; although the maximum thrust recorded for $\alpha_{max} = 10°$ and $\alpha_{max} = 5°$ is decisively less than for the other cases, the average thrust values are higher. It means that the allocation procedure tends to share more equally the required control work among the engines, more than focusing on a particular one to provide the bulk of the effort. The comparison between global average thrust levels of unconstrained and constrained cases confirms what is stated so far; the maximum thrust values are lower in the constrained that in the unconstrained case while the average thrust values remain almost unchanged. It is symptom of a change in resource exploitation by the control system. Shared effort is preferred to single bulk contribution, as it was in the unconstrained case.

Results for $\boldsymbol{\alpha_{max} = 10°}$

If in the unconstrained gimbal case, most of the thrust is provided at the very beginning of each mission in order to cancel out the effects of initial errors, in the present case generally significant peaks of thrust are requested throughout the entire mission. There is no more a net separation between a transient and a steady state region, thus a separate

analysis of them loses meaning.

- **Halo Orbit:**

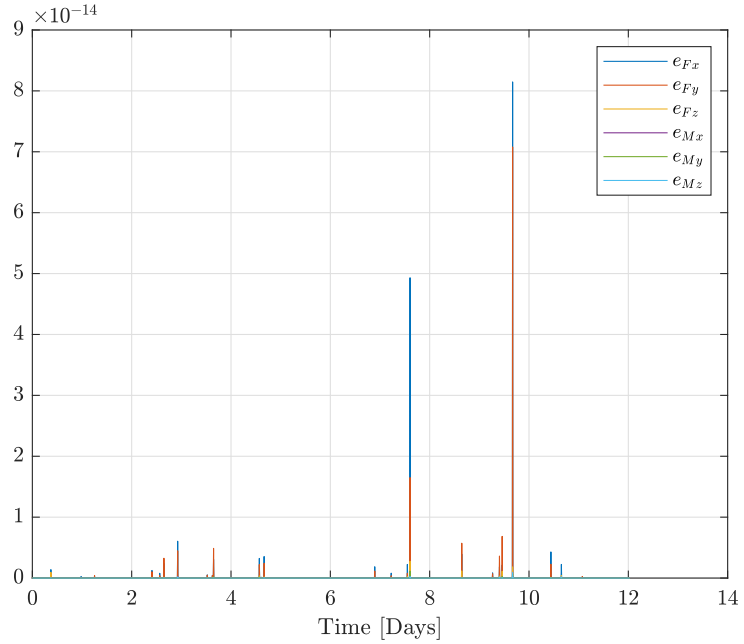

Figure 5.28: Constrained gimbal with $\alpha_{max} = 10°$ - Halo orbit: evolution of the mapping error: $\boldsymbol{e} = \boldsymbol{\tau_c} - \boldsymbol{\tau}$

.

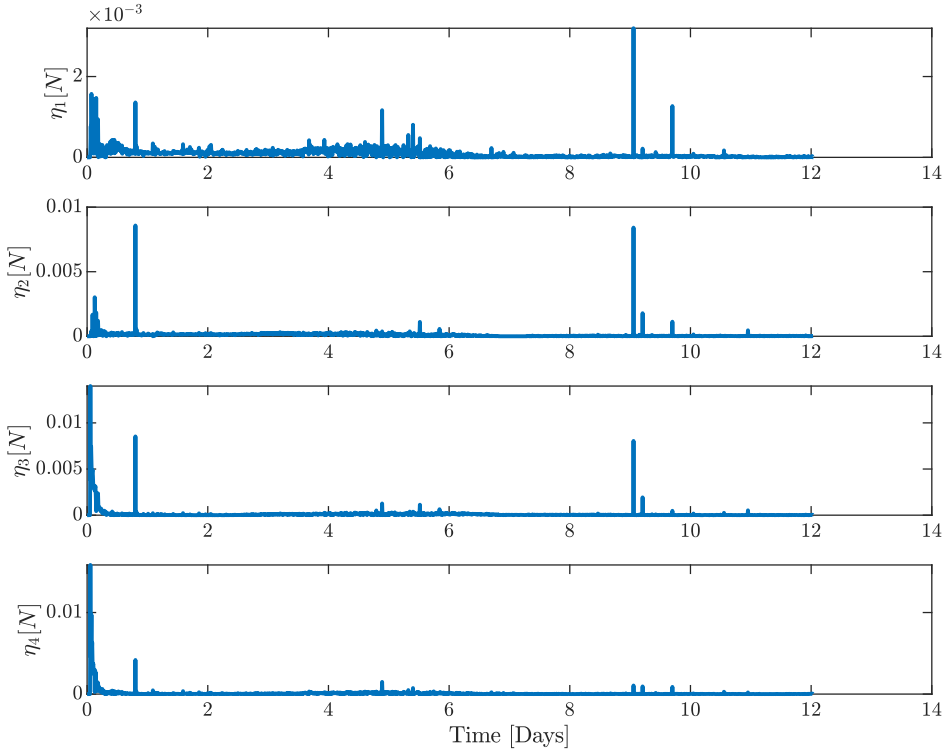

Figure 5.29: Constrained gimbal with $\alpha_{max} = 10°$ - Halo orbit: steady state behaviour of engine thrust levels.

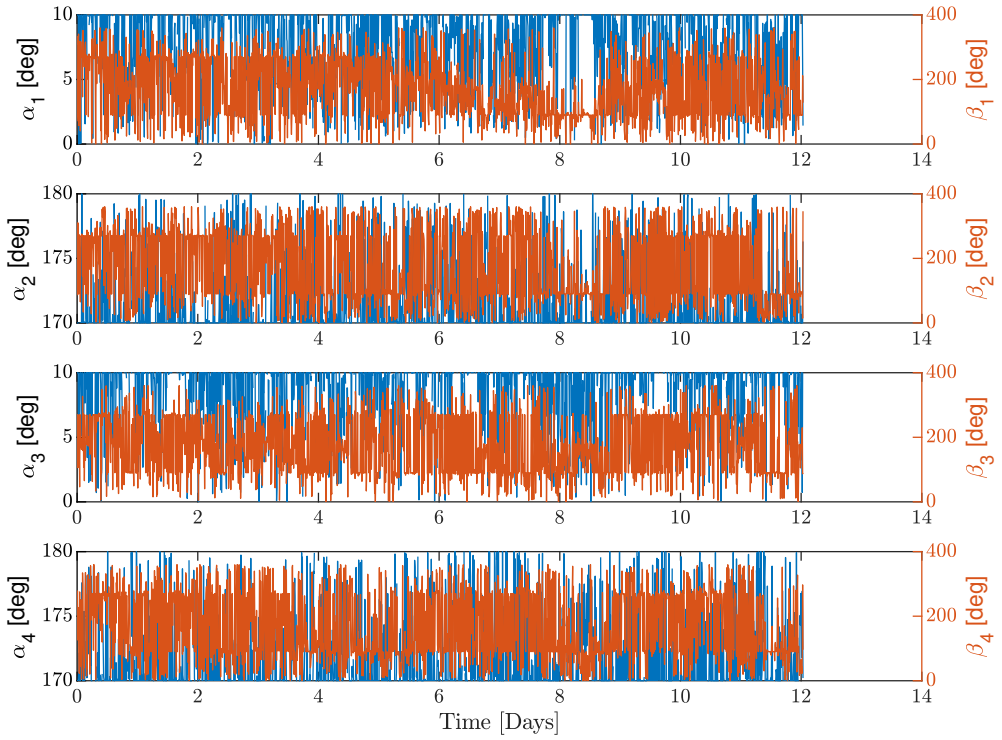

Figure 5.30: Constrained gimbal with $\alpha_{max} = 10°$ - Halo orbit: gimbal orientation during the mission. The right-hand side axis refers to the α angle, the left-hand side axis concerns the β angle. Conventions for α and β are shown in Section 5.1 Fig.(5.2) and Fig.(5.3).

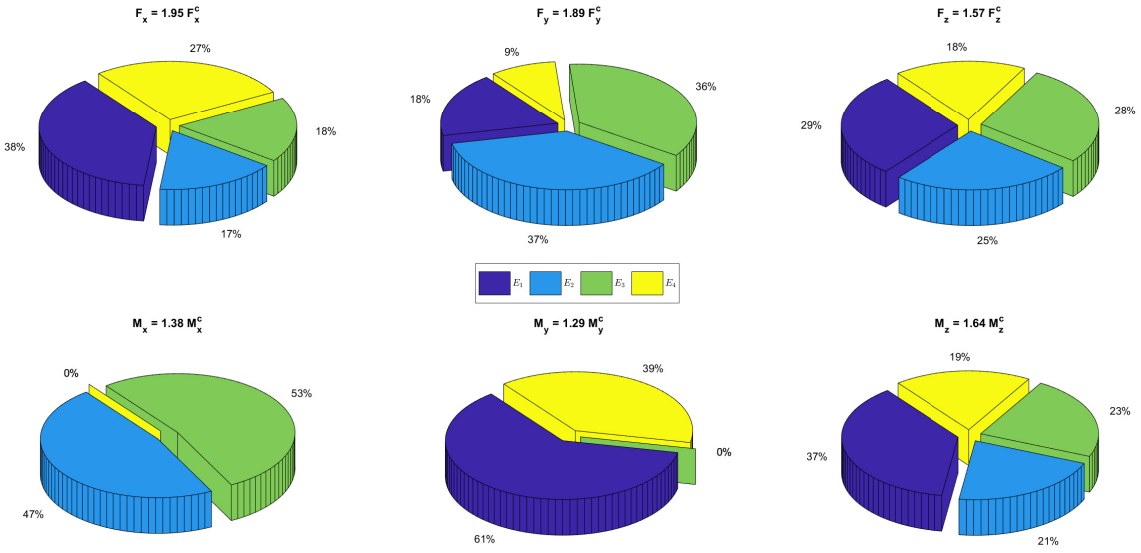

Figure 5.31: Constrained gimbal with $\alpha_{max} = 10°$ - Halo orbit: engine contributions to control inputs. The title of each pie chart represents the ration between the commanded ideal input (denoted by the superscript ^{c}) and the produced one in terms of absolute values. Ratios may exceed unity as only the absolute values of the contributions are considered, not their sign.

Max. Error	e_{Fx} = 8.14e-14
	e_{Fy} = 7.08e-14
	e_{Fz} = 2.75e-15
	e_{Mx} = 9.72e-16
	e_{My} = 1.15e-15
	e_{Mz} = 8.85e-16
Thrust Range	E_1 = [0.0032 - 9.21e-16] [N]
	E_2 = [0.0086 - 7.37e-17] [N]
	E_3 = [0.014 - 7.33e-15] [N]
	E_4 = [0.0158 - 6.81e-15] [N]
Average Thrust	E_1 = 8.4201e-05 [N]
	E_2 = 1.0182e-04 [N]
	E_3 = 1.1065e-04 [N]
	E_4 = 9.2767e-05 [N]
Global Av. Thrust	9.7359e-05 [N]
Global Max. Err	8.14e-14
Max. Thrust	T_{MAX} = 0.0158 [N]

Table 5.5: Constrained gimbal angle α_{max}, Halo orbit case - control allocation main results.

The error analysis presented in Fig.(5.28) proves the validity of the method. The control allocation procedure, and the high-level motion control, are perfectly capable of control the spacecraft in Halo orbit around a collinear libration point. As stated previously, the control effort is more equally shared among all the engines; there is no preponderant contribution of a particular thruster in any of the control degrees of freedom, as it is shown in Fig.(5.31). In the present case, engine E1 leaves the marginal role it appears to assume in the unconstrained case in favour of a central one in almost all the control degrees, together with all the other engines. It is worth noticing also how gimbal orientations tend to cover more completely

the allowable direction space with respect to the unconstrained case, where the thrust vectoring control is more locked to particular positions. As it is expected, significant cancellations affect the spacecraft control. All the ratios between the global produced forces or moments and the requested ones deviate from unity; it means that in order to produce the commanded virtual input engines provide a global contribution which exceeds the nominal request of about the 50%, for the present case, which may also get close to 100% for F_x and F_y. Oppositely, control DOFs which can be achieved by a specific couple of actuators, i.e. M_x and M_y, appear to be provided in a more efficient way.

Tab.(5.5) summarises the results.

- **Lyapunov Orbit:**

  The control system is successfully capable of commanding the spacecraft also in the case of the nominal Lyapunov trajectory selected for the project. It presents the same features already highlighted for the Halo case. The engines are requested to work in a more cooperative manner with respect to unconstrained angle scenario, as it can arise from Fig.(5.35). Moreover the gimbal mechanisms span completely all the directions at their disposal remaining confined inside the respective cones having $\alpha_max = 10°$. Also in the present case the control effort is sensibly higher with respect to the required one. Cancellation evidences appear in the control of F_x and F_y, where it is provided almost more than the double required force. Contrary, the control in M_x and M_y is achieved in a more efficient way, as the ratios in Fig.(5.35) remain close to unity.

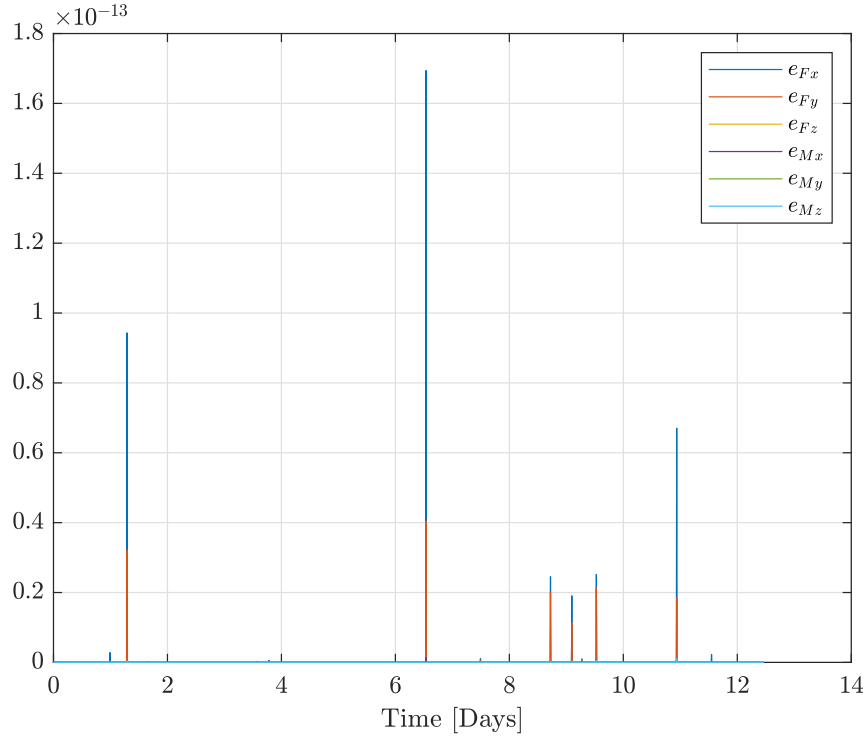

Figure 5.32: Constrained gimbal with $\alpha_{max} = 10°$ - Lyapunov orbit: evolution of the mapping error: $\boldsymbol{e} = \boldsymbol{\tau_c} - \boldsymbol{\tau}$

.

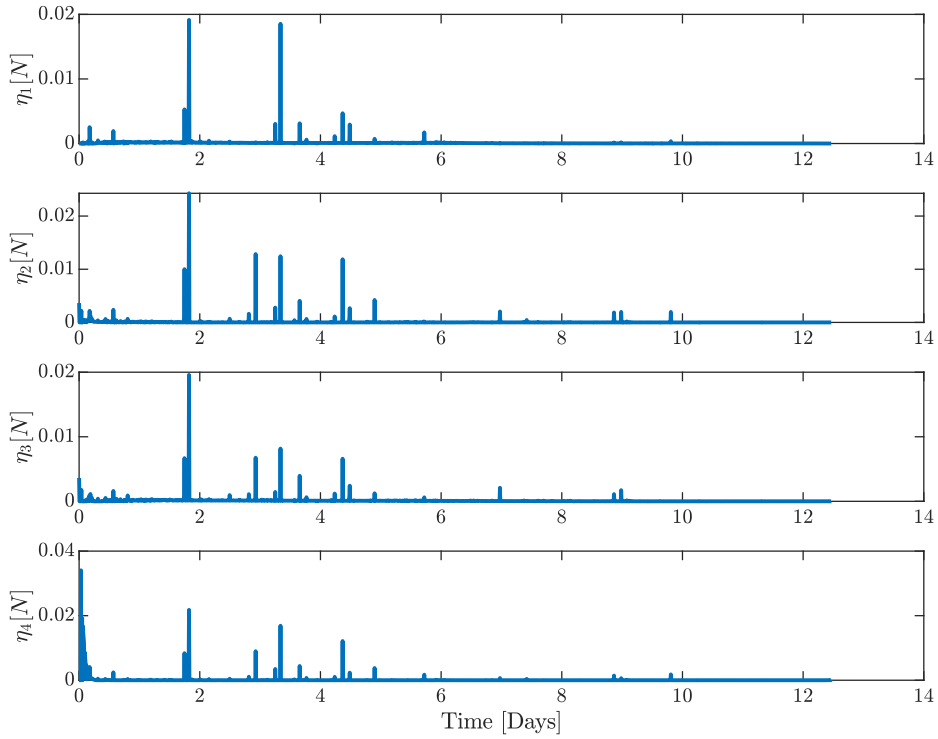

Figure 5.33: Constrained gimbal with $\alpha_{max} = 10°$ - Lyapunov orbit: steady state behaviour of engine thrust levels.

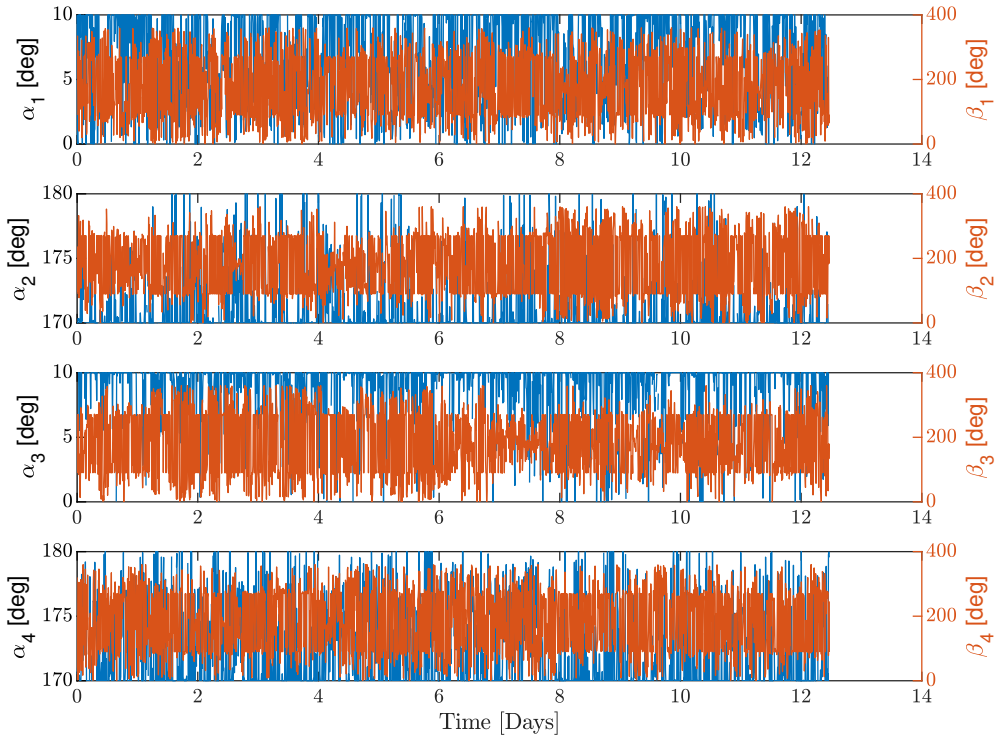

Figure 5.34: Constrained gimbal with $\alpha_{max} = 10°$ - Lyapunov orbit: gimbal orientation during the mission. The right-hand side axis refers to the α angle, the left-hand side axis concerns the β angle. Conventions for α and β are shown in Section 5.1 Fig.(5.2) and Fig.(5.3).

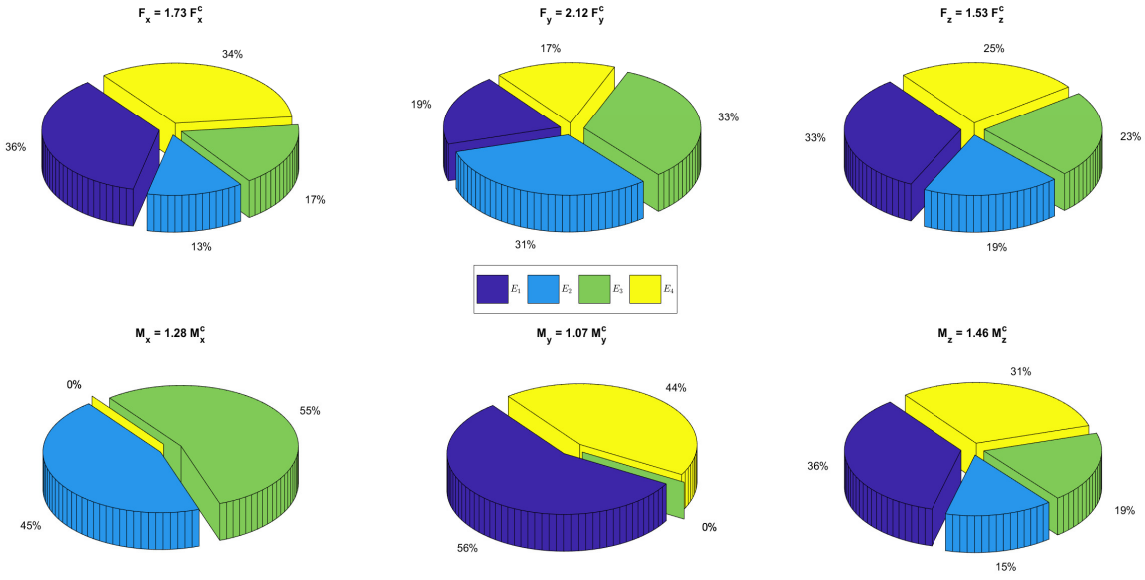

Figure 5.35: Constrained gimbal with $\alpha_{max} = 10°$ - Lyapunov orbit: engine contributions to control inputs. The title of each pie chart represents the ration between the commanded ideal input (denoted by the superscript ^{c}) and the produced one in terms of absolute values. Ratios may exceed unity as only the absolute values of the contributions are considered, not their sign.

Tab.(5.6) summarises the results.

Max. Error	e_{Fx} = 1.69e-13
	e_{Fy} = 4.04e-14
	e_{Fz} = 3.20e-18
	e_{Mx} = 1.39e-15
	e_{My} = 8.86e-16
	e_{Mz} = 1.02e-15
Thrust Range	E_1 = [0.0191 - 8.28e-16] [N]
	E_2 = [0.0243 - 2.41e-15] [N]
	E_3 = [0.0196 - 1.03e-14] [N]
	E_4 = [0.0340 - 1.39e-18] [N]
Average Thrust	E_1 = 1.0386e-04 [N]
	E_2 = 8.1969e-05 [N]
	E_3 = 1.0519e-04 [N]
	E_4 = 1.4310e-04 [N]
Global Av. Thrust	1.0853e-04 [N]
Global Max. Err	1.69e-13
Max. Thrust	T_{MAX} = 0.0340 [N]

Table 5.6: Constrained gimbal angle α_{max}, Lyapunov orbit case - control allocation main results.

- **Lissajous Orbit:**

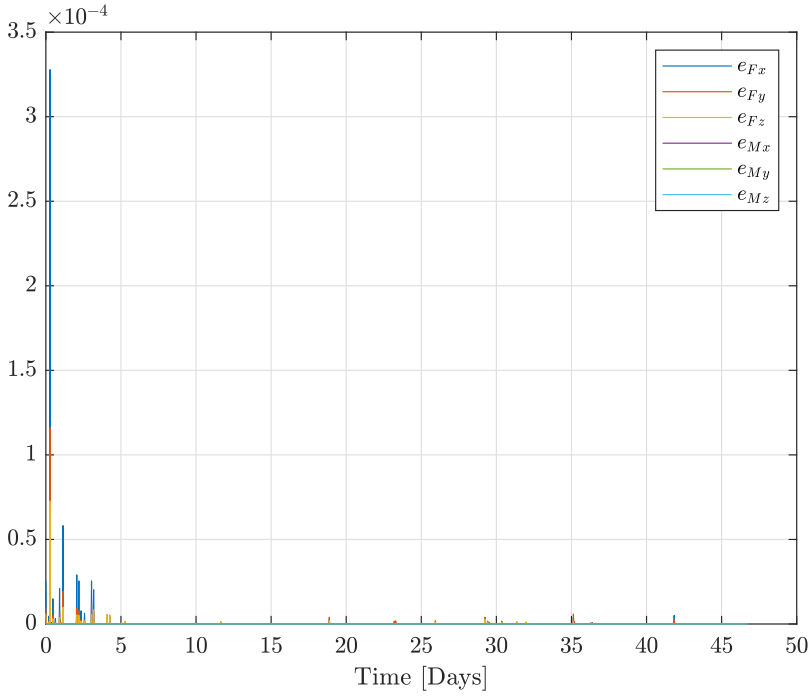

Figure 5.36: Constrained gimbal with $\alpha_{max} = 10°$ - Lissajous orbit: evolution of the mapping error: $\boldsymbol{e} = \boldsymbol{\tau_c} - \boldsymbol{\tau}$

.

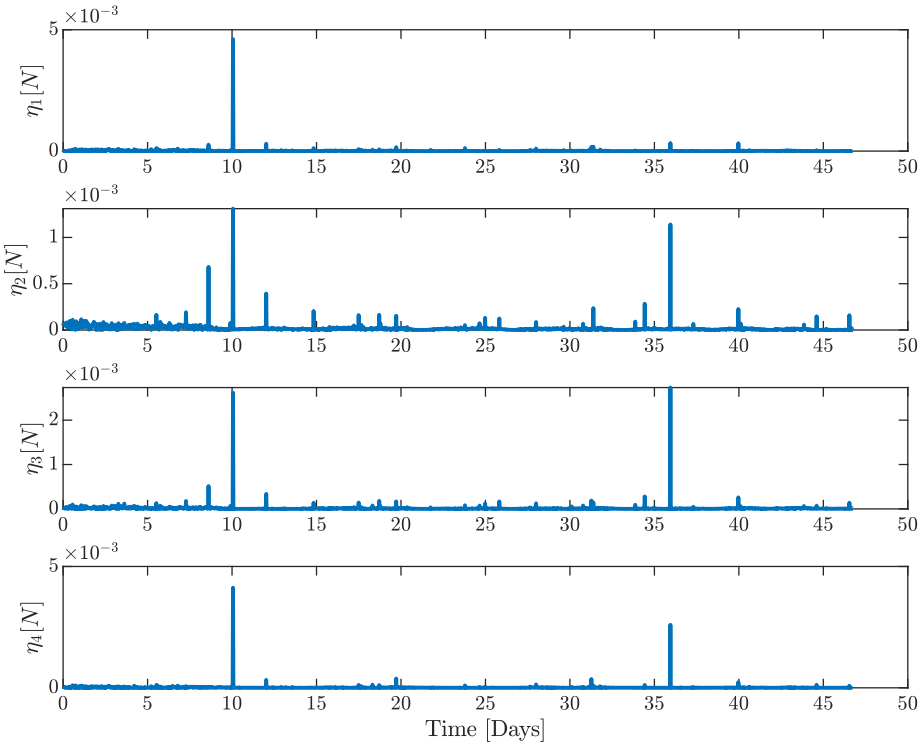

Figure 5.37: Constrained gimbal with $\alpha_{max} = 10°$ - Lissajous orbit: steady state behaviour of engine thrust levels.

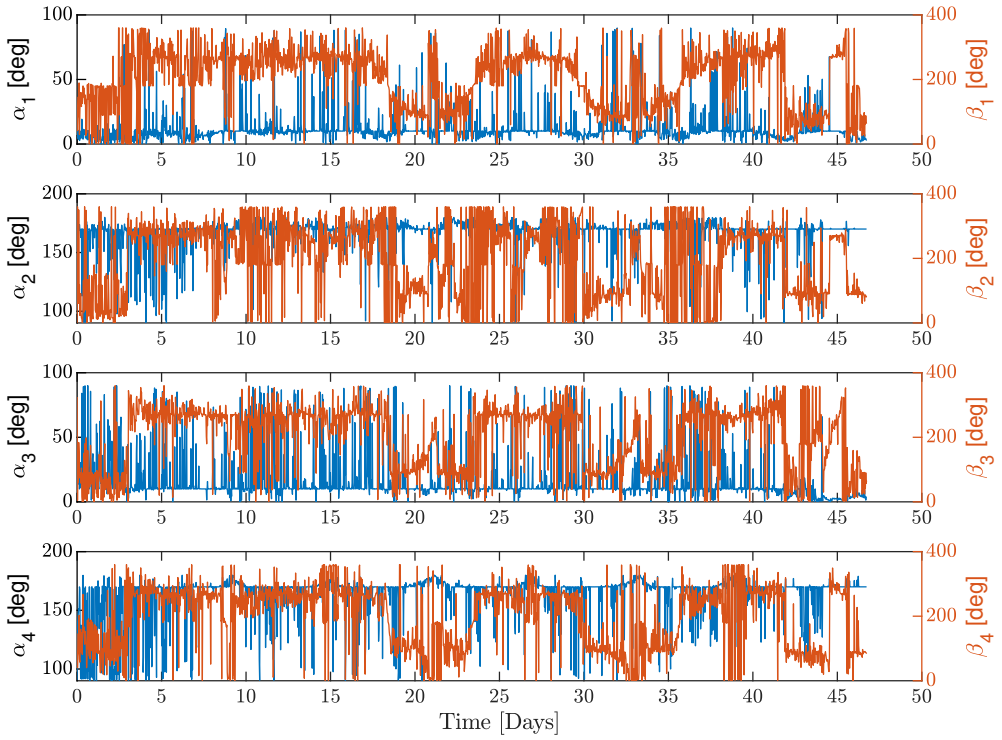

Figure 5.38: Constrained gimbal with $\alpha_{max} = 10°$ - Lissajous orbit: gimbal orientation during the mission. The right-hand side axis refers to the α angle, the left-hand side axis concerns the β angle. Conventions for α and β are shown in Section 5.1 Fig.(5.2) and Fig.(5.3).

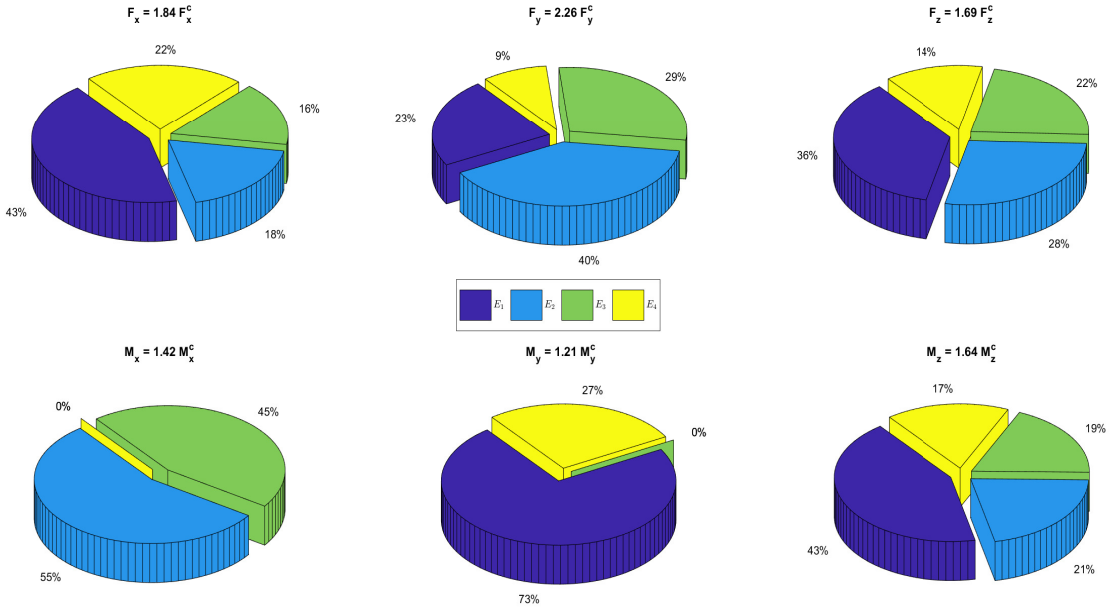

Figure 5.39: Constrained gimbal with $\alpha_{max} = 10°$ - Lissajous orbit: engine contributions to control inputs. The title of each pie chart represents the ration between the commanded ideal input (denoted by the superscript ^{c}) and the produced one in terms of absolute values. Ratios may exceed unity as only the absolute values of the contributions are considered, not their sign.

In the Lissajous case the control allocation procedure fails to produce satisfactory results. The mapping errors at the beginning of the mission reach non-negligible values requiring a second iteration of the entire process to asses the method to be capable of handling them, but this is out of the scope of the project. Moreover, the control system is unable to find appropriate directions withing the allowable range in order to control the spacecraft; the optimisation algorithm converge to unfeasible solutions whatever starting point is given as initial guess. The only reasonable justification which could explain such behaviour relies on the intrinsic properties of the Lissajous orbit; analytical approximation errors which are shown in Chapter 3 and Chapter 4 to drive the control system to perform stronger control actions, also lead the allocation procedure to the impossibility of finding a proper solution to accommodate the control input requests. The procedure is definitely not validated for the Lissajous nominal orbit selected in the work. For this reason no significant results may be extrapolated from the Lissajous case analysis.

5.4 Thruster selection

The main goal of this section is to carry out an exhaustive analysis of electric propulsion technologies, currently available or under development, on which to base a preliminary selection of the thrusters considering the results of Chapter 5. Firstly an overview of electrical micropropulsion systems is presented in order to figure out the main drivers of the selection. The most important features characterising each type of engine are exposed as well as the technological peculiarities, advantages and disadvantages.
Compared with conventional propulsion systems, micropropulsion systems have the following two characteristics in general.

1. The thrust and impulse range covered is relatively small with order of magitudes of mN-μN and mNs-μNs.

2. Volume and weight are relatively small. Generally, weight is in kilograms or lower orders of magnitude.

The propulsion system is actually a mechanical system which turns different forms of energy into kinetic energy. As regards electric propulsion, it uses the means of electric heating, electromagnetic, or electrostatic to accelerate the propellant, and emerging with a high-velocity jet-flow. Miniaturised electric propulsion system often are referred as *Micro Electro-Mechanical Systems (MEMS)* technologies. There is a wide range of different MEMS propulsion units which exploit different principles to produce a net force.

- **Pulsed Plasma Thruster (PPT)**:

  The PPT is one of the earliest researched electric thrusters. In the 1950s pulsed plasma thruster technology began to be developed and applied. In 1964 in the Soviet Zond-2 satellite, it was used in flight tests for the first time [37]. Because it relies on an electromagnetic field to accelerate the plasma to produce thrust, it belongs more specifically to the category of electromagnetic thruster. The working principle of PPT is that a circuit charges the capacitor to a sufficiently high voltage which in turn discharges between the cathode and the anode rod sleeve. It generates high temperatures which heat the exposed portion of the propellant to make it decompose. Subsequently the decomposed gas is ionized and the joint action of its own magnetic and dynamic pressure produce the gas acceleration towards outside which results in a net thrust on the spacecraft. Tab.(5.7) collects the performance of the most advanced micro PPT prototypes on the market [49] [35].

Properties	**DawgStar PPT**	**μPPT at AFRL**
Thrust form	Pulse	Pulse
Thrust [μN]	< 112	10
I_{sp} [s]	500	-
MIP [Ns]	5.6e-5	-
Thrust to Power ratio [μN/W]	8.3	-
Mass [Kg]	3.95	< 0.1

Table 5.7: PPT prototypes performance. I_{sp} stands for *Specific Impulse* and MIP stands for *Minimum Impulse Bit*.

The main advantages and drawbacks of this technology are [5]:

1. **Advantages:** firstly, it is able to provide relatively high specific impulse. Moreover it does not require for high-pressure reservoirs and cryogenic devices, which simplifies the system architecture and reduce the occupied volume.
2. **Disadvantages:** the propellant get frequently contaminated and it is not consumed uniformly. Moreover the system is capable of sustain low working frequencies and, though it is characterised by high specific impulse, the amount of energy required to carry out the process is substantial.

- **Field Emission Electric Propulsion (FEEP)**:

FEEP is an electrostatic electric propulsion, which relys on a high-voltage electrostatic field accelerating charged ions to produce thrust. At present, no information is available about FEEP for flight tests [49]. Solid propellant is stored in the transmitter storage chamber until needed, when the reservoir chamber is heated to liquefy the propellant typically low melting point metals. The liquid metal moves then to the emitters where the presence of an accelerating electric field causes the metal to win the surface tension and accelerate. Tab.(5.8) collects the theoretic performances of FEEP according to [35]

Properties	**FEEP (Cesium)**	**FEEP (Indium)**
Thrust form	Continuous	Continuous
Thrust [μN]	0.1-1200	1-100
I_{sp} [s]	7000-11000	10000
MIP [Ns]	1e-9	$< 1e-8$
Thrust to Power ratio [μN/W]	16-20	15
Mass [Kg]	2.2	2.5

Table 5.8: PPT prototypes performance. I_{sp} stands for *Specific Impulse* and MIP stands for *Minimum Impulse Bit*.

The main disadvantage of FEEP for small satellite applications is that it requires an excessively high operating voltage.

- **Colloid Thruster**:

  The colloid thruster is another electric propulsion system that was studied earlier, and is categorized as electrostatic. However, because of its higher operating voltage and the huge volume of the system needed to obtain a large advance, its study was not extensive. Recently, with the development of technology, colloid technologies arouse fervent attention in the scientific community once again. It works similar to FEEP and also uses high voltage to accelerate charged particles to produce thrust. Differently from the latter, colloid thrusters use more conductive liquid as working fluid.

  Tab.(5.9) summarises the typical colloid thruster performance.

Properties	**Performances**
Thrust form	Continuous
Thrust [μN]	0.1-1200
I_{sp} [s]	7000-11000
MIP [Ns]	1e-9
Thrust to Power ratio [μN/W]	16-20
Mass [Kg]	2.2

Table 5.9: Colloid thruster typical performance. I_{sp} stands for *Specific Impulse* and MIP stands for *Minimum Impulse Bit*.

  Many research activities have been carried out in the last decade regarding colloid thruster systems [48] [30] [33]. However, the problematic high voltage requirement still represent a big challenge for practical applications.

- **Hall Thruster:**

  Hall thrusters belong to electrostatic electric propulsion. They have been widely researched in Russia, Europe, Japan, and the United States. Their technologies and applications are mature among electric propulsions. The basic structure of a Hall thruster is composed of an annular solenoid, injector anode, a plasma chamber, and a cathode. Electrons emitted from the cathode initially move to the anode in

the electric field strength. They are captured during movement by a magnetic field in the plasma chamber. Propellant gas (usually xenon) is injected from the anode to plasma chamber, where it is ionized due to the effect of the electrons. Once the anode gas is ionized, it will be accelerated and fly out in the electric field, producing thrust. Typical Hall thruster performance parameters are listed in Tab.(5.10) [49].

Properties	**Performances**
Thrust form	Continuous
Thrust [μN]	$> 4e-3$
I_{sp} [s]	> 1200
MIP [Ns]	1e-3
Thrust to Power ratio [μN/W]	60
Mass [Kg]	0.9

Table 5.10: Hall thruster typical performance. I_{sp} stands for *Specific Impulse* and MIP stands for *Minimum Impulse Bit*.

Available hall thrusters on the market unfortunately present a severe limitations: the thrust range is way higher the theoretic value reported in Tab.(5.10) which makes it a still unripe technology for CubeSat application. However comparing the *Technology Readiness Level* in conjunction with engine weight, power demand and I_{sp}, with the other micropropulsion technologies, hall thrusters appears as the ideal candidate for nano-satellite propulsion in the close future.

To sum up everything, it is possible to conclude that:
The PPT system has a simple structure, and is low cost with good stability. Especially, PPT system technology is relatively mature, has found many practical applications, and has worked reliably. Also, the PPT system has a higher specific impulse, and can provide small and repeatable pulse impulse. However, the main drawbacks are that the mass of PPT systems is generally large, the thrust to power ratio is low and it is affected generally by plume contamination problems. In addition, the working principles of PPT

are complex requiring a perfect tuning of electromagnetic and electric effects which need further in-depth analysis.

FEEP has a high specific impulse, small thrust, and it can provide a slight pulse impulse. Although there is no formal FEEP propulsion system used in space flight test, very similar technology (like the indium ion emission propulsion on MIR, GEOTAIL and EQUATOR-S satellites) have been proven for space missions. FEEP's drawback is that its pushing power ratio is low, and a high operating voltage. It also has the problem of pollution plumes.

The colloid thruster system turns out to be very suitable for small satellites propulsion. It is simple to design, resulting in low cost and high stability. It uses an inert propellant which is a great advantage for long-term tasks. It is promoted further because it can provide a wide range of thrust and specific impulses. Its drawback is that it has a low ratio of pushing power with higher operation voltage than FEEP. Moreover, as the other technologies, it is affected by pollution plume problems.

Finally, Hall thruster advantages include its higher specific impulse and high thrust power ratio. Meanwhile, the Hall thruster is the most mature system of the electric thruster systems. Differently for the other thruster types, it has lower risk of a contamination plume. Its disadvantage is the poor quality and the large, complex structure [49].

All the technologies presented so far are still under development, so it is not possible to select a particular engine for the missions analysed in this project. Moreover, nowadays technologies are far to respect the constraints imposed by the results of Chapter 3 Chapter 4.3 and Chapter 5. The thrust range results request fine thrust tuning spanning from μN to mN, in conjunction with high impulse bit accuracy. Among the MEMS technologies, whose properties are listed from Tab.(5.7) to Tab(5.10), pulsed plasma thrusters seem to be the least suitable solution to be applied to the types of missions proposed. Conversely both FEEP, Colloid and Hall thrusters present interesting properties: the first two are characterised by astonishing thrust ranges supported by low MIP and incredibly high specific impulses. However the drawbacks previously listed drive the interest upon the hall thrusters. Definitely the combination of performance, technology readiness level and

practical features makes the hall thruster the preferred choice to be implemented for the station-keeping attitude control of a stand-alone CubeSat in orbit around collinear libration points.

Chapter 6

Conclusions

The design of the *High-Level Motion Control laws* and *Control Allocation procedures* is carried out and tested on the orbits selected as representative for the three main categories of orbits around collinear libration points: *Halo orbits*, *Lyapunov orbits* and *Lissajous orbits*. The decoupled station-keeping and attitude controls produce satisfactory results maintaining the spacecraft position and orientation on the desired track in spite of the presence of external disturbances. Without considering the coupling of the two control systems, which emerges from the adoption of only four engines for all control purposes, it is possible to derive the ideal control forces and moments to control the spacecraft during its mission without significant issues. However, the problematic is just submitted to the *Control Allocation procedure*. It is at this level that the commanded virtual forces and moments have to be matched simultaneously by a proper coordination of thrust magnitudes and orientations. An optimisation process has to be carried out in order to find the best solution in terms of mapping error production and fuel consumption.

The results coming from this type of approach are satisfactory and suggest a more in-depth development of the theme. This approach is capable of governing the spacecraft properly in two out of three cases, i.e. in the Halo case and Lyapunov case. Both station-keeping and attitude control objectives are achieved in an efficient way; the propulsion system composed of just four actuators is adequately exploited to face the multi-tasking role of positioning and attitude control and resistance to external disturbances. Both in the ideal case where gimbal mechanisms are free to span the entire available space,

both in the case where practical limitations concerning gimbal orientations are taken into account, the control system is capable of controlling the spacecraft in its journey. On the contrary for the selected Lissajous orbit, the control allocation algorithm is not able to coordinate the engines to match the control requirements once gimbals are limited to maximum opening angles. The reasons for this failure are mainly dictated by the intrinsic properties of the Lissajous orbit definition. In this project Lissajous trajectories are computed analytically by linearising the CR3BP equations of motion around the libration points. Differently from Halo and Lyapunov orbits, no numerical correction schemes are applied to compute the desired Lissajous trajectory. It leads to the presence of non-negligible approximation errors which requires a different level of control effort. In the context of CR3BP, the bulk of the control effort for Halo and Lyapunov trajectories is mainly condensed at the spacecraft orbit insertion in order to deal with the presence of initial errors; once the insertion transient ends, required control input magnitudes drastically drop to relatively small values. In the Lissajous case instead, linearisation errors force the control system to intervene decisively throughout the entire mission. The overall required force do not stick around precise directions but keep on changing its orientation; this kind of situation is absolutely inadequate for the control allocation procedure which tries to match a continuous changing force with a more steady, overall required moment. The excess of freedom offered in the ideal case where gimbals are free to move, manages to compensate the unsteady behaviour of the required control force; once gimbals get constrained, the control system fails to achieve its goals.

Tab.(6.1) summarises the achievements of the proposed approach to the coupling of station-keeping and attitude control for an under-actuated CubeSat in orbit around libration points.

Orbit	**Unconstrained gimbals**	**Constrained gimbals**
Halo	✓	✓
Lyapunov	✓	✓
Lissajous	✓	×

Table 6.1: Procedure achievements.

The approach appears to be very efficient for preliminary analyses. The station-keeping and the attitude controls are designed separately and than integrated lately by means of the allocation procedure. There is no constraint on the selection of the high-level control algorithms whose performances may be analysed separately. This feature grants design freedom, which is essential during the early phases of mission developments. Moreover, since the allocation algorithm is completely detached from high-level motion control procedures, this approach enables the designer to analyse many different combinations of control techniques to figure out the most suitable for its particular mission. The method turns out to be extremely general and it can be easily transposed to other typologies of missions. Obviously orbit selection directly impacts on virtual control requirements but since the allocation technique is independent from the high-level control formulation, there is no limit to its applicability. Moreover the optimisation algorithms used during the allocation phase may account for many different constraints. In the context of this work it is followed a top-down approach: the outputs of the control system design have served as drivers for the thruster selection. For this reason constrains on thrust magnitude are omitted in order to find out the nominal thrust envelope of the mission. However if the choice of the engine is already known a priori, the control allocation procedure is able to account for them with any practical issue. Obviously, a major drawback of the approach is that during the high-level motion control design no information is provided about the engines limitations, which can be accounted for only during the last phase. Unfeasible requirements are not noticed until the control allocation procedure takes place, as it is happened for the constrained gimbal case of Lissajous trajectory. It is left up to the engineer experience to recognise since the beginning if the techniques adopted in the high-level phase produce traces which can be subsequently matched by the propulsion system via control allocation optimisation.

With regard to the techniques adopted in this work some important considerations can be drawn. First of all, it is clear the paramount importance of numerical correction schemes for orbit determination. The CR3BP equations of motion are extremely sensitive to errors: small perturbations of the solution may cause large errors after few orbit

Table 6.2: Main advantages and drawback of the approach proposed in the project.

Advantages	**Disadvantages**
1) Generality: the approach can be extended to whatever space mission. The high-level motion control and the allocation procedure may be designed to achieve the mission requirements, no matter what kind of mission it is. 2) Design freedom: the four core parts of the procedure, i.e. orbit design, station-keeping control law, attitude control law and control allocation are not related by the problem formulation. Their structures are independent of each other	1) Top-Down flow: there is no information about the influence that lower level constraints have on higher level results. 2) On-line implementation: the method requires the knowledge of the positions occupied by the spacecraft in its journey. Since this is a requisite, an on-line implementation for on-board operation is not feasible.

revolutions. The single shooting technique used to compute Halo and Lyapunov orbits in this project works well for limited simulation periods; the cumulative numerical error due to machine accuracy leads to orbit divergence after approximately 5-6 orbit revolutions. For longer simulation *Multiple Shooting Techniques* have to be adopted. Orbits computed analytically bring to unsatisfactory results. Then, the control algorithms for station-keeping and attitude control are tuned in order to respond quickly and resolutely to initial errors; this causes a strong control effort condensed in a small amount of time. The satellite is rapidly brought back to its nominal behaviour, ready to perform the task it is designed for. It would be interesting to better analyse how a looser control would impact on the propulsion system and on the mission concept of operations. It has to be noticed that, since the spacecraft nominal attitude is determined by the knowledge of the future actual trajectory of the spacecraft, the method do not work as an on-line control procedure. The procedure applicability is restricted to design purposes, and this represents the second major disadvantage of the methodology. Tab.(6.2) is intended to give a briefly overview of the main advantages and disadvantages of the proposed approach.

This project represent a preliminary step in the analysis of the control of under-actuated spacecrafts in orbit around collinear libration points. Further developments are required to properly characterise the performance of such kind of control. Above all, a failure tolerance analysis would be of fundamental importance to asses the robustness of the

method. Failure scenarios would have to consider both thruster failures both gimbal ones, as movable mechanical parts undergoing the harsh deep-space environment are easily prone to fails. Moreover, the adoption of more sophisticated control algorithms could increase the performance in terms of thruster exploitation, fuel consumption ad tightness of the control. From the consideration pointed out so far, the *Model Predictive Control (MPC)* appears as the ideal candidate to substitute the LQG algorithm used for the station-keeping. It would path the way also for a practical implementation on-board. Of great interest would be also the comparison of different optimisation algorithms for control allocation. It would be interesting to analyse how the propulsion system resources are coordinated differently by the different algorithms used. Finally,

Bibliography

[1] A., F. Deep Space nanosats – positioned for exponential growth. *Conference: 4S Symposium 2016* (2016).

[2] A. Rahmani, M. A. Jalaliy, S. H. P. OPTIMAL APPROACH TO HALO ORBIT CONTROL. *AIAA Guidance, Navigation, and Control Conference and Exhibit* (2003), 11–14.

[3] Anderson, B. D. *Optimal Control; Linear Quadratic Methods*. Prentice-Hall International.

[4] B., W. *Space Vehicle Dynamics and Control, 2nd Edition*. American Institute of Aeronautics and Astronautics, 1952.

[5] Bendong Liu, Xinrui Li, J. Y. G. G. Recent Advances in MEMS-Based Microthrusters. *Micromachines 10*, 818 (2002).

[6] Biggs J.D., Calvo A.R., T. F. Attitude Control for the LUMIO CubeSat in Deep Space. *Conference: 70th International Astronautical Congress* (2019).

[7] Bramanti C., B. D. Deep-space CubeSats: Thinking inside the box. *Astronomy & Geophysics 59*, 5 (2018), 5.24–5.30.

[8] Breakwell John V., B. J. V. The halo family of 3-dimensional periodic orbits in the Earth-Moon restricted 3-body problem. *Celestial Mechanics*, 20 (1979), 389–404.

[9] Breakwell John V., Kamel Ahmed A., R. M. J. Station-Keeping for a Translunar Communication Station. *Celestial Mechanics 10*, 3 (1974), 357–373.

[10] Brophy J.R., M. M. e. a. The Ion Propulsion System for Dawn.

[11] Cielaszyk, D., and Wie, B. New approach to halo orbit determination and control. *Journal of Guidance, Control, and Dynamics 19*, 2 (1996), 266–273.

[12] Curtis, H. D. *Orbital mechanics for engineer students - Third Edition*. Elsevier.

[13] D., P. A Monopropellant Milli-Newton Thruster System for Attitude Control of Nanosatellites.

[14] Doedel, Romanov, P. K. D. G.-V. V. Elemental Periodic Orbits Associated with the Libration Points in the Circular Restricted 3-Body Problem. *International Journal of Bifurcation and Chaos 17*, 8 (2007), 2625–2677.

[15] Domingo V., e. a. The SOHO Mission: An Overview. *Solar Physics 162*, 1-2 (1995), 1–37.

[16] Dunham D., F. R. Libration Point Missions, 1978 - 2002.

[17] Eismont N., e. a. RELICT 2 project: Scientific program and structure. *ESA SP-314* (1990), 99–104.

[18] E.L., S. On the Verge of an Astronomy CubeSat Revolution. *Nature Astronomy 2*, 5 (2018).

[19] Farquhar R.W., K. A. Quasi-Periodic Orbits About the Translunar Libration Point. *Celestial Mechanics 7*, 4 (1973), 458–473.

[20] Fossen J.I., J. T. Control allocation—A survey. *Automatica 49* (2013), 1087–1103.

[21] Ghorbani M., Hassani A, P. M. A Study of Spacecraft Reaction Thruster Configurations for Attitude Control System. *IEEE Aerospace and Electronic Systems Magazine 37*, 2 (2017).

[22] Howell, K. C., and Pernicka, H. J. Station-Keeping Method for Libration Point Trajectories. *Journal of Guidance, Control, and Dynamics 16*, 1 (1993), 151–159.

[23] J.R., B. NASA's Deep Space 1 ion engine (plenary). *Review of Scientific Instruments 73*, 2 (2002), 1071–1078.

[24] K. Nishiyama, S. Hosoda, K. U. R. T., and Kuninaka, H. Development and Testing of the Hayabusa2 Ion Engine System. *Joint Conference of 30th International Symposium on Space Technology and Science* (2015).

[25] Keeter, T. M. Station-keeping strategies for libration point orbits: Target point and floquet mode approaches. Master's thesis, School of Aeronautics and Astronautics, Purdue Univ., West Lafayette, 1994.

[26] Kolbeck J., K. J. e. a. Nano-Sat Scale Electric Propulsion for Attitude Control-Performance Analysis. *2019 IEEE Aerospace Conference* (2019).

[27] Kolbeck J., L. J. e. a. μCAT Micro-Propulsion Solution for Autonomous Mobile On-Orbit Diagnostic System. *Small Satellite Conference 2016* (2016).

[28] Maksim Shirobokov, Sergey Trofimov, M. O. Survey of station-keeping techniques for libration point orbits. *Guidance, Control, and Dynamics 40*, 5 (2017), 1085–1105.

[29] Markley F. L., C. J. L. *Fundamentals of Spacecraft Attitude Determination and Control*. Springer, 2014.

[30] Martinez-Sanchez, M.; de la Mora, J. G.-C. H. K. V. Research on colloid thrusters. *Proceedings of the 26th International Electric Propulsion Conference* (1999).

[31] NASA. Gimbal for Steering Propelled CubeSats - Fact Sheet.

[32] Nazari, M., A. W., and Butcher, E. A. Continuous Thrust Stationkeeping in Earth–Moon L1 Halo Orbits Based on LQR Control and Floquet Theory. *AAS/AIAA Astrodynamics Specialist Conference, AIAA Paper 2014-4140* (2014).

[33] Paine, M.; Gabriel, S. G.-C. H. K.-V. A micro-fabrication colloidal thruster array. *In Proceedings of the 37th AIAA Joint Propulsion Conference Exhibit* (2005).

[34] Passaro A., Gonzalez del Amo J., E. D. e. a. Flight Experience from the Smart-1 Electric Propulsion System.

[35] R. Leach, K. N. Discussion of micro-newton thruster requirements for a drag-free control system. *16th Annual/USU Conference on Small Satellites* (2002).

[36] Richardson, D. L. Analytic construction of periodic orbits about the collinear points. *Celestial Mechanics*, 22 (1980), 241–253.

[37] R.L. Burton, P. T. Pulsed plasma thruster. *Jet Propulsion Power 14*, 5 (1998), 716–735.

[38] R.W., F. Station-Keeping in the Vicinity of Collinear Libration Points with an Application to a Lunar Communications Problem. *AAS Science and Technology Series: Space Flight Mechanics Specialist Symposium 11* (1966), 519–535.

[39] S., Yu, X. S. B., and Man, Z. Continuous Finite-time Control for Robotic Manipulator with Terminal Sliding Mode. *Automatica 41*, 11 (2005), 1957–1964.

[40] Schoolcraft J., Klesh A., W. T. Interplanetary CubeSat Navigational Challenges. *International Symposium on Space Flight Dynamics* (2015).

[41] Schoolcraft J., Klesh A., W. T. MarCO: Interplanetary Mission Development on a CubeSat Scale. *SpaceOps Conferences* (2016).

[42] Slotine J. E., L. W. *Applied Nonlinear Control*. Prentice Hall.

[43] Stone E. C., e. a. The Advanced Composition Explorer. *Space Science Reviews* (1998).

[44] Szebehely, V. *Theory of orbits, the restricted three body problem*. Academic Press, 1967.

[45] Tiwari P.M., J. S., and un Nabi, M. Rigid spacecraft attitude tracking using finite time sliding mode control. *Third International Conference on Advances in Control and Optimization of Dynamical Systems* (2014), 263–270.

[46] W., O. K. International Sun-Earth Explorer: A Three-Spacecraft Program. *Science 198*, 4313 (1977), 131–138.

[47] Whittaker, E. T. *Treatise on the Analytical Dynamics of Particles and Rigid Bodies*. Cambridge University Press, 1961.

[48] Xiong, J.; Zhou, Z. Y. X. W. X. F. Y. L. Y. A colloid micro-thruster system. *Microelectronic Engineering 61* (2002), 1031–1037.

[49] You, Z. Micropropulsion - Space Microsystems and Micro/nano Satellites. *Micro and Nano Technologies* (2018), 295–339.

[50] Zazzera Franco B., Topputo F., M. M. Assessment of Mission Design Including Utilization of Libration Points and Weak Stability Boundaries. *Dipeartimento di Ingegneria Aerospaziale, Politecnico di Milano*.